

博 士 論 文

**Research on clinical gait analysis based on
predictive assessment for the exoskeleton
rehabilitation robot**

2022 年 5 月

王 躍 飛

Abstract

Patients with lower limb dyskinesia due to stroke have the potential to remodel their motor nervous system. Gait deviations require data obtained from clinical gait analysis to assess the gait characteristics of the patient. Patients suffering from lower limb dyskinesia, especially in early stages of rehabilitation, have weak residual muscle strength in the affected limb and require passive training by the lower limb rehabilitation robot. Anatomy indicates that the biceps femoris short head muscle has a strong influence on knee motion at the swing phase of walking. The knee locomotion in gait cycle is actuated by the biarticular hamstrings (HAMS), gastrocnemius (GAS) and biceps femoris short head (BFSH). We sought to explore how it affects the gait cycle in the optimization framework. However, the training trajectory of conventional rehabilitation robots performing passive training usually follows gait planning based on general human gait data, which cannot simultaneously ensure both effective rehabilitation of affected limbs with varying severity pathological gait and comfort of the wearer within a safe motion trajectory.

In this thesis, we propose a clinical gait analysis framework based on predictive simulation assessment in the lower limb exoskeleton rehabilitation (LLER) robot, including a predictive assessment module and an LLER robot controller module. The framework is mainly used for passive training in the early stage of rehabilitation and active training in the middle and late stages of rehabilitation. The predictive assessment module aims to reproduce the pathological gait and the gait parameters of the model are obtained through simulation. The desired parameters are selected as input expected values for the LLER robot to achieve a customized rehabilitation strategy. In predictive assessment module, to elucidate the effects of weakness and contracture, we systematically introduced isolated defects into the knee musculoskeletal model and generated walking simulations to predict the gait adaptation due to these defects. We applied mild, moderate and severe muscle weakness or contracture to the BFSH, trained the model to walk at a self-selected speed, and investigated the relationship between them. The findings indicated that severe muscle contracture leads to severe knee flexion; severe muscle weakness induces a significant posterior tilt of the upper trunk, which hinders walking speed. Then, we attempt to establish modification rules for the knee locomotor model by modifying the model's muscle parameters to reproduce the gait characteristics of the affected limb. The effects of HAMS, GAS and BFSH on knee joint in gait cycle are investigated using predicted forward dynamics. The results showed that with more severe contracture, the non-swinging phase presented more severe knee hyperflexion and stronger knee torque, and the sensitivity for change is ranked by GAS>BFSH>HAMS. In swing phase, HAMS and GAS contractures aggravate the knee angle, whereas contractures of BFSH have a weak effect on knee angle. Mild HAMS muscle weakness accelerated walking speed, while moderate and severe HAMS muscle weakness hindered walking speed instead. BFSH muscle weakness is more sensitive to knee joint torque.

In the early stages of rehabilitation training, the predicted simulation results are adjusted by the physiotherapist and used as the expected value for trajectory tracking. To achieve fast trajectory tracking and improve the anti-disturbance capability for LLER robot, a PD controller with gravity compensation and a robust controller are developed. In the mid to late stages of rehabilitation, activation of affected muscle groups tends to gradually restore the relationship with

the central nervous system (CNS). Therefore, we developed a multimodal integrated human intention recognition modual based on motor imagery (MI). It consists of an MI-based EEG intent signal acquisition framework and an EMG-based locomotion command correction framework. The EMG-corrected EEG commands start the LLER robot to perform one complete gait cycle. This active training aims to rebuild the patient's motor nervous system and achieve complete rehabilitation.

Finally, a variable parameter impedance controller for the LLER robot is developed. We apply the knee joint angle and torque parameters optimized by predictive forward dynamics simulation as the expected values for the robot to achieve customized tuning of the motion trajectory for the exoskeleton rehabilitation robot and meet the different rehabilitation stages.

Acknowledgments

I would like to express sincere appreciation to my advisor, Professor Liu Zhen. I would like to thank him for his invaluable support and continuous guidance. This thesis would never be done without his guidance, advice and encouragement. I was very fortunate to be his student. Liu encouraged me to set the highest standards and have ambitious goals in my research, and he enabled me to achieve my goals. His insights gave me lots of inspiration for my project. In addition to the study, Liu also gave me a lot of help in daily life.

I thank professors of review committee for serving on my thesis committee and offering me their helpful suggestions and comments on how to improve my thesis, which guided and challenged my thinking, substantially improving this work.

I would particularly like to acknowledge my colleagues, Prof. Zhiqiang Feng, Dr. Li Ying, and Dr. Jiaqin Zhong for their wonderful collaboration and patient support. I would also like to acknowledge Dr. Meihua Zheng of Nagasaki University of Applied Science for her selfless help in my study and life in Japan.

Last but not least, I shall express, from the bottom of my heart, my deepest gratitude, appreciation, and thanks to my parents. Thanks for their belief in me all the time, for their understanding and encouragement from far away. Without their boundless love and encouragement, I would never have come to this point in my career. I would also like to thank Chuhao Zhang. With his help, I was able to successfully complete Chapter 4. I'm very grateful to Dr. Lei Shi, with his help, I successfully completed the experiments of EMG. Also, his experience in researching medical rehabilitation equipment has benefited me a lot. I am very grateful to the students in the research lab for their help in my research and daily life.

Finally, I would also like to express my gratitude to those people and institutions for providing support during writing the thesis, such as Inner Mongolia University of Science and Technology provided the EEG experimental equipment and place.

In addition, this work was supported in part by 2021 Guangxi University's Young and Middle-aged Teachers' Basic Research Ability Improvement Project (Grant No.2021KY0442), Guangxi Ship Digital Design and Advanced Manufacturing Engineering Technology Research Center of Beibu Gulf University.

Contents

Abstract	i
Acknowledgments.....	iii
Contents.....	iv
List of Figures	vii
List of Tables.....	xi
List of Acronyms/Abbreviations.....	xii
Chapter 1. Introduction	- 1 -
1.1 Background	- 1 -
1.2 Current status of research and challenges for clinical gait analysis.....	- 4 -
1.2.1. Application of multichannel SEMG in clinical gait analysis	- 4 -
1.2.2. Application of EEG sensors in clinical gait analysis.....	- 8 -
1.2.3. Challenges.....	- 11 -
1.3 Lower limb exoskeleton rehabilitation robots: state-of-the-art.....	- 11 -
1.3.1 Lower limb exoskeleton rehabilitation robot	- 11 -
1.3.2 Challenges	- 14 -
1.4 Research program of the thesis	- 15 -
1.5 Organization of the thesis	- 17 -
Chapter 2. Overall Framework.....	- 18 -
2.1 The overall framework of the system	- 18 -
2.1.1 Predictive Assessment Module	- 18 -
2.1.2 LLER Robot Controller	- 19 -
2.2 Framework functionality and preliminary considerations.....	- 20 -
2.2.1 Framework functionality.....	- 20 -
2.2.2 Intended use of the framework	- 22 -
2.3 Impedance control system for LLER robot	- 23 -
2.4 Conclusion.....	- 24 -
Chapter 3. Predictive Assessment in Passive Training for Rehabilitation	- 25 -
3.1 Predictive Dynamics	- 25 -
3.1.1 Methods.....	- 26 -
3.1.2 Simulation and optimization module.....	- 27 -

3.1.3 Musculoskeletal model	- 28 -
3.1.4 Gait controller	- 32 -
3.1.5. Generation of gait simulations.....	- 35 -
3.2 Experiment design.....	- 35 -
3.2.1 Pathological knee gait caused by BFSH muscle contracture or muscle weakness	- 36 -
3.2.2 The effects of muscle group synergy in gait cycle related to knee joint motion -	36 -
3.3 Validation	- 36 -
3.3.1 Validating the model's gait over a range of speeds	- 36 -
3.3.2 Walking with BFSH contracture or weakness in the swing phase	- 37 -
3.3.3 Validation for knee joint in gait cycle with muscle contracture or weakness-	38
-	-
3.4 Experimental validation of muscle activation	- 40 -
3.5 Discussion	- 42 -
3.6 Conclusion.....	- 44 -
Chapter 4. Motion Intent Detection Module Based on Multimodal Integration	- 45 -
4.1 Overview of detection architecture.....	- 45 -
4.2 Application advantages and characteristics of EEG sensors	- 47 -
4.3 Signal extraction and processing	- 49 -
4.3.1 EEG signal detection and data processing.....	- 49 -
4.3.2 EMG signal detection and data processing.....	- 51 -
4.4 Experiment and validation	- 52 -
4.4.1 Experimental design.....	- 52 -
4.4.2 Experimental conclusions	- 54 -
4.5 Conclusion.....	- 55 -
Chapter 5. LLER Robot Modeling and Controller Design.....	- 56 -
5.1 Control strategies for gait rehabilitation	- 56 -
5.2 Mathematical Model Formulation of LLER Kinematic Analysis	- 56 -
5.3 Reference trajectory acquisition based on predictive assessment	- 59 -
5.4 Controller for trajectory tracking model of LLER robot.....	- 62 -
5.4.1 Development of PD controller for hip-knee robot	- 62 -
5.4.2 Development of Robust Adaptive PD Controller for LLER Robot	- 65 -

5.5 Variable parameter impedance controller with gravity compensation	- 69 -
5.5.1 Variable parameter impedance controller for LLER robotics	- 70 -
5.5.2 Simulation of LLER robot knee joint tracking with impedance controller based on variable parameters.....	- 72 -
5.5.3 Development of impedance tuning approach based on a novel PSO algorithm - 75 -	
5.6 Conclusion.....	- 76 -
Chapter 6. Conclusions	- 78 -
6.1 Contributions.....	- 78 -
6.2 Future work and prospect.....	- 79 -
Appendix	- 81 -
A: Predictive assessment of the high-level control state of the simulation.....	- 81 -
B: Measurements for predictive assessment simulation.....	- 82 -
C: Initial Covariance Matrix Adaptation Evolutionary Strategy (CMA-ES) standard deviation for each free parameter.	- 83 -
References	- 84 -

List of Figures

Figure 1.1 Schematic view of SEMG application within a gait analysis laboratory.	- 5 -
Figure 1.2 Wireless SEMG acquisition and analysis system: FREEDOM SEMG System.....	- 6 -
Figure 1.3 Schematic diagram of SEMG system in clinical gait detection analysis.	- 7 -
Figure 1.4 Application of pressure sensors in gait analysis. The red area indicates high pressure, blue area indicates low pressure.	- 8 -
Figure 1.5 Architecture for clinical gait analysis based on BCIs.	- 10 -
Figure 1.6 EEG Electrode Montage Corresponding to the International 10-20 System.....	- 10 -
Figure 1.7 Three types of lower limb exoskeleton rehabilitation robots. (A) Upright rehabilitation robot [19], (B) The LLR-II Rehabilitation [62], and (C) Planar parallel lower limb rehabilitation robot [63].....	- 13 -
Figure 1.8 Comparison of predictive forward dynamic simulation and LLER robot.	- 17 -
Figure 2.1 Architectural of the rehabilitation framework based on predictive assessment.	- 20 -
Figure 2.2 Flow chart of LLER robot framework based on predictive forward simulation.	- 22 -
Figure 3.1 Predictive forward module for dynamic optimization. Relationship between gait controller, musculoskeletal model, measurement feedback, and forward simulation. We implement the musculoskeletal model in OpenSim3.3 and use SCONE for the forward prediction simulation.	- 27 -
Figure 3.2 The planar musculoskeletal model of gait.	- 28 -
Figure 3.3 The architecture of the adopted Hill-type muscle-tendon actuator model. PE is the passive elastic element, CE is the muscle contractile element, and SE is the serial-elastic element that represents the tendon. FT is the complete musculotendinous actuator. LMT , LM , are the complete length of the model unit and muscle length.	- 29 -
Figure 3.4 Muscle force-length, $fLLM$, and force-velocity, $fvLM$, curve used in model.....	- 30 -
Figure 3.5 The gait controller combines state machines and low-level control laws to determine the excitation, using the right leg as an example.	- 32 -
Figure 3.6 Effects of muscle physiology on activation illustrated by GAS activation and normalized fiber length in gait cycle.	- 34 -
Figure 3.7 Activation dynamics of the BFSH model in healthy gait cycle transforms the neural excitation (u) into the muscle activation (a).	- 34 -
Figure 3.8 Flowchart illustrating the forward dynamics component in OpenSim and SCONE.	- 35 -
Figure 3.9 Validating the model's gait over a range of speeds. Three prescribed speeds 0.6 m/s (red), 1 m/s (blue) and 1.4 m/s (green), and a self-selected speed (black) were analyzed. Joint	

angles for the hip (A), knee (B), and ankle (C) were plotted. Positive joint angles indicate flexion. Simulated kinematics and kinetics are compared with the experimental data (gray area) collected by Schwartz et al [101]. - 37 -

Figure 3.10 Predictive forward simulation of gait with BFSH contracture or weakness. Comparisons of knee angles in one gait cycle between the normal gait and three degrees of mild, moderate and severe of BFSH muscle contracture (A); Comparisons of knee angles with weakness (B); Comparisons of knee load with contracture (C); Comparisons of knee load with weakness (D). Joint load (BW), normalized by weight, denoted as $load = joint\ force / (model\ mass * g)$.- 38 -

Figure 3.11 Validation for knee joint in gait cycle with muscle contracture. Knee kinematics and kinetics with normal (red), mild (blue), moderate (green) and severe (purple) contractures in HAMS, GAS and BFSH, respectively, are compared with the experimental data (gray area) collected by Schwartz et al [101]. The gait for knee angles (left column) and knee moments (right column) are plotted with different severities of muscle contractures. - 39 -

Figure 3.12 Validation for knee joint in gait cycle with muscle weakness. Knee kinematics and kinetics with normal (red), mild (blue), moderate (green) and severe (purple) weakness in HAMS, GAS and BFSH, respectively, are compared with the experimental data (gray area) collected by Schwartz et al [101]. The gait for knee angles (left side) and knee moments (right side) are plotted with different severities muscle weakness..... - 40 -

Figure 3.13 Experimental validation scheme for BFSH excitation-activation. (A) EMG sensor and its placement. (B) Predictive simulation module for excitation and activation, and normalized EMG acquisition data were averaged from the group with the highest repeatability. (C) EMG data acquisition at BFSH in continuous gait cycles. Muscle activation was recorded starting from >170, and thresholds at signal intervals of -512 to 512 were considered as muscle activation until sustained inactivation..... - 41 -

Figure 3.14 Muscle activation in normal gait at self-selected speed. - 42 -

Figure 4. 1 Schematic representation of the motion intent detection system with multi-modal.- 46 -

Figure 4. 2 HMI actions of the assisted LLER robot and their transformation. - 47 -

Figure 4. 3 EEG acquisition equipment and experimental environment. (A) is the subject wearing EEG to do squat-up movement, (B) is the 13-channel electrode distribution for the international 10-20 system, and (C) is the EEG host..... - 50 -

Figure 4. 4 Flowchart of the preprocessing and decoding algorithm. - 51 -

Figure 4. 5 Activation of BFSH in the right leg during rise-squat movement measured with EMG. (A) EMG in the first cycle, (B) EMG acquisition devices and measurement locations, and (C) EMG in the first two consecutive cycles..... - 52 -

Figure 4. 6 Channel spectra and maps. - 53 -

Figure 4. 7 13-channel EEG acquisition of time-domain data for squat-rise movements..... - 54 -

Figure 5.1 Two link model for dynamic analysis of lower limb exoskeleton robot. It includes link lengths (l_1, l_2), center of gravity for link lengths (lc_1, lc_2), the approximate mass of the lower limbs (m_1, m_2), the angles between the rotational point (q_1, q_2), counterclockwise negative. - 57 -

Figure 5.2 Gait fitness of predicted forward dynamics. - 60 -

Figure 5.3 Knee changes in a gait cycle. - 61 -

Figure 5.4 Predicted value of right knee joint angle in 0-10 seconds. - 62 -

Figure 5.5 Block diagram of the PD controller for the hip-knee LLER robot..... - 63 -

Figure 5.6 Angle tracking of the hip and knee for the robot in normal simulated gait cycle. (A) is the trajectory tracking of the LLER robot hip joint. (B) is the trajectory tracking error of the LLER robot hip joint. (C) is the trajectory tracking of the LLER robot knee joint. (D) is the trajectory tracking error of the LLER robot knee joint. - 64 -

Figure 5.7 Torque generated by LLER robot's hip and knee in normal simulated gait cycle. (A) is the torque generated by the robot's hip. (B) is the torque generated by the robot's knee. - 65 -

Figure 5.8 Block diagram of the robust adaptive PD controller for the hip-knee LLER robot. . - 68 -

Figure 5.9 Simulation results of the robust adaptive PD controller for the LLER robot. (A) and (B) show the angle trajectory tracking of the hip and knee, respectively. (C) and (D) presents the angle tracking errors of the hip and knee, respectively. (E) and (F) are the angle velocity tracking of ankle and knee, respectively. (G) and (H) show the angle velocity tracking errors of hip and knee, respectively..... - 69 -

Figure 5.10 Schematics illustrating of ideal impedance control system for LLER robot. The input to the control system is the predicted joint angles and joint loads after the optimization [138]. In the exoskeleton robot model, we assume that the simulation parameters for the robot are Table 5.1. - 71 -

Figure 5.11 Architectural framework of variable impedance PD controller based on predictive assessment. The inputs to the control system are optimized predicted joint angles and joint loads with offset values set by the physiotherapist [138]. In the exoskeleton robot model, we assume that the masses, lengths and momentum of Inertia for shank and thigh are $8kg$, $0.5m$ and $0.4kgm^2$, respectively..... - 72 -

Figure 5.12 Knee joint angle trajectory and load tracking. The left and right columns are robot tracking for the forward predictive assessment of BFSH contracture severity and muscle weakness severity, respectively. The top row presents the robot knee trajectory tracking and the bottom row presents the robot knee load tracking. - 73 -

Figure 5.13 Knee joint angle trajectory tracking and torque tracking. The parameters obtained from the uninjured walking simulation (gray area) are compared to the angular tracking (top) and moment tracking (bottom) of the robot knee joint with three different impedance parameters, Damping Bd (Ns/m) and Stiffness Kd (N/m). - 74 -

Figure 5.14 Flowchart for the hybrid controller based on PSO algorithm..... - 76 -

Figure 0.1 High-level control states for each leg [145]. (A) denotes the signed horizontal distance (d) between the center of gravity and the ankle of the model. (B) denotes the stance and swing phases triggered by the ground reaction force ($FGRF$). (C) is the state transition for high-level control of each leg. $F(\text{stance load threshold})$, $F(\text{swing load threshold})$, $d(\text{landing threshold})$ and $d(\text{late stance threshold})$ are the threshold parameters, respectively. Corresponds to the 4 range thresholds and load thresholds mentioned in section 3.1..... - 81 -

List of Tables

Table 1.1 Related work on rehabilitation robots.....	- 2 -
Table 1.2 Part of the EEG acquisition equipment parameters.....	- 11 -
Table 1.3 Design of some Institute exoskeleton robots.....	- 12 -
Table 3.1 Slow-twitch ratio of various muscles in the Hill-type activation model.....	- 31 -
Table 3.2 Muscle parameters for the unimpaired musculoskeletal model.	- 31 -
Table 3.3 The impact of contracture or weakness of muscle groups on knee joint in gait cycle.-	43
-	
Table 4.1 EEG frequency classification.....	- 49 -
Table 4.2 Action trigger time of the object in the experiment.....	- 53 -
Table 4.3 Waveform amplitude at each trigger moment during EEG measurement.....	- 55 -
Table 5.1 Parameters for simulation.	- 59 -
Table 5.2 Parameter CMA optimizer.	- 60 -
Table 5.3 The lower limb of the exoskeleton's DOF design.	- 61 -
Table 5.4 Parameters for simulation.	- 62 -
Table 0. 1 Con-Sev optimized gait conversion parameters	- 82 -
Table 0. 2 Initial CMA-ES standard deviation for each free parameter.....	- 83 -

List of Acronyms/Abbreviations

MTU: Musculotendon Units	COP: Center of Pressure
HES: Human Exoskeleton System	CMRR: Common mode rejection ratio
ODE: Ordinary Differential Equations	MRCP: Movemnt-Related Cortical Potential
ZMP: Zero Moment Point	ERS: Event-Related Synchronization
SSMVEP: Steady-State Motion Visual Evoked Potential	ERD: Event-Related Desynchronization
LLER: Lower Limb Exoskeleton Rehabilitation	WPAL: Wearable Power-Assist Locomotor
DOF: Degree of Freedom	CMRR: Common Mode Rejection Ratio
PID: Proportional Integral Differential	CMA-ES: Covariance Matrix Adaptation Evolutionary Strategy
BCI: Brain Computer Interface	SCONE: Simulation and CONTROL Environment
EMG: Electromyographic	CNS: Central Nervous System
SEMG: Surface electromyographic	ES: Early Stance
EEG: Electroencephalographic	MS: Mild Stance
VGRF: Vertical Ground Reaction Force	PS: Pre-Swing
IMU: Inertial Measurement Unit	S: Swing
CPM: Continuous Passive Motion	LP: Landing Preparation
GMAX: Gluteus Maximus	ICA: Independent Component Analysis
HAMS: Hamstrings	ERP: Event-related Potentials
ILPSO: Iliopsoas	MI: Motor Imagine
RF: Rectus Femoris	PSO: Particle Swarm Optimization
VAS: Vastus	HMI: Human Machine Interface
BFSH: Biceps Femoris Short Head	AAN: Assist As Needed
GAS: Gastrocnemius	PD: Proportional Differential
SOL: Soleus	ITAE: Integrated Time and Absolute Error
TA: Tibialis Anterior	

Chapter 1. Introduction

In this chapter, we will present the study background, the current status of the study, and the purpose of the thesis. This chapter will give us a preliminary understanding of the research content and organization of the thesis.

1.1 Background

The aging population is a global issue, and physical deterioration and frailty in elderly people have become a socio-economic problem in many countries. A survey from the United Nations reveals that people older than 60 years represented 11.5% of the global population in 2012, and this percentage will be nearly doubled by 2050 [1]. Human knee joints play a crucial role in performing daily life activities, such as standing and walking. Each year 250 new lower spinal cord lesions occur in the Netherlands, resulting in paraplegia. These patients are paralyzed from the pelvis to the feet and lose, among other things, the ability to stand and walk [2]. Losing these abilities can have great consequences on the patient's mental state. Patients with neurological disorders caused by disease or injury, such as stroke and spinal cord injury, commonly present with muscle weakness or contractures which lead to lower Limb dyskinesia [3]. Pathological gait with irregular muscle groups directly causes insufficient force or torque in the lower limb joints [4]. Janet Taylor and Dario Farina [5] found that due to muscle-related changes, a slower preferred walking speed emerged in elderly people as they improved their walking ability. Common gait deviations in cerebral palsy can be divided into gait patterns of spastic hemiplegia (drop foot, horseshoe in different knee positions) and spastic diplegia (true horseshoe, jumping, pronounced horseshoe and squatting) [6]. T Mark Campbell and Guy Trudel [7] investigated the associations between knee flexion contracture with the range of extension, function, pain, and stiffness of the contralateral knee. G.E. Rose et al. [8] found no significant relationship between time and body mass index for worsening knee flexion range, knee flexion in intermediate stance, peak knee extension in stance and hamstring length, and improvement in mean and maximum hip rotation in children with bilateral cerebral palsy and no history of orthopedic surgery in their gait analysis. However, there are many patients worldwide with knee impairments such as muscle weakness, pain, paralysis, and gait disorders, which can be caused by a stroke, spinal cord injury, post-polio, injury, osteoarthritis, and other diseases [9][10]. At present, with a rapidly aging population and the increase of physical movement disorders patients caused by various diseases, rehabilitation robot technology has become a new research field that combines medicine and engineering [11]. The study of movement draws from and contributes to diverse fields, including biology, neuroscience, mechanics, and robotics [12].

Traditional rehabilitation is not only physically exhausting for the therapist, but 44% of the patients who are rehabilitated by physiotherapy will have future problems [13]. Paralyzed patients with movement disorders require extensive rehabilitation programs to restore ambulatory function. Traditional manual therapy methods are labor-intensive and have limited therapeutic effects, thus promoting the development of robot-assisted rehabilitation therapy [14][15]. By using robotic-assisted rehabilitation devices, it is possible to reduce the intensive work as well as facilitate the customization of rehabilitation based on the diagnosis of the data obtained [16]. There are several

methods to determine the appropriate trajectory for the movement of the rehabilitation robot (see Table 1.1). We note, a prerecorded trajectory obtained by gait analysis, a prerecorded trajectory during therapist assistance which requires data use, and modeling the trajectory based on normative movements which can be based on kinematics and/or dynamics constraints during the path motion in terms of fitting more realistic motion [17].

Table 1.1 Related work on rehabilitation robots.

Study and Brand	Fusion Method	Fusion Input	Fusion Output	Training mode	Test
Yu GJ et al. [18], /	Butter-worth filter	MI	The speed of gait training	Active training	Prompt signal-performance MI-robot moved
Milia P et al. [19], Ekso	Adjust motor power according to residual muscle force	Buttons on the crutches	Joint position and angle	Passive training, active powered	FirstStep-ActiveStep-ProStep
Nitschke, J et al. [20], HAL	Calculating stride length and muscle strength	Myoelectric potentials	Joint angle and torque	Active training, Passive training	Using woodway on the treadmill or therapy with the HAL on a rollator
Jung, C et al. [21], COWALK	3D motion capture data acquired from normal gait, PD feedback control commands joint movement	Joint trajectory as a reference input	Joint movement	Passive training	Free Walking-Actuated Legs and Actuated Pelvis- Actuated Legs and Locked Pelvis
Lim, D et al. [22], HEXAR	Control Law with Human-Robot Interaction Force	Insole sensor	Joint angle, Joint movement	Hip: Passive/Active; Knee: Active, Ankle- quasi - Passive	EMG measures muscle activity- Insole sensor measures the vGRF
Tannous, H et al. [23], /	Real-time quaternion-based fusion scheme, based on the extended Kalman filter	One Kinect visual sensor and two Shimmer IMU sensors	Joint angle	Active training	Motion capture-Signal processing-Joint motion estimation-Robotics
Song, B et al. [24], /	Real-time motion profiles based on a weighted fuzzy logic algorithm	Four fuzzy inputs were produced through the hip joint angles;	The motion profiles during the defuzzification	Passive training	Angle/pressure sensor acquisition-Fuzzy algorithm analysis-Motion profile-Robot
Wang, X et al. [25], /	Continuous nonlinear ordinary differential equations (ODE), the zero-moment-point (ZMP) theory and three splines in interpolation method, PID controller,	Gait model and sensor acquisition signals	Ten DOFs	Passive training	Gait Modeling; Sensor: zero-moment-point (ZMP) +PID control-robot
Li, L et al. [26], LLRTS	EEG-driven Lower Limb Rehabilitation Training System; Steady-State Motion Visual Evoked Potential (SSMVEP) BC I system	Visual stimulation	Joint angle	Active training, Passive training	Acquisition and processing of EEG-Stimulation paradigm-Stroke patient- robot

For rehabilitation purposes, it is desirable to have the trajectories planning similar to the trajectories of a normal human lower limb movement, to ensure the comfortable and correct movements as practiced during activities of daily life. Indeed, motion therapy can be carried out in different modes including passive, active, active-resistive, active-assistive, and bilateral exercises, which differ depending on the degree of patient involvement [27]. Selecting the proper mode strategy requires an appropriate rehabilitation robot choice, with concerned patients. It enables the robot to perform cyclic motion, which is an essential requirement for repetitive operations. Moreover, this approach requires little computational time, making it particularly favorable for the real-time control of a redundant robot. On the other hand, state-of-the-art bipedal locomotion control methods directly output joint torques, which ignore constraints and energetic costs imposed by muscle anatomy and physiology. Consequently, to accomplish a motion task, controllers often employ torque patterns that are inefficient or even impossible for humans. These biologically implausible torque patterns diminish the naturalness of the resulting gaits [28]. Therefore, devices that can help individuals with knee dysfunctions to regain the ability to walk with a natural gait are desirable, and they are designed to improve the physical and mental health of these patients. To obtain the reference trajectory, Bin Chen et al. [29] applied a motion capture system to acquire the 3D kinematic data from the lower body for normal walking of healthy people. Moreover, the joint angles at special timing were derived from the human exoskeleton system (HES) leg geometry constraints. They also modified the designed reference trajectories, such as gait period and amplitude, for different wearers according to their physical characteristics. However, it is a challenge to determine these characteristics, not to mention determining the gait reference trajectory for patients with pathological gait. It was found that inertial or optical motion capture sensors lack accuracy when estimating joint angles during motion capture, which could lead to incorrect data interpretation. Therefore, Halim Tannous et al. [23] proposed fusion between inertial and visual motion capture sensors to improve the estimation accuracy of joint angles. In another study, Yi Zheng et al. used a human motion capture system: four high-speed cameras, a testbed, and a computer system to study the stability of the exoskeleton robot's climbing posture using an effective data acquisition area in the view of two high-speed cameras[30].

Patients with lower limb movement disorders, especially in the early stages of rehabilitation, have weak residual muscle strength in the affected limb and require passive training of the affected limb by a lower Limb rehabilitation robot [31][32][33]. In the continuous passive motion (CPM) stage [34], the rehabilitation robot mainly drives the affected limb to perform rehabilitation training according to the preset gait trajectory. However, the motion trajectory of conventional rehabilitation robots performing passive training follows a gait plan established based on normal human gait data [16]. This singularity in the motion trajectory of the rehabilitation robot during the passive training stage may not simultaneously ensure both effective rehabilitation and safe motion trajectories for different levels of pathological gait, and may cause patient discomfort during this rehabilitation training. Inverse kinematic simulations have been successfully applied to estimate human motions which are not directly observable, such as muscle forces or joint moments [35]. Although these inverse simulations provide useful insights into human motion, they rely on existing data and cannot predict new behavior [12]. Moreover, motion capture requires expensive hardware equipment, which makes it difficult to apply to the rehabilitation treatment

stage.

BFSH weakness and contracture, usually occur in conditions such as cerebral palsy, stroke and secondary dysfunction after knee osteoarthritis surgery. Although these deficits are the pathologies that lead to the observed knee flexion contractures, this phenomenon is usually accompanied by neurological deficits and biomechanical factors, making it difficult to confirm the correspondence. Carmichael F. Ong et al. [3] applied the predictive dynamics simulation method to investigate how SOL and GAS muscles affect the plantar flexor of the ankle joint and generalized the relationship between them. Kirsten Veerkamp et al. [36] evaluated how gastrocnemius hyperreflexia affects gait kinematics by using predictive simulations. The isometric length and force of the muscles and tendons have a large effect on the movement of the knee joint [7]. Knee flexion contracture and semi membrane tendon and biceps femoris tendon affect each other [37]. Anatomy indicates that the BFSH muscle group has a strong influence on knee joint motion during the swing phase of walking [38][39].

The bipartite HAMS and the unipartite GAS and BFSH muscle groups play the most significant role in knee motion during the walking gait cycle [3][40][41]. Weakness and contractures of these muscle groups usually occur in conditions such as cerebral palsy, stroke and secondary dysfunction after knee osteoarthritis surgery [42][43][44]. Carmichael F. Ong et al. [3] applied the predictive dynamics simulation method to investigate how SOL and GAS muscles affect the plantar flexor of the ankle joint and generalized the relationship between them. Kirsten Veerkamp et al. [36] evaluated how gastrocnemius hyperreflexia affects gait kinematics by using predictive simulations.

1.2 Current status of research and challenges for clinical gait analysis

Research [45] has found gait analysis to be more accurate than visual gait assessment. Some research laboratories have provided evidence that gait analysis can change treatment decisions. Tishya A. L. Wren et al. [46] have found that gait analysis not only changes treatment decisions when inconsistent with the original treatment plan but also reinforces treatment decisions when consistent with the original plan. Cheng-Tang Pan and Yow-Ling Shiue [47] developed a multi-loop modulation method on the servo drives for lower limb rehabilitation exoskeleton, the predefined joint trajectories were derived from clinical gait analysis or recorded by healthy individuals, which is the desired trajectory of a robotic exoskeleton.

1.2.1. Application of multichannel SEMG in clinical gait analysis

EMG sensors are devices that direct, amplify, record and display bioelectrical signals generated by the neuromuscular system as it completes its activity, and are used to reflect physiological information about muscles in real time. It is a meaningful assessment tool for locomotion function diagnosis and a better biofeedback therapy technique.

Application of surface electromyography (SEMG) to the clinical evaluation of neuromuscular disorders can provide relevant “diagnostic” contributions in terms of nosological classification, localization of focal impairments, detection of pathophysiological mechanisms, and functional assessment.

The present review article elaborates on: (I) the technical aspects of the myoelectric signals acquisition within a protocol of clinical gait analysis (multichannel recording, surface vs. deep

probes, electrode placing, encumbrance effects) (II) Sequence of procedures for subsequent data processing (filtering, averaging, normalization, reproducibility control) and (III) a set of feasible strategies for the final extraction of clinically useful information. The application of SEMG for functional diagnosis is achieved through the kinematic and kinetic analysis of factors such as changes in passive muscle-tendon properties (peripheral non-neural components), paralysis, spasticity and selective loss of motor output of functionally antagonistic muscles by non-invasive assessment of relevant pathophysiological mechanisms impeding gait function [48]. The basic instrumentation is represented (see Fig.1.1): TV-based motion analyzer for retro-reflective markers detection, dynamometric force platform for ground reaction measurement, the portable device and the fixed unit of a radio-telemetric EMG system. The bipolar electrodes and their pre-amplification case are depicted in the lower inset.

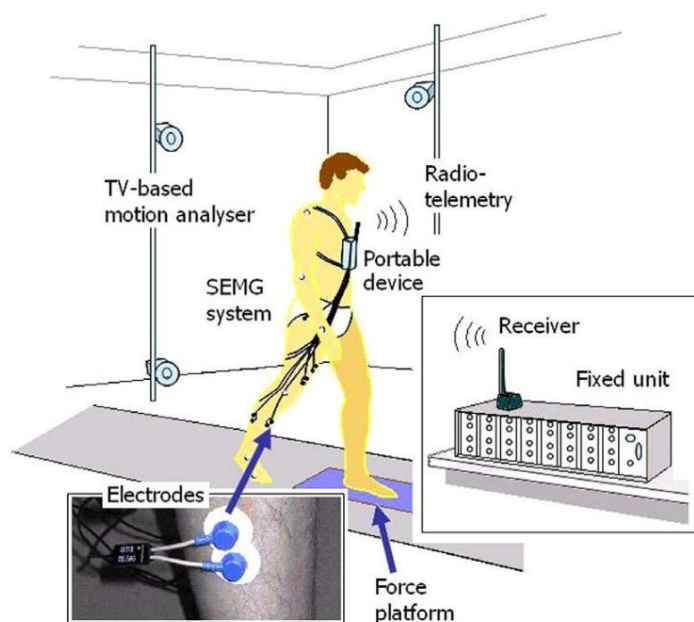


Figure 1.1 Schematic view of SEMG application within a gait analysis laboratory.

In clinical gait analysis, SEMGs are collected simultaneously with kinematic and kinetic descriptors of locomotor movements. These signals can be obtained by microswitches fixed on the foot plant, multi-sensor foot insole, ground reaction platforms, electrogoniometers and/or video-analysis systems. Adoption of such a “comprehensive” approach might produce side effects in terms of slowing preparation time, possible appearance of fatigue phenomena in patients, and potential prejudice in their ability to perform natural locomotor actions, with consequent limitation of representativity of data collected. In fact, a crucial requirement for an EMG system to be applied in gait analysis is a minimum encumbrance, which can be achieved by adopting small pre-amplifiers integrated into the electrodes, light flexible wires and relatively low-weight portable devices communicating to a fixed receiver unit by radiotelemetry (see Fig. 1.1).

In a study performed by Winchester et al. [49] no-significant differences between surface, wire and no-electrode walking conditions were detected in normal adults as far as stride dimensions were considered. Quite noticeable in this respect is the recent implementation of separate radio-transmitting devices for each channel, which includes a couple of sensors, pre-

amplifiers and radio-transmitter in a single self-powered case (see Fig. 1.2). One of the great advantages of the FREEDOM SEMG sensor is that the sensor module can be fixed in the muscle area to be measured as needed. The measurement signal channel is transmitted by the host computer via a wireless network, allowing the subject to make larger movements. Mainly used for muscle contraction pattern assessment, muscle fatigue assessment, athlete data interpretation and training recommendations.

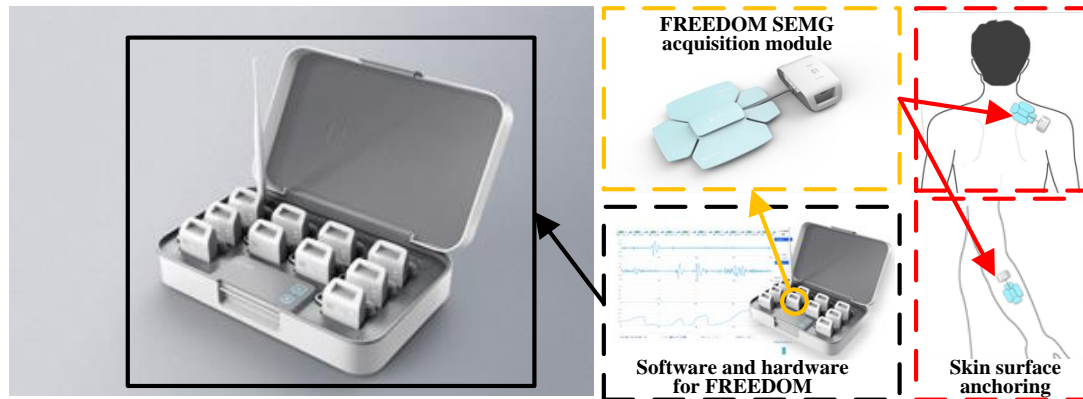


Figure 1.2 Wireless SEMG acquisition and analysis system: FREEDOM SEMG System.

The current wireless surface EMG signal acquisition system used for gait analysis has the following features.

- Wireless transmission with real-time feedback. Synchronized display. Ultra-low power consumption: can work continuously for 10 hours and standby time >10 days. Skin fixation is strong and stable, with no displacement for strenuous movements, and high-fidelity restoration of biological signals. There are 10 channels EMG, combined with IMU sensor acquisition at the same time, it can realize multi-dimensional data accurate measurement, in addition to automatic analysis.
- Main applications: movement disorder analysis, assessment of the degree of muscle spasticity, movement pattern analysis, diagnosis and differential diagnosis.
- The sensor system integrates multi-dimensional information IMU sensors (gyroscope and acceleration sensor).
- The system integrates gyroscope (GYR). GYR sensor is a device used to measure the trajectory of the upper and lower limbs of the human body and the three-dimensional angle of the joints, which can collect human motion information in real time.
- Integrated acceleration (ACC) sensor. ACC sensor is used to collect real-time human motion angle information, which can realize simple motion capture function.
- The installation of the sensor is strong and stable: each sensor with auxiliary lamination silicone, the electrode piece is firmly fixed to the skin surface, greatly reducing the influence of motion and noise, ensuring the authenticity of the biological signal.

SEMG sensors evaluate muscle movement mainly by measuring the activation of the muscle surface. The assessment for the degree of muscle contracture includes the following main aspects.

(I) evaluation of muscle contraction and diastolic function, (II) evaluation of neuromuscular motor control function, (III) flexion-relaxation test, (IV) assessment of muscle coordination and (V) testing of muscle endurance level.

Using multi-channel EMG sensors to measure the subject's muscle groups, the motor status of the subject can be assessed synergistically. The movement disorder analysis mainly includes studies on the following areas. (I) research on the coordinated control role of the skeletal muscle system, (II) research on motor control in sports medicine, (III) research on muscle stability and coordination, and (IV) assessment of muscle activation status.

The main aspects for assessment during lower limb rehabilitation are: pre-operative and post-operative assessment; assessment of rehabilitation effects; gait analysis; muscle fatigue analysis. The main operation steps of the SEMG sensor system (see Fig. 1.3) are: firstly, select test items and evaluation indicators, and then configure electrodes according to the posting point scheme. Secondly, guide the testing action and direct the completion of electrical signal acquisition; and thirdly, mark and intercept the acquired EMG data. Finally, customize the analysis/automatic analysis of data and generate data reports. The central motor nervous system consists of the cerebral cortex, spine and muscles. The central motor nerve sends commands in the form of electrical signals that reach the muscle surface and cause the muscle to contract, driving the limb to move. SEMG is fixed to the measured muscle surface and acquires the activation data of the muscle during gait. The pressure sensor on the sole can distinguish the gait posture by judging the change in pressure value (for instance, distinguishing gait transition).

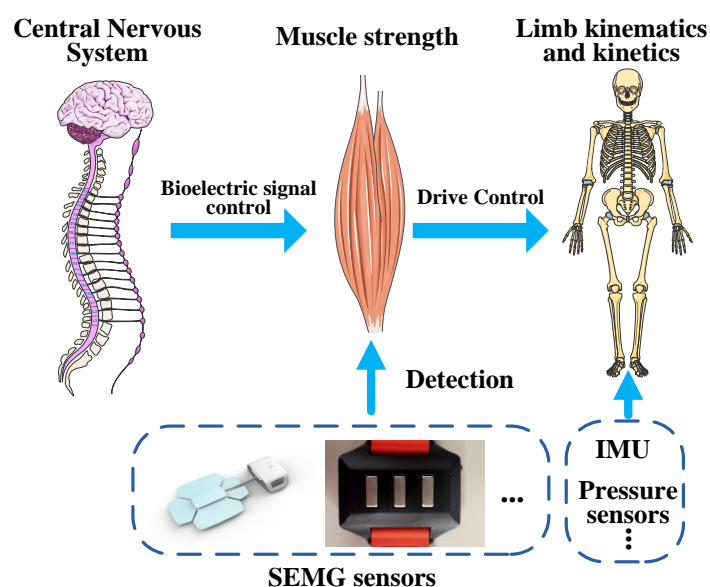


Figure 1.3 Schematic diagram of SEMG system in clinical gait detection analysis.

The FREEDOM is a SEMG sensor system for muscle contraction pattern assessment, incorporating a plantar pressure detection device. The center of pressure (COP) refers to the point of action of the combined plantar pressure, reflecting the overall distribution of plantar pressure. The area of the foot COP curve envelope ellipse (see Fig. 1.4) reflects the stability of the subject directly.

1. Stability can be assessed mentally. The reasons for lack of stability in the vertical stance are both physiological and psychological, namely lack of strength in the core muscles and lack of concentration in the mental state. For the athlete, balance is primarily a reflection of mental status.
2. Left-right balance: Measurement of the elliptical area of the COP envelope on the left and right side alone reflects the balance of both limbs. Promptly communicate with the athlete to adjust the training if it is due to muscle strength differences between the two sides, or to provide prompt treatment if it is due to injury, such as an injury on one side.
3. Eye open/eye closed balance differences: Some athletes have significantly higher balance with eyes closed than with eyes open, presumably due to the exclusion of visual input. In trampoline, balance at the moment of net fall is critical and can be trained in both open/closed eyes to find the optimal balance pattern for the individual.

The right foot of the test subject in Fig. 1.4 had a larger COP envelope area and poorer than normal balance test results, which was strongly related to the poor physical condition of the test subject at that time and should be continuously monitored to avoid movement hazards due to body imbalance.

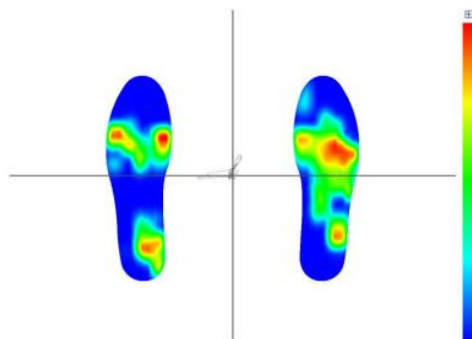


Figure 1.4 Application of pressure sensors in gait analysis. The red area indicates high pressure, blue area indicates low pressure.

1.2.2. Application of EEG sensors in clinical gait analysis

The method based on EEG signal extraction of patient's intention is another approach applied to lower limb rehabilitation training. Current research on this means focuses on the acquisition of EEG signals, extraction of valid information, Brain-Computer Interface (BCI) algorithms and the development of fusion with other sensors.

MI is considered to be the best strategy for natural control of neural prostheses and BCI-based rehabilitation approaches [50]. Ang Kai Keng et al [51], in comparing a combined BMI robotic intervention with a robotic-only intervention, observed that the former required less intensive treatment for the same exercise gain, i.e., 136 and 1040 repetitions of exercise for each modality, respectively. The fact that combining BMI and MI associations may lead to better motor function outcomes is also supported by the EEG study by Pichiorri et al [52]. Muscular control during walking is believed to be simplified by the coactivation of muscles called muscle synergies. Although significant cortico-muscular connectivity during walking has been reported [53], the

level at which the cortical activity is involved in muscle activity (muscle synergy or individual muscle level) remains unclear. Brain decoding techniques, which predict the mental or motor state of a human from recorded brain signals, have received substantial attention for the development of brain-machine interfaces (BMIs) for repairing or assisting deficits in cognitive or sensory motor functions [54]. BCI record, infer and translate different parameters associated with movement from different types of brain signals to provide volitional control to prosthetic limbs, exoskeletons, computers, and even digital avatars. It is a well-known fact that not only the cerebral cortex but also the cerebellum and spinal cord all play a crucial role in ambulatory movements. It is of interest to understand how much information we could extract from the cerebral cortex using non-invasive technology. Previous studies of BCI based on scalp EEG have demonstrated the feasibility of decoding kinematics for lower limb movements during walking. Sho nakagome et al. [55] investigated offline decoding analysis with different models and conditions to assess how they influence the performance and stability of the decoder. In the study of Yokoyama H et al. [56], artifacts in EEG signal were removed using artifact subspace reconstruction (ASR) method. Brain-Computer Interface (BCI) or Brain-Machine Interfaces (BMI) have been more extensively investigated in recent years in the scope of gait rehabilitation due to their great prospect in understanding and analyzing gait-related brain rhythms and Event-Related Potentials (ERPs). As EEG signals can act as a real-time projection of brain's motor activity during gait, EEG-based gait studies hold significant potential in achieving early prediction of future movement plans which researchers can readily utilize for more effective rehabilitation of motor-impaired persons providing them with necessary motor capabilities. In a BCI-based rehabilitation system, the brain waves are extracted, processed, and translated to control an assistive device [57]. For an effective assistive system, it is critical to detect the movement intention as early as possible to provide the system with enough time to adapt to the requirement of the individual [58]. There have been two majorly reported neural features related to movement intention detection. Those are Movement-Related Cortical Potential (MRCP) [59] and Event-Related Synchronization/ Desynchronization (ERS/ ERD) [60].

Prediction of Gait intention from pre-movement Electroencephalography (EEG) signals is a vital step in developing a real-time BCI for a proper neuro-rehabilitation system (see Fig. 1.5). Shafiul Hasan et al. propose the feasibility of a fully predictive method that detects the intent to start and stop gait cycles by using EEG signals obtained before the event [57]. They customized an 8-channel EEG system with electrodes placed around the sensorimotor cortex of the subject's head. EEG signal extraction was used to capture information related to alpha and beta band events in the frequency domain using a discrete wavelet transform-based method. The feature set was then classified using a support vector machine (SVM) classifier with an RBF kernel in a tenfold cross-validation scheme for the "walk vs. stop" and "rest vs. start" categories.

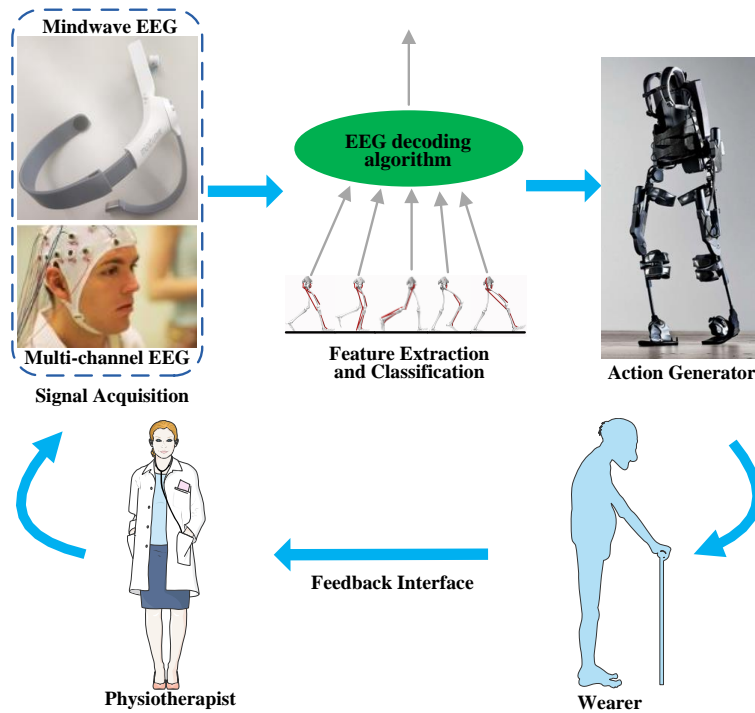


Figure 1.5 Architecture for clinical gait analysis based on BCIs.

EEG signal acquisition equipment: Electroencephalography (EEG) is a non-invasive technique used to detect and record the sum of voltages generated on the cortex by cortical activity. Unlike the invasive methods of inserting electrodes or implanting parts of the brain for behavioral observation, EEG can be applied to humans without ethical controversy. Different from medical imaging techniques (like fMRI), EEG recordings have a high time resolution and are therefore mainly used to detect event-related potentials that last only a few milliseconds. The EEG electrode cap records the amplitude potential difference between the active electrode on the scalp and the reference electrode. The active electrode on the EEG electrode cap usually follows the 10-20 international system, as shown in Fig. 1.6.

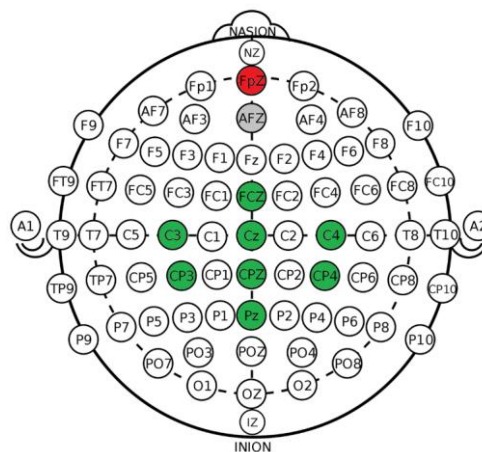


Figure 1.6 EEG Electrode Montage Corresponding to the International 10-20 System.

The parameters of some EEG amplifier equipment manufacturers and main products are shown in Table 1.2.

Table 1.2 Part of the EEG acquisition equipment parameters.

Company Name	Device Name	CMRR	Bandwidth	Sample Rate
NeuroScan	SynAmps 2	110	DC-3500 Hz	20000 Hz
EGI	NetAmps 300	120	DC-4000 Hz	20000 Hz
Brain Products	DC	120	DC-4000 Hz	1000 Hz
Symtop	UEA	98	0.5-120 Hz	1000 Hz

1.2.3. Challenges

As a part of a gait analysis protocol, the SEMG is being more and more frequently applied to clinical problems. The development of proper tools to facilitate data comparison and quantitative description of SEMG locomotor patterns will possibly contribute to a more effective use of kinesiological electromyography. For this purpose, one important aspect is the need to harmonize the recording techniques in terms of electrode positioning, signal conditioning and filtering, data reporting, and parameters' extraction [48]. EMG methods cannot be used as input to LLER robots; for example, patients with complete lower limb paralysis may not be able to use devices such as exoskeletons because it is difficult to obtain control signals from the muscles of the paralyzed limb. On the other hand, as technology advances, BCI (brain-computer interface) or BMI (brain-machine interface) has attracted the attention of the bio-robotics field. Brain-machine interface can open up new ways to directly decode the user's brain signals to control devices such as prostheses, exoskeletons or wheelchairs; for example, even if the user's limbs are not capable of any adequate movement, he/she can still generate commanding brain signals that can be used in this brain control interface to drive an exoskeleton. However, BCI/BMI using only EEG signals as the primary input has not been fully accepted in bio-robotic applications due to the difficulties of EEG such as low reliability, low accuracy, poor user adaptability and low data transmission rate. Therefore, the low accuracy of EEG decoding and the design of effective paradigms for MI are problems that hinder the application of EEG in rehabilitation devices.

1.3 Lower limb exoskeleton rehabilitation robots: state-of-the-art

In the nearly six decades since researchers began to explore methods of creating them, exoskeletons have progressed from the stuff of science fiction to nearly commercialized products. While there are still many challenges associated with exoskeleton development that has yet to be perfected, the advances in the field have been enormous [61].

In this section, we review the history and discuss the state-of-the-art of lower Limb exoskeletons and mobile orthoses. We provide an overview of the design of the three main types of lower Limb exoskeletal rehabilitation robots (see Table 1.3) described in the literature and conclude with a discussion of the major advances that have been made and the obstacles that remain to be overcome.

1.3.1 Lower limb exoskeleton rehabilitation robot

Exoskeletons are wearable robotic systems that integrate human intelligence and robot power. At present, the mainstream lower limb rehabilitation robots have the forms of sitting, suspension and walking assistance. Typical lower limb exoskeletons are used for gait rehabilitation, human movement assistance and human strength enhancement[16]. The Ekso (see Fig. 1.7A) lower limb

exoskeleton rehabilitation robot is the most representative rehabilitation device, the user usually needs a sling to hold the pelvis, allowing patients with lower limb movement disorders to achieve the function of walking on a simple flat surface. However, this type of rehabilitation robot is usually expensive, in addition, the configuration of the lithium battery in the back increases the burden on the wearer.

Table 1.3 Design of some Institute exoskeleton robots.

Institute (Country)	Name	Use	DOF/Actuator	Actuator/Output Force	Sensors	Control Algorithm
Florida Institute for Human and Machine Cognition (USA)	IHMC mobility assist exoskeleton	Paralysis patients	Hip:A-A-U Knee:A Ankle:U- U-U	RSEA: Moog BN3425EU-02 brushless motor+harmonic reducer (100:1); Output torque:80Nm	Optical rotary encoder, Linear encoder, Foot switch	Position control, Force/torque control
Saga University (Japan)	Lower-limb power-assist exoskeleton	Lower limb weakness daily use	Hip:A-N-N Knee:A Ankle:U- N-N	Maxon DC motor	Encoder, Force sensor, EMG sensor, Laser ranging sensor, plantar contact sensor	ZMP stability control, Conscious recognition based on EMG signal, Ability to perceive to environment
University of Tsukuba (Japan)	HAL-3	Patients with lower-limb paralysis	Hip:A-U-U Knee:A Ankle:U- U-U	DC servo motor + harmonic reducer DC	Plantar pressure sensor, Angle sensor, Gyroscope	Conscious recognition based on plantar pressure and torso angle
Nagoya University (Japan)	WPAL (Wearable Power-Assist Locomotor)	Patients with lower limb paralysis	Hip:A-N-N Knee:A Ankle:A- N-N	DC servo motor	Three axis angular acceleration sensor, Plantar pressure sensor, Encoder	Swing phase step trajectory control of lower limb
University of Delaware (America)	ALEX	Stroke patients	Hip:A-U-U Knee:A Ankle:U- U-N	Linear actuator Peak torque: 50Nm	Encoder, Force-torque sensor, Foot switch	Human-robot coordination
Centre for Automation and Robotics (Spain)	ATLAS	Quadriplegic patients	Hip:A-N-N Knee:A Ankle:U- N-N	Brushless Maxon motor + harmonic reducer Peak torque:57Nm Average torque: 32Nm	Plantar pressure distribution sensor, Angle sensor	CoP stability control, Conscious recognition
Ekso BIONICS Inc. (USA)	Ekso GT™	Spinal cord injury, multiple sclerosis, Green-Barré syndrome	Hip:A-A-U Knee:A Ankle:U- U-U	Adopt advanced behavior-driven	Pressure sensors and gyroscopes	Follow-Up and Self-Balancing

Hip joint degrees of freedom sequence: flexion/extension, ab/ad-duction, rotation;

Ankle joint degrees of freedom sequence: plantar/dorsal flexion, in/e-version, pro/supination;

A-actuated, U-unactuated, N-no DOF.

The LLR-II Rehabilitation is a seated rehabilitation device in which the robot drives the affected limb to perform rehabilitation training. This type of rehabilitation robot can be used without considering the change in the position of the center of gravity. Such rehabilitation robots can realize active rehabilitation training mode in which the affected limb drives the movement of the exoskeleton robot and passive rehabilitation training mode in which the exoskeleton drives the

movement of the affected limb according to the preset movement trajectory. The robot modeling approach uses joint space planning, that is, the planning of each joint is realized by calculating the interpolation points of each joint angle. Moreover, the LLR-II rehabilitation is equipped with joint torque sensors and six-dimensional force sensors on the foot soles. In the training task, man-machine interaction force information is collected, from which can be extracted characteristic quantities to predict the task difficulty by using support vector machines.

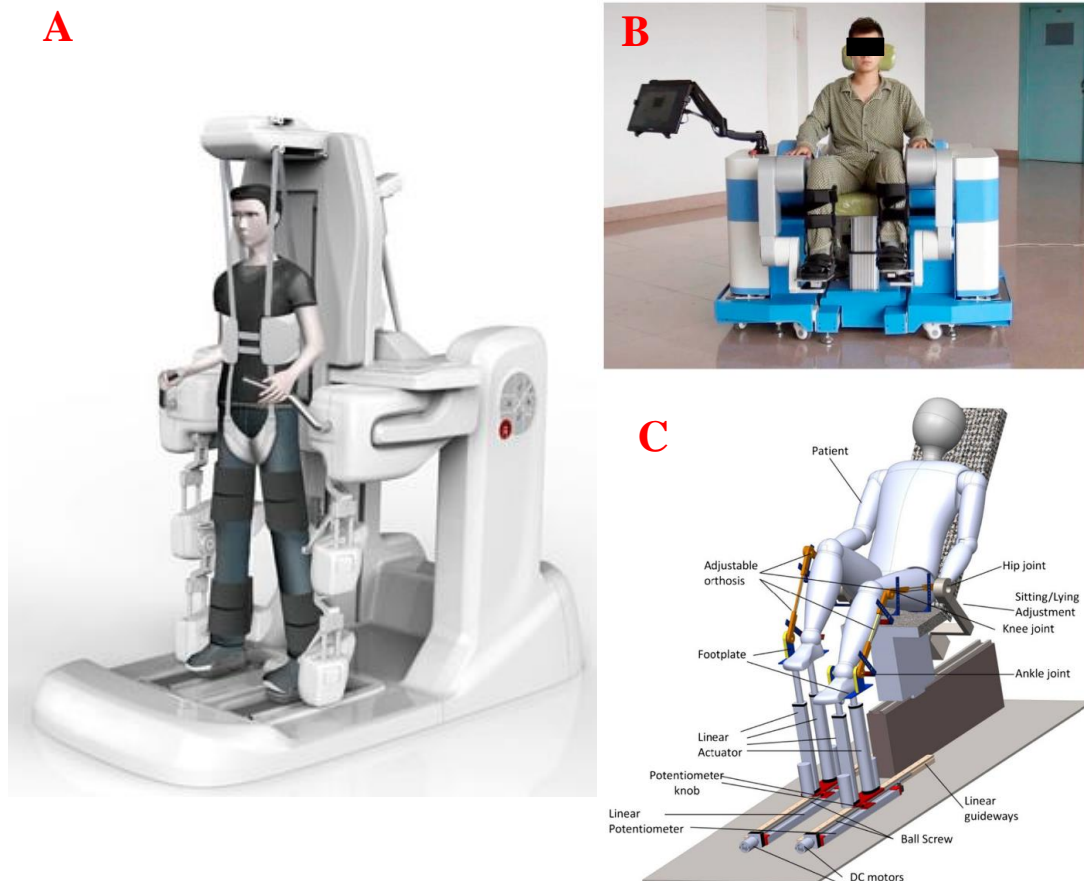


Figure 1.7 Three types of lower limb exoskeleton rehabilitation robots. (A) Upright rehabilitation robot [19], (B) The LLR-II Rehabilitation [62], and (C) Planar parallel lower limb rehabilitation robot [63].

Plane-parallel type rehabilitation robots, mainly use motion planning in Cartesian space, namely, planning the end trajectory in Cartesian space and then solving the inverse for each interpolation point to calculate the angle corresponding to each joint. Vasanthakumar, M et al. [63] developed a planar hybrid 1P-2RP robot for lower limb rehabilitation applications that combines the advantages of both serial and parallel manipulators, and validated the proposed robust sliding mode control through rigorous experiments by varying the control parameters. The optimal combination of the controller parameters obtained by parametric sensitivity analysis in the presence of external disturbances and parameter uncertainties is achieved, with the task space position error within $2mm$ of the whole trajectory in magnitude. Thus, the proposed control scheme is suitable for lower limb rehabilitation applications, especially for stationary trainers. Jezernik et al.[64] developed the robotic orthotic Lokomat, a rehabilitation robot developed to

train spinal cord injury and stroke patients on a treadmill as a motor automation device. The Ekso GT exoskeleton [65] developed by Ekso Bionics is a wearable exoskeleton suit designed for the assistance and rehabilitation of patients with various levels of lower limb weakness. It is suitable for rehabilitation training for patients with lower limb mobility.

LLER robots are primarily developed for three types of applications. The first application focuses on gait rehabilitation (i.e. helping patients with mobility disorders in the rehabilitation of musculoskeletal strength, motor control, and gait). The second application is human locomotion assistance, which is targeted at paralyzed patients who have lost motor and sensor function in their lower limbs. Assistance from exoskeletons enables these patients to regain the ability to stand up, sit down, and walk, just as an able-bodied person [66]. The third application of exoskeletons is aimed at enhancing the physical abilities of able-bodied humans (i.e. human strength augmentation) [67].

1.3.2 Challenges

According to literature investigation, the main challenges regarding lower limb exoskeleton rehabilitation robots are divided into the following areas.

1. The power supply, lightweight actuators, and efficient transport are among the many issues that all researchers in the field of exoskeleton rehabilitation robotics would have to face. Obviously, especially for those at more advanced stages of exoskeleton development, for many power, actuator, and other subsystems, the off-the-shelf components do not meet the low weight, high efficiency, and other criteria needed to achieve their design goals [68]. Indeed, it is a problem faced by many areas of mobile robotics, especially those with anthropomorphic architectures. The field of biomechanics for human motion has matured in recent decades, providing the necessary background science for designing devices with dynamics very similar to those of the operator's motion. And of course, the latest technological advances in computation, sensing, and control have advanced so rapidly that these areas are no longer major obstacles to the implementation of robotics hardware.
2. There is a lack of published quantitative studies on the effects of exoskeletal devices that have been reported to improve human locomotion on the affected limb. In addition to motor performance as assessed by metabolic cost, other performance metrics applicable to these types of systems including reduced forces on the musculoskeletal system, reduced muscle fatigue, and improved bipedal stability all necessitate long-term follow-up measurements for analysis. Of course, there are many design challenges that may contribute to poor exoskeleton performance: joint mismatch between the operator and hardware, kinematic constraints from accessories such as the safety belt and fixation straps, designs that are not optimized for weight-bearing gait [69], increased operator forces to resist motion, and suboptimal adding power, etc. However, all of these problems are difficult to solve and there are many opportunities for basic research to deal with these challenges.
3. Lower limb exoskeleton rehabilitation robots also face the daunting problem that the specific nature of the disability varies from patient to patient. This makes it difficult to develop a device that is universally applicable. In fact, this is a challenge for many assistive devices. Therefore, the development of customized rehabilitation modules for the clinical gait analysis of different patients is necessary.

4. An improved understanding of muscle and tendon function in walking and other locomotor tasks may contribute to understanding more effective exoskeletal leg structures. Gait models based on actual machine components that capture key features of human motion could enhance understanding of human leg morphology and control, and lead to similar improvements in efficient, low-mass exoskeleton design [70].

1.4 Research program of the thesis

Patients with lower limb dyskinesia due to stroke and other diseases have the potential to remodel their motor nerve function. They can usually be rehabbed with the help of rehabilitation equipment. Impressive results of the rehabilitation robot trajectory have also been achieved by controllers based on tracking motion capture data [71][72][73][74]. However, as with methods that tune joint trajectories or controller parameters by hand, motion capture driven controllers have a limited ability to predict changes in gait. For the lower limb rehabilitation training performed by this type of patient, this article proposes a novel approach of clinical gait analysis based on predictive assessment for the exoskeleton rehabilitation robot. The approach involves not only the passive training pattern of the affected limb in the early stages of rehabilitation, due to weak muscle strength (Chapter 3) but also the active training pattern of the affected limb in the middle and late stages of rehabilitation (Chapter 4). Aiming to adapt the lower limb exoskeleton device to the rehabilitation training requirements of different affected limbs, this article proposes to implement clinical gait analysis by an approach of forward kinetic predictive assessment simulation. Therefore, we will focus on the relationship between the predictive assessment model and the influence of the knee joint during the gait cycle in rehabilitation training. The goal is to reproduce the diseased gait of the affected limb and gradually achieve a normal gait after the parameters are adjusted by the psychotherapist. The framework not only avoids secondary injuries to the affected limb caused by a large range of rehabilitation actions, but also reduces the patient's discomfort and improves resistance to rehabilitation training.

In this article, we simulate pathological gait by predicting forward dynamics, using energy efficiency as a high-level objective (using minimizing the total cost of transport within a self-selected speed while ensuring head stability as a high-level goal), and the gait controller uses a combination of state machines and low-level control laws to determine the excitation, calculating the optimal trajectory of motion to perform a given task and seeking the relationship between the influence of the muscle-tendon system on pathological gait. We systematically introduce the isolated BFSH muscle group into the musculoskeletal model as an example of knee dyskinesia in order to predict gait adaptation due to deficits in this muscle group. We apply mild, moderate and severe muscle weakness or contracture to the BFSH and retrained the model to walk at a self-selected speed to recreate pathological gait without experimental data and obtain more realistic changes in knee parameters. Then, we attempted to explore the characteristics for reproducing the patient's gait just by modifying the parameters of the model muscles. Therefore, mild, moderate and severe muscle weakness or contractures were applied to the HAMS, GAS and BFSH muscle groups, respectively, and the models were trained to walk at self-selected speeds. Finally, we developed an impedance control model for the lower limb exoskeleton rehabilitation robot: we adopted the knee joint angle and torque parameters optimized by using predictive forward dynamics simulation as the desired values for the robot in order to achieve customized tuning for the robot motion trajectory.

This approach obtains as realistic a model of pathological gait as possible by studying the effect of muscle weakness or contraction of injured muscle groups on walking, and feeds the changed parameters such as angle, angular velocity and torque of each joint of the optimized model into the exoskeleton rehabilitation robot controller as feedback parameters to achieve customized passive training motion trajectories. This not only realizes progressive rehabilitation training, but also increases the comfort of the wearer and alleviates the rebelliousness of the patient.

The goal of our work is to enhance the realism of locomotion gaits exhibited by physically-simulated humanoids without dependence on motion capture data. To this end, we augment the joint-actuated humanoid model with a set of Hill-type musculotendon units (MTU). These musculotendon units generate torques for the most important degrees of freedom (DOF) during locomotion: the sagittal plane hip, knee, and ankle DOF. To actuate these muscles, we define biologically-motivated control functions that map the current state of the body (joint angles, muscle fiber lengths, etc.) to excitation signals. The parameters of these functions are optimized to yield gaits that move the character forward without falling down. The comparison of the predictive assessment module with the LLER robot approach to implementation is shown in Fig. 1.8. The musculoskeletal model used for the predictive dynamic simulation is based on an adult, approximately 1.8m in height and 75.2kg in weight, used to simulate lower limb gait. The model is driven by 18 Hill-type musculoskeletal units with nine per leg [28]. The lower limb exoskeleton robot is based on controller system, actuator system, sensor system, power supply and exoskeleton robot mechanism. Sensor systems include surface electromyography (SEMG) sensors, piezoelectric sensors, encoders and posture meters.

To achieve the above description, the framework we developed needed to solve the following problems.

- A. By predicting the forward dynamics to model pathological gait, the gait controller combines high-level state machines and low-level control laws to determine the excitation and calculate the optimal motion trajectory to perform a given task, seeking the relationship between the effects of the musculotendinous system on pathological gait.
- B. 2. Construct an exoskeleton robot model based on impedance control strategy, develop PD control algorithm with gravity compensation and LLER robot controller with robust adaptive algorithm, respectively, to realize and optimize the trajectory tracking in passive training mode. Develop the impedance controller with variable parameters, and adjust the impedance parameters according to the rehabilitation status of the affected limb, which can make the LLER robot exhibit damping and flexibility.
- C. 3. Combining A and B, the optimization results of the predictive assessment mentioned in 1 (parameters such as angle, angular velocity and torque of each joint of the robot) are used as input data for the control system of the exoskeleton robot mentioned in 2. Realize the design of corresponding robot rehabilitation movement patterns for different pathological gait patterns when performing passive training with the help of the LLER robot.
- D. In the middle and late stages of rehabilitation training, the affected limb needs to undergo active training with the help of the LLER robot. By applying the multi-sensor integration

(EEG and EMG sensors) based on motor imagination, we can obtain the accurate intention of the trained person in multiple ways, so that the patient can perform autonomous rehabilitation training in the middle and late stages of rehabilitation, and help the motor nervous system to achieve the reconstruction as soon as possible.

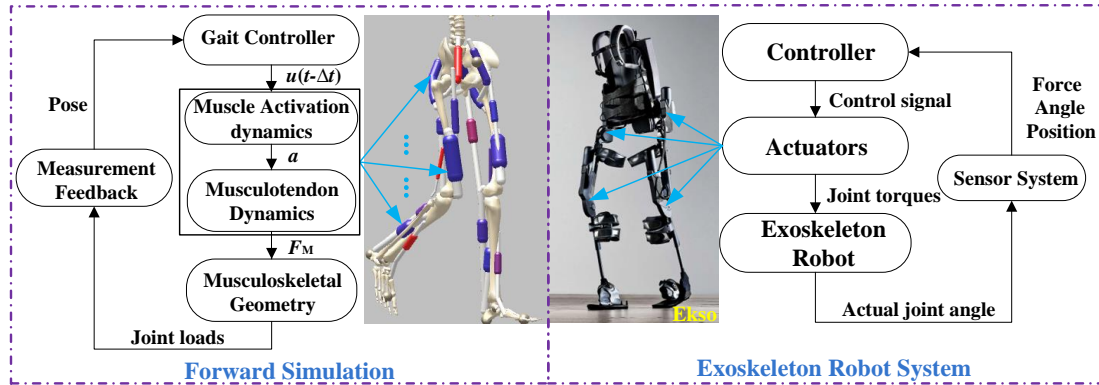


Figure 1.8 Comparison of predictive forward dynamic simulation and LLER robot.

Advantages of the framework: a. Through gait diagnostic analysis, the intrinsic cause of the affected limb can be considered more accurately; b. Because it is a predictive model construction, it does not return to cause trauma to the patient; c. To avoid the patient's inaccurate subjective judgment leading to unsatisfactory rehabilitation results; d. In the initial stage of rehabilitation with the help of the robot for passive training, it can be adapted to different pathological gaits and obtain appropriate rehabilitation actions to avoid secondary injuries caused by excessively large rehabilitation actions in passive training.

1.5 Organization of the thesis

The remainder of the thesis is organized as follows: Chapter 2 presents the general framework of the lower limb exoskeleton rehabilitation robot, the passive training-based predictive simulation assessment and the active training-based multi-sensor fusion framework. Followed by Chapter 3, the predictive dynamic modeling of the BFSH muscle-tendon system is presented as an example and the relationship between its influence on the gait cycle is described and the relationship between the impact of HAMS, GAS and BFSH on the knee joint is summarized. Chapter 4 presents an MI-based intent detection module for patients with multimodal integration for driving rehabilitation robots for more accurate active training. Chapter 5 introduces the human-robot system model, establishes the exoskeleton robot model based on impedance control strategy, designs different intelligent algorithms to optimize the model, and combines Chapter 3, the knee joint parameters optimized by the predictive assessment are used as input parameters for the pre-passive training of the rehabilitation robot. Chapter 6 presents a conclusion, including our contributions and future work and expectations. Next is the reference list used in this thesis.

Chapter 2. Overall Framework

This article presents a novel approach to clinical gait analysis based on predictive assessment for the exoskeleton rehabilitation robot, which mainly includes a predictive simulation-based clinical gait assessment module and a rehabilitation robot controller module for different application scenarios. In addition, a patient intent detection module with multi-mode integration applied to the active training mode is proposed to enhance motor neural remodeling. From our study and findings from the literature, we suggest that the use of hybrid interfaces may be the key to enhancing the usability of technologies restoring or assisting the locomotion of a wider population of patients in clinical applications and outside the laboratory environment.

2.1 The overall framework of the system

The overall framework involves the predictive assessment module and the LLER robot controller. The predictive assessment module is a novel approach to clinical gait analysis, which can reproduce the patient's pathological gait by simulation and can calculate various parameters of the model during the gait cycle. The physical therapist is allowed to select the expected values of the desired parameters as the LLER robot controller to achieve customized robot trajectory planning. In order to make the interface between the predictive assessment module and the robot more accurate and safe, we require the help of a physical therapist.

2.1.1 Predictive Assessment Module

In this thesis, the pathological gait is simulated by the predictive forward dynamics with energy efficiency as the high-level goal. The gait controller uses a combination of state machines and low-level control laws to determine the excitation, aiming at calculating the optimal motion trajectory to accomplish the given task and ultimately seeking the relationship between the impact of the tendon system on the pathological gait.

First, we tried to systematically introduce the isolated BFSH muscle into the musculoskeletal model as an example of knee dyskinesia in order to predict gait adaptation due to the lack of this muscle group. We apply mild, moderate and severe muscle weakness or contracture to the BFSH and retrained the model to walk at a self-selected speed to recreate pathological gait without experimental data and obtain more realistic changes in knee parameters. The framework obtains the realistic pathological gait model by studying the effect of muscle weakness or contraction for injured muscle group on walking, and then inputs optimized parameters (angle, angular velocity, and torque, etc.) into the exoskeleton rehabilitation robot controller as feedback in order to achieve customized passive training motion trajectories.

The results of the study on the relationship between the effects of BFSH on the knee joint during the swing phase have given us more confidence in the study on the effects of each major muscle group on the knee joint during its movement in the gait cycle. We attempted to explore the characteristics for reproducing the patient's gait just by modifying the parameters of model muscles. Therefore, mild, moderate and severe muscle weakness or contractures were applied to the HAMS, GAS and BFSH muscle groups, respectively, and the models were trained to walk at self-selected speeds. The obtained predicted simulation results for the normal gait need to be verified by experiments. After analyzing the optimization results for different severity levels, the

modification rules are summarized. In other words, by studying the relationship between the model's muscles and gait, the final goal is to build a library of modification rules.

The structure of the rehabilitation framework based on predictive assessment (see Fig. 2.1) includes clinical gait analysis based on predictive assessment and a multimodal controller for the exoskeletal rehabilitation device. The yellow area (see Fig. 2.1) indicates the clinical gait analysis. First, the patient needs to undergo a detailed clinical diagnosis to ensure that the conditions described in chapter 2.2.2 are met. Next, the physiotherapist modifies the parameters of the predictive assessment model according to the modification rules in relation to the damage of the affected limb, and uses the SCONE software to reproduce the simulation of the pathological gait, while obtaining the motion parameters of each joint during the gait cycle. Finally, the physiotherapist increases the offsets of the joint motion parameters according to the condition of the affected limb. These data will be used as input expected values for the controller of the exoskeleton rehabilitation device to guide the device to perform customized trajectory tracking for passive training.

2.1.2 LLER Robot Controller

LLER devices can be single joint motor rehabilitation devices, multi-joint rehabilitation centers or assisted walking rehabilitation robots (like the Ekso robot[75]). The joint movement control of these devices requires the integration of impedance control and some intelligent algorithms (e.g. particle swarm optimization algorithms or fuzzy neural networks), the former to achieve the damping effect and elasticity effect of the joint movement and the latter to achieve the tuning of the impedance control parameters.

The multi-modal integrated human Intent recognition module based on MI (see the bottom of Fig. 2.1) is applied to the active training mode of the LLER robot. The main features of this model are: 1. After the preliminary passive training, the motor nervous system of the affected limb has been gradually reconstructed; 2. After the preliminary training, the activation of some muscles of the affected limb has been restored and can show normal muscle activation. Based on this, the human intent recognition module mainly consists of two parts: the EEG intent signal acquisition module based on MI and the SEMG-based motor command correction module. Among them, the MI-based EEG intent signal acquisition module relies on the passive training in the pre-rehabilitation period to generate an effective EEG signal of MI which drive the LLER robot to execute the pre-programmed trajectory training. The SEMG-based motor command correction module is based on fixing EMG dry electrode sensors to the muscle region of the affected limb with activation capability. By detecting muscle activation with the EMG sensor, SEMG module corrects the intended control commands after EEG acquisition and processing. Only when the EEG driving command and SEMG muscle activation command are satisfied at the same time, the control command of the LLER robot is valid. Otherwise, it will be considered as an invalid control command.

Overall, the functional design of the controller should be developed to meet the actual rehabilitation training needs, while the specific mechanical form of the exoskeleton rehabilitation robot is not specifically requested by this framework. In addition, this module requires that patients have an initial diagnosis to ensure that their central nervous system has the potential to recover. The physical therapist needs to be involved in the whole process, not only to choose the

modified plan according to the pathological gait, but also to adjust the parameters of the robot controller according to the rehabilitation process to guarantee the rehabilitation safety and improve the rehabilitation effect.

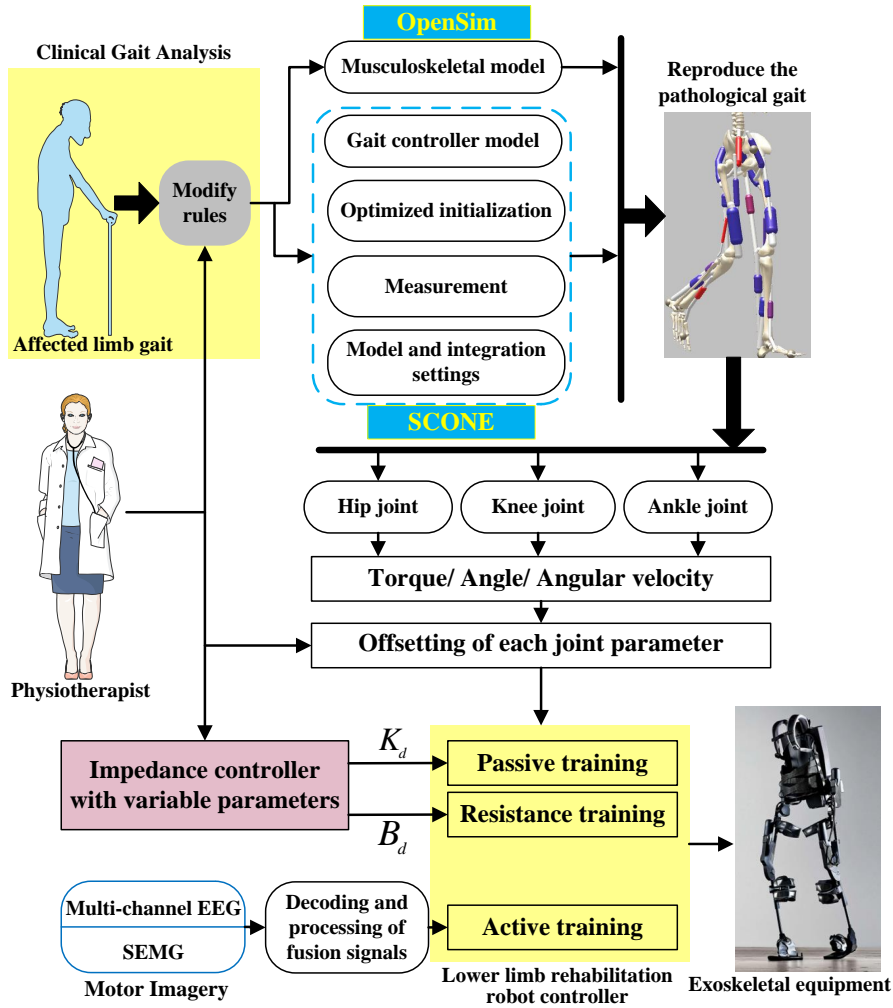


Figure 2.1 Architectural of the rehabilitation framework based on predictive assessment.

2.2 Framework functionality and preliminary considerations

The framework presented in this article is focused on the affected limbs with lower-limb paralysis due to stroke. Such patients usually show that their locomotor nervous system can be remodeled by external stimulation. Moreover, the residual muscle strength of the affected limb is usually weak during the initial stage of rehabilitation. In addition, patients who suffer from long-term lower limb dyskinesias, their muscles, tendons and bones are all susceptible to secondary injuries in the early stages of rehabilitation training. Therefore, we propose to provide the user with as much scope of applications as possible.

2.2.1 Framework functionality

Lower limb rehabilitation training mode is divided into passive training, active training and resistance training. Because resistance training is mainly applied in the later stages of rehabilitation, and it is non-powered training, similar to fitness equipment. Therefore, this paper

focuses on passive training and active training.

(1) Passive training mode: the robot controller mainly through position control, to achieve the exoskeleton robot to drive the affected limb to execute the pre-defined joint movement trajectory training mode. This mode applies to the early stage of rehab training.

(2) Active training mode: the exoskeleton robot by acquiring the patient's motor intention. That is, the patient undergoes a period of MI training, such as start and stop, then the acquisition of EEG signals through BMI decoding and machine learning algorithms to extract a more accurate locomotion intent. Meanwhile, the robot receives the real-time accurate posture of the lower limb obtained by multi-sensor fusion of EMG sensors, pressure sensors and IMU. All these information form the high-level control commands of the lower limb exoskeleton rehabilitation robot, which are combined with the preset commands of the robot controller itself to perform the active training mode. This mode is suitable for the early and middle stages of rehab.

(3) Resistance training mode: The rehabilitation device is not connected to the actuator, the muscle strength drives the rehabilitation device to move. This mode is usually applied in the case of significant improvement of muscle strength in the later stage of rehab.

The lower limb exoskeleton rehabilitation robot based on variable parameter impedance controller is mainly composed of robot kinematics and dynamics modeling, impedance controller design and parameter tuning. The yellow blocks (see Fig. 2.1) indicate the stored files of the model. The blue lines represent the need for human intervention and manipulation. In this article, one of the main tasks is to establish the modification rules for the knee joint in gait cycle. This framework not only improves the rehabilitation training effect but also increases the comfort of the wearer and alleviates the rebelliousness of the patient.

The predictive forward simulation module has three main data files: *Model.osim*, *InitialFile.par* and *Measures.scone* (see Fig. 2.2). The model files are the muscle-tendon geometry and the muscle-tendon actuated model, and the initialization files defined the initial values and thresholds of parameters. For instance, by changing the pelvis velocity along the x-axis direction, it is possible to have the model walk at different speeds.

This framework is a clinical gait analysis using a predictive assessment approach. It has the advantage of not only reducing the cost of diagnosis but also allowing rehabilitation equipment to achieve different gait tracking trajectories based on different pathological gait. However, it is not accurate to reproduce pathological gait through simulation, but as a new approach to rehabilitation training, it can be improved with the help of the physiotherapist. At least this approach can make the patient feel comfortable during the rehabilitation training and also can improve the rehabilitation effect.

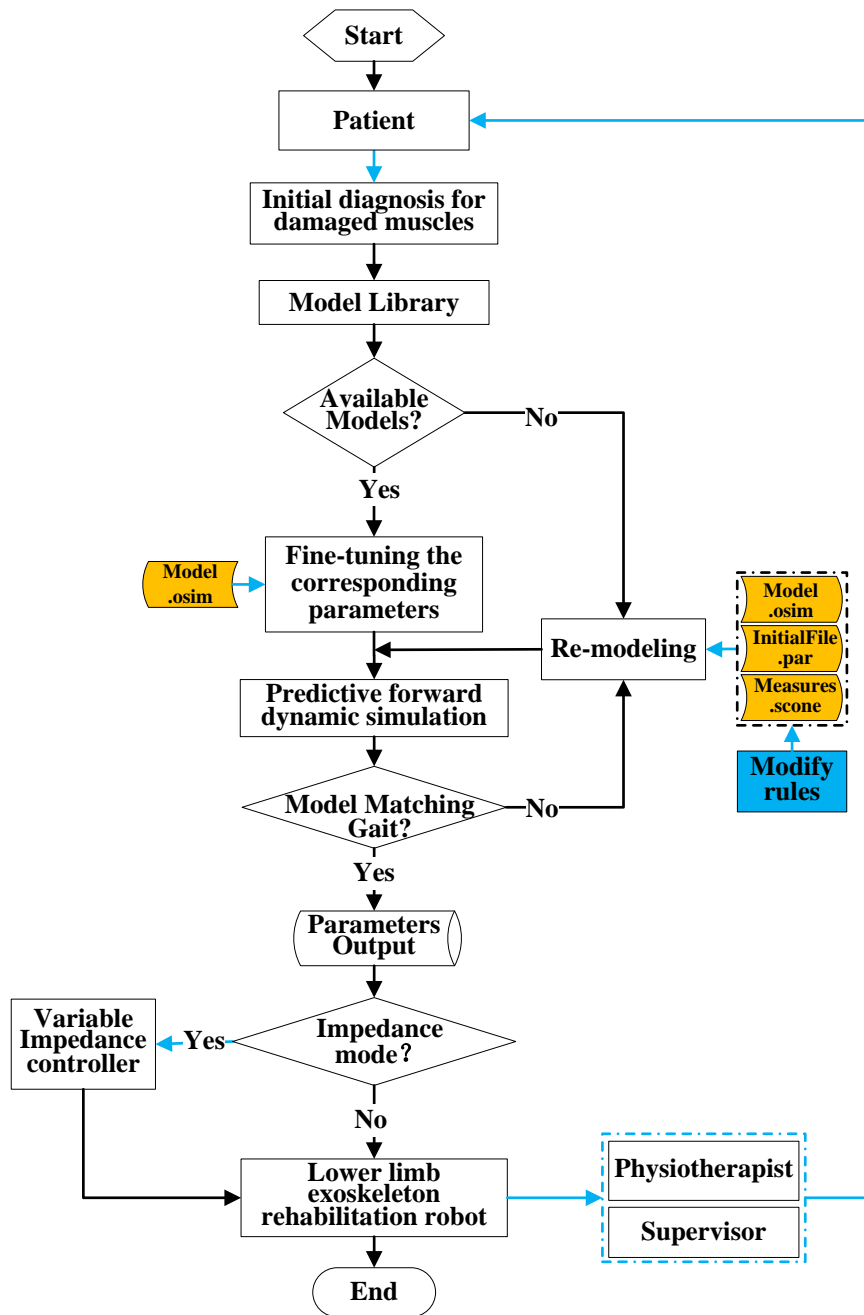


Figure 2.2 Flow chart of LLER robot framework based on predictive forward simulation.

2.2.2 Intended use of the framework

Exoskeleton robots for clinical rehabilitation are currently facing a high risk of using the equipment. Once a patient falls or has another accident, the health care worker may lose his or her career or the hospital faces the risk of huge compensation. Therefore, we refer to the Ekso[75] robot and make the following reference requirements for the objects to whom the framework applies.

- People with lower limb weakness or paralysis due to neurological disease or injury such as: Spinal cord injuries, stroke, Multiple Sclerosis, and Guillain Barre Syndrome.

- Spinal Cord Injuries, Multiple Sclerosis, and Guillain Barré syndrome.
- The patient should be conscious and able to cooperate fluently with the physical therapist for rehab inquiries.
- Not suitable for those with emotional resistance to rehabilitation training.
- A complete evaluation and screening by a medical provider before using the device.
- Not available for patients with unresolved deep vein thrombosis (DVT).
- Not suitable for patients with severe osteoporosis. Because it can prevent safe standing or may increase the risk of fractures due to standing or walking.
- Not indicated for patients with uncontrolled spasticity.
- Not for patients with uncontrolled autonomic dysreflexia (AD).
- Skin integrity issues on the contact surface of the device or the prohibition of sitting need to be evaluated before they can be applied.

In addition to the above requirements, when the rehabilitation robot hardware is designed at a later stage, the requirements should be based on the actual situation, with the aim of ensuring the safety of the user.

2.3 Impedance control system for LLER robot

The controller of the LLER robot consists of 2 parts: 1. the passive training controller of the LLER robot for the affected limb in the pre-rehabilitation period; and 2. the active training controller of the LLER robot in the mid-and late-rehabilitation period. In fact, the preliminary development of the active training controller for the LLER robot involved in this article only performs a single-step operation of the passive training controller. That is, the multi-mode integrated intent sensor acquires and processes the MI signal and then triggers the LLER robot active controller to execute one motion cycle. Therefore, for the development of the LLER robot controller, we focus on the passive training stage.

Patients with lower extremity motor dysfunction due to stroke and other diseases usually carry out passive rehabilitation due to weak residual muscle strength in the lower extremity. This is characterized by the fact that the implementation of customized clinical gait analysis is necessary because of the wide variability of the affected limb, the emotional impact of the patient's rehabilitation, and other factors. After recreating the gait of the affected limb using the forward kinetic predictive assessment module, the patient is taken from a pathological gait and gradually completes rehabilitation training after the physical therapist sets the corrected offset values based on the rehabilitation of the affected limb. At the same time, it reduces the patient's pain during rehabilitation training, eliminates the patient's resistance to rehabilitation training, and also ensures the safety of rehabilitation training and prevents secondary injury to the affected limb caused by muscle strain.

To meet these characteristics and to reduce the development cost, we developed a PD controller with gravity compensation. The simulation results show that the trajectory tracking can be basically completed, but the robustness is poor. Aiming at this problem, we then developed a robust adaptive PD controller, and the simulation results showed that the controller could greatly

improve the robustness of the system. Finally, in order to improve the human-robot interaction, we developed the impedance controller with variable parameters of gravity compensation, and the simulation results showed that the LLER robot can achieve different damping and elasticity when the physiotherapist sets different damping and stiffness values, so that the LLER robot can be more adaptable to the complex rehabilitation needs.

2.4 Conclusion

This chapter presents the overall framework of clinical gait analysis based on predictive assessment applied to the LLER robot, including the overall structure and intended use of the framework. The framework contains the predictive assessment module and the LLER robot controller. The predictive assessment module is used to reproduce the patient's pathological gait using forward dynamics simulation for clinical gait analysis. The assessment results could be used as the expected values for the LLER robot, realizing customized trajectory planning. For the LLER robot controller, depending on the passive training in the pre-rehabilitation period, a PD controller with gravity compensation, a robust adaptive controller, and an impedance controller with variable parameters were developed. Depending on the active rehabilitation training in the middle and later stages of rehabilitation training, a multimodal integrated detection module based on MI was developed.

Chapter 3. Predictive Assessment in Passive Training for Rehabilitation

In the initial stage of robot-assisted rehabilitation training, the passive training modes are normally applied mainly due to the weak residual muscle strength of the affected limb: the rehabilitation robot drives the affected limb to perform constant rehabilitation movements through pre-set parameters. In order to develop a framework to solve the problem of obtaining adapted rehabilitation movements for different pathological gait patterns and to avoid secondary damage to the affected limb due to the excessive amplitude of non-variable passive training rehabilitation movements.

3.1 Predictive Dynamics

Although multi-parameter controllers are capable of human-like lower limb gait locomotion, they are highly influenced by the parameters. To produce a gait with a high degree of realism, Ackermann et al. [76] used a goal based on minimizing metabolic energy expenditure, thereby selecting the most relaxed gait for the gait task. Human or animal metabolism is estimated by oxygen consumption, Anderson [77] used a biologically based MTU driver to estimate metabolic energy expenditure. The result is a motor control optimization program that minimizes physiologically based goals within a parameter space limited to biologically plausible torque patterns.

Musculoskeletal simulations built from experimental gait data have been used to study gait pathologies. For example, simulations of individuals with cerebral palsy have quantified individual muscle contributions to body weight support and forward propulsion [78], the minimum muscle strength required to walk in a crouch gait [79], and the contributions of contracture and spasticity to increased hamstring resistance [39]. These studies suggest strong links between muscle deficits and the observed gait adaptations; however, since these studies tracked experimental data from patients with a combination of muscular, skeletal, and neural deficits, the independent effects of muscular weakness and contracture on the observed gait adaptations cannot be assessed.

The goal of our work is to determine which knee gait adaptations during the gait cycle are caused by weakness or contracture of the HAMS, GAS and BFSH muscles. To this end, we first created and validated an optimization module and musculoskeletal model that could generate realistic motion from scratch. Our controller follows the reflection-based controller described previously [80][81], and the parameters of our controller are iteratively updated within the optimization module.

Our framework consists of a predictive dynamic simulation and an LLER robot (see Fig. 2.2). Predictive dynamics use a shooting method to solve the dynamic optimization problem for generating a gait simulation. We implement the musculoskeletal model in OpenSim 3.3, which is actuated by 18 Hill-type musculoskeletal units, nine for each leg. We use an optimization and control framework (SCONE) to implement gait controller based on an objective function that sought to minimize metabolic cost, update the variable values of the optimization problem using the Covariance Matrix Adaptation Evolutionary Strategy (CMA-ES), then output the optimized

joint variables to the controller of the lower limb exoskeleton rehabilitation robot, enabling the sharing of parameters between the two modules.

3.1.1 Methods

Our optimization module used a single shooting method to solve the dynamic optimization problem of generating a simulation of gait. We implemented our model in OpenSim3.3 [35] and used an optimization and control framework (SCONE) [82] to implement the gait controller, perform the simulation using OpenSim as the plant, and optimize the parameters of our problem.

OpenSim has the following functions. First, the software can calculate variables that are difficult to measure experimentally, such as the forces generated by muscles and the stretch and recoil of tendons during movement. Second, OpenSim can predict novel movements from models of motor control, such as kinematic adaptations of human gait during loaded or inclined walking. Changes in musculoskeletal dynamics following surgery or due to human–device interaction can also be simulated; these simulations have played a vital role in several applications, including the design of implantable mechanical devices to improve human grasping in individuals with paralysis. OpenSim is an extensible and user-friendly software package built on decades of knowledge about computational modeling and simulation of biomechanical systems. OpenSim’s design enables computational scientists to create new state-of-the-art software tools and empowers others to use these tools in research and clinical applications. OpenSim supports a large and growing community of biomechanics and rehabilitation researchers, facilitating exchange of models and simulations for reproducing and extending discoveries. Overall, the software (OpenSim) can calculate variables that are difficult to measure experimentally, such as the forces generated by muscles and the stretch and recoil of tendons during movement. Moreover, OpenSim can predict novel movements from models of motor control, such as kinematic adaptations of human gait during loaded or inclined walking.

SCONE (<https://scone.software>) is open-source software for the predictive simulation of biological motion. It computes motion trajectories that perform a given task optimally, according to high-level objectives such as stability, energy efficiency and pain avoidance. Predictive simulations enable powerful new applications for musculoskeletal models, such as predicting the outcome of treatment and optimizing the efficiency and efficacy of assistive devices. It is a fully-featured software framework that allows researchers to perform, analyze and reproduce custom predictive simulations of biological motion.

With SCONE, users can:

- Design elaborate control strategies, using an easy-to-use custom configuration script (examples included).
- Optimize any set of model or control parameters, according to a user-defined objective. Out-of-the-box, SCONE supports different flavors of Covariance Matrix Adaptation (Hansen, 2006) for optimization.
- Use any existing OpenSim model [83] as a basis for predictive simulation.
- Add support for any third-party dynamic simulation software package, by implementing a thin API layer in C++.

- Efficiently develop, optimize, and analyze predictive simulations using the SCONE user interface.

3.1.2 Simulation and optimization module

The predictive forward dynamics simulation module relies on a musculoskeletal model. The musculoskeletal model used for the predictive dynamic simulation is based on an adult, 1.8m height and 75.2kg weight, used to simulate lower limb gait. The musculoskeletal geometry uses a trunk and two three-segment legs (See Fig. 3.1 below for the musculoskeletal model) to represent the human body which is a muscle reflex model proposed by Hartmut Geyer and Hugh Herr [80]. The forward dynamics model of gait controller consists of 70 free optimization parameters, 16 joint offset, four range thresholds and load thresholds for swing and stance, respectively[84]. The predictive optimization simulation process is shown in Fig. 3.1. The gait controller is implemented in SCONE, including leg states update, target features update and computation of the excitation signal (simulating the CNS), with output as $u(t - t_d)$. Musculoskeletal model is developed in OpenSim 3.3, including muscle activation dynamics, muscle contraction dynamics and joint moments update, and forward simulation is implemented using CMA-ES to optimize the joint angle, angle velocity and torque of each joint, while parameters such as hip, knee, ankle and head stability and gait speed range from the measurement feedback are fed into the gait controller which formed a closed-loop control model.

We use OpenSim3.3 to implement the development and parameterization for the musculoskeletal model. Then the modified model is optimized for the forward dynamics using SCONE. The exoskeleton robot depends on the kinematic and kinetic model of the 2-link humanoid model [11].

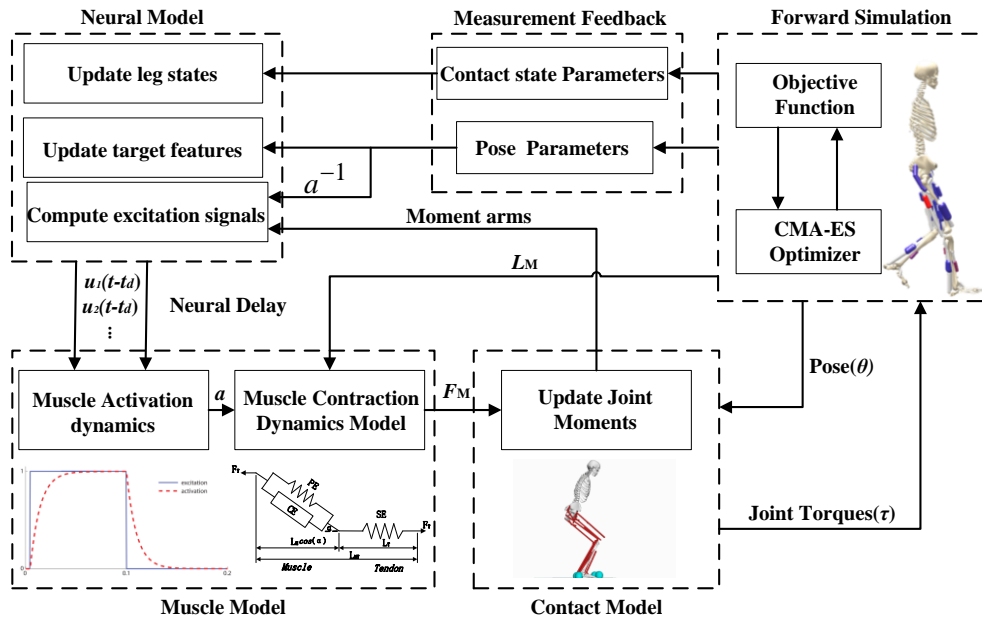


Figure 3.1 Predictive forward module for dynamic optimization. Relationship between gait controller, musculoskeletal model, measurement feedback, and forward simulation. We implement the musculoskeletal model in OpenSim3.3 and use SCONE for the forward prediction simulation.

3.1.3 Musculoskeletal model

The musculoskeletal model used for the predictive dynamic simulation is based on an adult, 1.8m height and 75.2kg weight, used to simulate lower limb gait. The musculoskeletal geometry uses a trunk and two three-segment legs to represent the human body which is a muscle reflex model proposed by Hartmut Geyer and Hugh Herr [80]. This simulation model has been cited in close to 700 pieces of literature. The results of these studies proved that it is reliable. Therefore, this article will be based on this musculoskeletal model for subsequent modeling. Considering the peak isometric forces, the muscle groups with similar functions in the lower limbs were combined into one MTU, so we obtained 9 MTU representing each leg: gluteus maximus (GMAX), biarticular hamstrings (HAMS), iliopsoas (ILPSO), rectus femoris (RF), vastus (VAS), biceps femoris short head (BFSH), gastrocnemius (GAS), soleus (SOL), and tibialis anterior (TA)[85][86][87] (See Fig. 3.2). The tendon slack length for each MTU was calculated using experimental data [87]. A compliant contact model was used to generate forces between the spheres at the heel and toes of the feet and the ground plane. Previous studies in [88][89] found that representing muscle paths as a single line tends to overestimate length changes, so we set the maximum muscle fiber contraction velocity to 15 optimal fiber lengths per second (l_0^m/s). The tendons are modeled as nonlinear springs that generate torque when the joint is hyper-flexed or hyperextended. Ligaments generate torque when the hip is flexed over 120° or extended over 30° , the knee is flexed over 140° or extended over 0° , the ankle is dorsiflexed over 20° or plantarflexed over 40° [3].

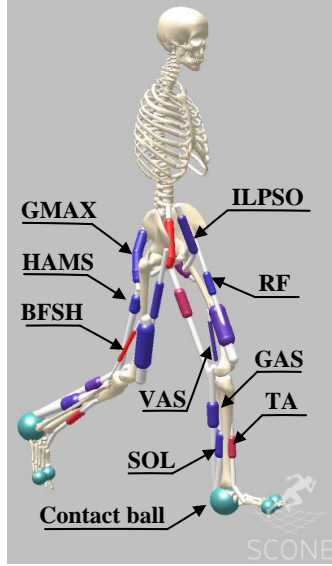


Figure 3.2 The planar musculoskeletal model of gait.

We employ the Hill-type model [43] with three elements in each MTU model: contractile element (CE), parallel-elastic element (PE), and serial-elastic element (SE) (see Fig. 3.3). The following relations hold true for our model:

$$F_{MT} = F_T = (F_{CE} + F_{PE})\cos\theta, \quad (3.1)$$

$$F_T = F_M^0 \cdot k_T(L_{MT} - L_M\cos\theta - L_{ST}), \quad (3.2)$$

$$F_M = F_{CE} + F_{PE}, \quad (3.3)$$

$$F_{CE} = F_M^o \cdot a \cdot f_l(L_M) \cdot f_v(\dot{L}_M), \quad (3.4)$$

$$F_{PE} = f_{PE}(L_M) = F_M^o \cdot M_0 \cdot (e^{\varepsilon_M} - 1), \quad (3.5)$$

$$a_{t+1} = 100h(u_t - a_t) + a_t, \quad (3.6)$$

Where F_{MT} , F_T and F_M are complete musculotendinous actuator, tendon force and muscle force, respectively. L_{MT} , L_M , L_{ST} are the complete length of the model unit, muscle length and tendon slack length. F_M^o is the maximum isometric force. $M_0 = 0.10377$, from the literature [90], ε_M is the passive muscle strain at F_M^o . Muscle excitation, u , represents the neural signals from the central nervous system and is a value between 0 and 1, representing the discharge rate of neurons. The excitation-activation model dynamic is represented by the first-order delay of equation (3.6), where h is the step-size (1/2400 s) [91] and a_t and u_t are the muscle activation and excitation dynamics.

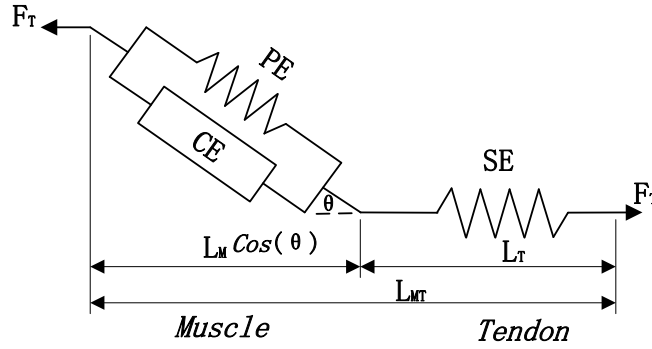


Figure 3.3 The architecture of the adopted Hill-type muscle-tendon actuator model. PE is the passive elastic element, CE is the muscle contractile element, and SE is the serial-elastic element that represents the tendon. F_T is the complete musculotendinous actuator. L_{MT} , L_M , are the complete length of the model unit and muscle length.

The model used the time delay (t_d) parameters of [92]. For all positive feedback and PD control laws, the initial time delay parameters are 5ms for hip, 10ms for knee, 20ms for ankle, respectively. For F- law acting on the soleus (SOL), the time delay parameter is 40ms. Muscle activation, a , and muscle excitation are represented by the differential equation (3.4), where h is the step size (1/2400 s), a_t and u_t denote the muscle activation and excitation values at the t -th timestep. The relationship between muscle force-muscle fiber length, $f_l(L_M)$, and muscle force-muscle fiber length velocity, $f_v(\dot{L}_M)$, is based on the relevant conclusion of [12][93] (see Fig. 3.4). The x-axis is L_{CE}/L_M^{opt} and V_{CE}/V_{max} respectively, L_M^{opt} is the optimal fiber length parameters.

The force generating capacity of a muscle is dependent on the length of muscle fibers (force-length relationship) and the velocity of muscle fibers (force-velocity relationship). The force-length curve shows that muscles can generate force more efficiently near L_{opt} , and the force-velocity curve shows that muscles lose ability to generate force as the magnitude of contraction velocity increases. In other words, the muscles are suitable for low speed situations and produce strong muscle forces.

The gait cycle is divided into five states, forming five transitions (see Fig. 3.5), and the total lower limb joint moment in the sagittal plane for each state is obtained by summing the

contributions of all relevant muscles for each state. Taking the mid-stance phase as an example, the joint moments for each joint are:

$$\tau_{hip} = \tau_{GMAX} + \tau_{HAMS}^{hip} - \tau_{ILPSO}, \quad (3.7)$$

$$\tau_{knee} = \tau_{VAS} - \tau_{HAMS}^{knee} - \tau_{GAS}^{knee}, \quad (3.8)$$

$$\tau_{ankle} = \tau_{SOL} - \tau_{TA} - \tau_{GAS}^{ankle}, \quad (3.9)$$

where the moment that makes the joint angle larger is positive. HAMS and GAS are biarticular muscles. Muscles of the legs include Slow-twitch fibers and fast-twitch fibers. Among them, slow-twitch muscles use energy slowly and fairly evenly to make it last a long time. This helps them contract for a long time, without running out of power. Fast-twitch fibers use up a lot of energy very quickly, then get tired and need a break. On average, people have about 50% slow-twitch and 50% fast-twitch fibers in most of the muscles used for movement. The slow-twitch ratios of the 12 muscle models of the lower limbs are determined according to the literature [3]. Slow-twitch ratios are used in the *measurement files* as the feedback ratios.

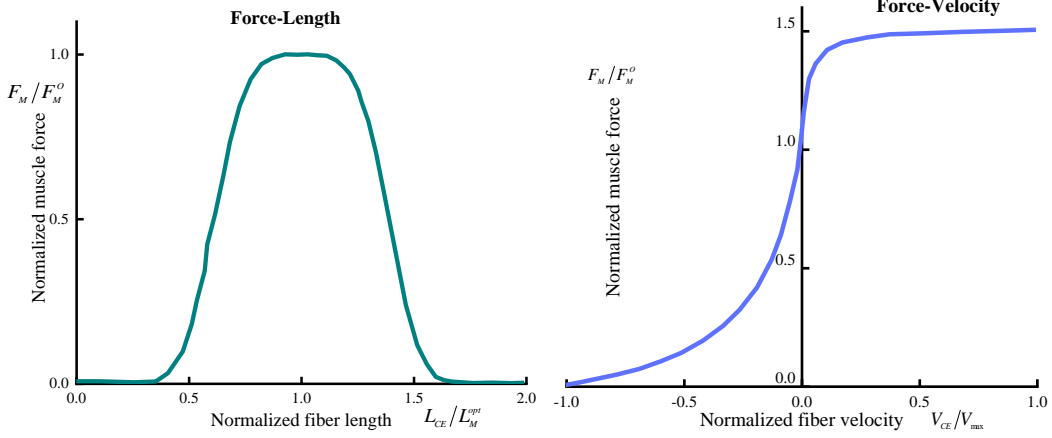


Figure 3.4 Muscle force-length, $f_l(L_M)$, and force-velocity, $f_v(\dot{L}_M)$, curve used in model.

OpenSim is a dynamic simulation software used to build and analyze locomotion [4]. The software generates muscle-driven simulations of object motion by the following steps: input the dynamic musculoskeletal model, the experimental kinematics, and the experimental reaction forces and moments obtained from the subject. Among them, the dynamic musculoskeletal model is actuated using the Hill-type model. Ong, Carmichael F. et al [5] used OpenSim to model a normal human: they collected kinematic and force feedback data from the subject and implemented the modeling through the following steps:

- a. Experimental kinematics is used to scale the musculoskeletal model to match the dimensions of the object.
- b. Solving the inverse kinematics (IK) problem to find the model joint angles that best reproduce the experimental kinematics.
- c. A residual reduction algorithm (RRA) is used to refine the model kinematics to be more dynamically consistent with the experimental reaction forces and moments.
- d. A computational muscle control (CMC) algorithm is used to find a set of muscle excitations

that will generate forward dynamic simulations that closely track the object's motion. From this, slow-twitch ratios were determined for 12 muscle models of the lower limbs, as shown in Table 3.1.

Table 3.1 Slow-twitch ratio of various muscles in the Hill-type activation model.

No.	Muscle	Slow-twitch ratio
1	hamstrings	0.499
2	bifemsh	0.529
3	glut_max	0.55
4	iliopsoas	0.5
5	rect_fem	0.387
6	vasti	0.484
7	gastroc	0.546
8	soleus	0.759
9	tib_ant	0.721
10	ercspn	0.6
11	intobl	0.56
12	extobl	0.58

Peak isometric forces were based on a previous musculoskeletal model[94], whose muscle volumes were based on young, healthy subjects[95]. The tendon strain at peak isometric force was 4.9% [94] for all muscles except for the plantar-flexors, whose values were set to 10% [96].

Table 3.2 Muscle parameters for the unimpaired musculoskeletal model.

Muscle name	Maximum isometric force (F_M^o)* [N]	Optimal fiber length (L_M^{opt})[m]	Muscle passive parameters (k_T, ϵ_M)**	Maximum fiber contraction velocity [L_M/s]	Tendon slack length (L_{ST})[m]	Muscle path from [97] model
ILPSO	2697	0.117	(5, 0.6)	15	0.130	psoas
GMAX	3338	0.157	(5, 0.6)	15	0.048	gluteus maximus
RF	2192	0.076	(9, 1.0)	15	0.346	rectus femoris
HAMS	4105	0.069	(5, 0.8)	15	0.349	semimembranosus
VAS	9594	0.099	(9, 1.0)	15	0.102	vastus intermedius
BFSH	557	0.11	(5, 0.6)	15	0.117	biceps femoris short head
GAS	4691	0.051	(5, 0.6)	15	0.384	medial gastrocnemius
TA	2117	0.068	(5, 0.6)	15	0.238	tibialis anterior
SOL	7925	0.044	(5, 0.6)	15	0.244	soleus

*Maximum isometric force is based on a specific tension of $60 N/cm^2$.

** k_T is the exponential shape factor for the passive force-length curve. ϵ_M is the passive muscle strain at F_M^o [98].

The tendon slack length of each muscle was calculated based on experimental data [87]. We

set maximum muscle fiber contraction velocity to 15 optimal fiber lengths per second as used in the literature [96] because models that represent muscle paths as a single line tend to overestimate length changes [89]. All muscle-tendon parameters are based on [97] and summarized in Table 3.2.

3.1.4 Gait controller

Our control laws for the actuators are based on the muscle-reflex controller introduced by Geyer and Herr [80]. Gait forward dynamics are actuated by the high-level state machine and the low-level control laws. The high-level state machine consists of five states, early stance (ES), mid stance (MS), pre-swing (PS), swing (S), and landing preparation (LP) respectively. Five transitions are generated between the five states, where the transitions associated with landing and standing are determined by comparing the ground reaction force of the ipsilateral foot to the threshold. In contrast, the transitions related to swing are determined by comparing the horizontal distance of the ipsilateral foot from the pelvis to the threshold. The five transitions are ES to MS, where the horizontal distance between the ipsilateral foot and the pelvis is less than the threshold; PS to S, where the ground reaction force of the ipsilateral foot is below the threshold; S to LP, where the horizontal distance between the ipsilateral foot and the pelvis is greater than the threshold; LP to ES, the ground reaction force of the ipsilateral foot is greater than the threshold; MS to PS, which is not controlled by the free parameter, occurred when the contralateral leg entered the ES state [21,22]. These conditions help the model to accurately execute the corresponding control program modules in *GaitController.scene*.

The gait controller combines state machines and low-level control laws to determine the excitation, using the right leg as an example (see Fig. 3.2). The state machine has two states in stance: early stance (ES), mid stance (MS), and three states in swing: pre-swing (PS), swing (S), and landing preparation (LP). The transition for each state is determined by the activation of the low-level control law. The low-level control laws include signal constants, feedback based on muscle length, muscle velocity and muscle force, and PD control based on pelvic tilt angle. The positive and negative feedback is denoted by (+) and (-), respectively. All feedback laws based on muscle states acted upon the same muscle, except for a negative force feedback from the soleus to the tibialis anterior. The model's 18 skeletal-muscle-tendon actuators are gluteus maximus (GMAX), biarticular hamstrings (HAMS), iliopsoas (ILPSO), rectus femoris (RF), vastus (VAS), biceps femoris short head (BFSH), gastrocnemius (GAS), soleus (SOL), and tibialis anterior (TA) [85][86][87].

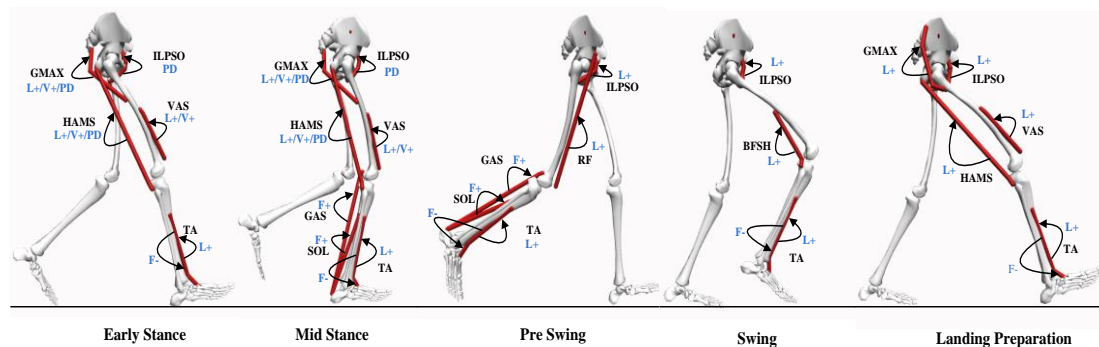


Figure 3.5 The gait controller combines state machines and low-level control laws to determine the excitation, using the right leg as an example.

In the low-level control laws, given the muscle-tendon model **MT**, the positive force feedback law, positive length feedback law, positive length velocity feedback law and Muscle-driven PD control law are defined as[3]

$$u_{F\pm} = \pm K_{F\pm} \tilde{F}_{MT}(t - t_d), \quad (3.10)$$

$$u_{L+} = \max(0, K_{L+} [\tilde{L}_M(t - t_d) - L_0]), \quad (3.11)$$

$$u_{V+} = \max(0, K_V [\tilde{\dot{L}}_M(t - t_d)]), \quad (3.12)$$

$$u_{PD} = K_P[\theta(t - t_d) - \theta_0] + K_V[\dot{\theta}(t - t_d)], \quad (3.13)$$

where $\tilde{F}_{MT}(t - t_d)$, $\tilde{L}_M(t - t_d)$ and $\tilde{\dot{L}}_M(t - t_d)$ are the *MT* model force normalized by F_{MT} , L_M and \dot{L}_M with a time-delay of t_d , respectively. K_P , K_V , θ , are proportional coefficients, differential coefficients and joint angles of the PD controller, respectively. PD controller is to ensure the stability of the controlled joint movement. Note that \tilde{F}_{MT} cannot increase indefinitely since the muscle's force generation capacity depends nonlinearly on the length and contraction velocity of the muscle fiber. As \tilde{F}_{MT} starts to decrease due to muscle physiology, $u_{F\pm}$ starts to decrease as well. The force feedback is the main source of activation to the GAS, TA, and SOL muscles during the stance phase (see Fig. 3.5).

As to the relationship between muscle activation and fiber length, we illustrate it with the GAS as an example. Fig. 3.6 shows the activation and fiber length of GAS during the gait cycle. Note the nonlinearity of the activation curve generated by the linear force feedback control law. While the foot is flat on the ground during mid-stance, GAS activation does not significantly change the fiber length, and force feedback leads to an activation build-up. As the heel loses contact during late-stance, the fiber rapidly shortens and reduces f_l and f_v (see Fig. 3.4). As the generated force decreases, the same force feedback leads to a drop-off in activation. We can see that positive feedback is generated during mid-stand (starting from 30% of the gait cycle) when muscle activation does not produce a significant change in muscle fiber length as the foot is on the ground. As the heel loses ground contact in late stance (starting from 50% of the gait cycle), the same muscle activation rapidly shortens the fiber length, which reduces force output and the activation through u_F^{GAS} .

The objective function, J , quantified high-level tasks of walking:

$$J = \omega_{cot} J_{cot} + \omega_{spd} J_{spd} + \omega_{head} J_{head}, \quad (3.14)$$

The goal is to minimize the gross cost of transport (J_{cot}) within the specified speed (J_{spd}), while ensuring head (J_{head}) stability. To balance the competitive objectives, the weights were manually adjusted to the following values[3]: $\omega_{cot} = 1kg/J$, $\omega_{spd} = 10000s^{-1}$, $\omega_{head} = 0.25s^3/m^2$. These weights determine the priority of the solution, that is, the contribution of the J_{head} term is greater than the contribution of J_{spd} , while ensuring that J_{cot} is minimal. The relevant procedures are defined in the *Measures.scone* file shown in Figure 3.7.

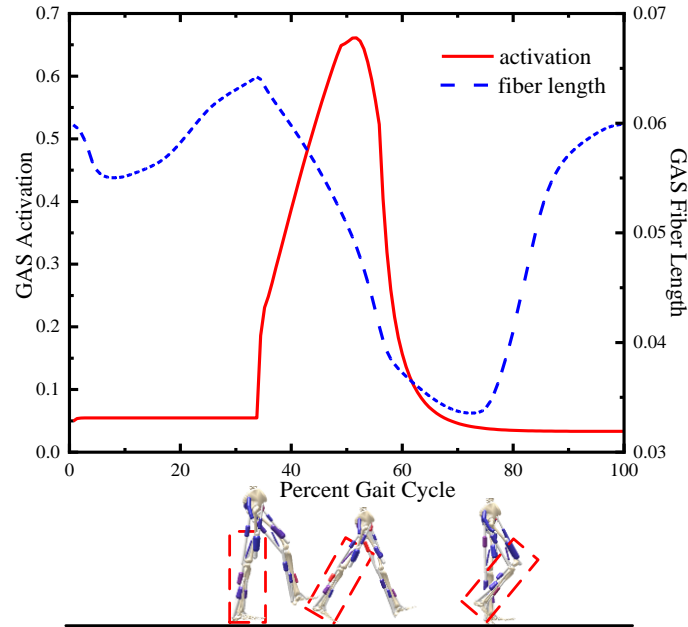


Figure 3.6 Effects of muscle physiology on activation illustrated by GAS activation and normalized fiber length in gait cycle.

In this article, we first particularly focus on the effect of BFSH on the gait posture during the gait cycle. As seen in Figure 3.5, the BFSH is mainly activated in swing state of the gait cycle. To implement the predictive simulation for healthy gait, the delay time (t_d) of BFSH is defined 10ms for gait controller initialization, and the relationship between the excitation (u) of the central nervous system and the activation (a) of the BFSH muscle model in gait cycle is shown in Figure 3.7. The model is represented by a first-order delay. The model used the time delay (t_d) parameters of [92]. For all positive feedback and PD control laws, the initial time delay parameters are 5ms for hip, 10ms for knee, 20ms for ankle, respectively. For F- law acting on the soleus (SOL), the time delay parameter is 40ms. In the initialization of this Figure, $t_d = 10ms$.

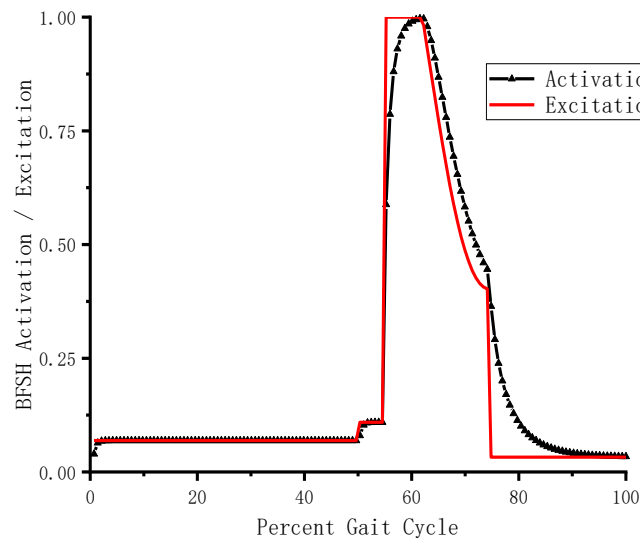


Figure 3.7 Activation dynamics of the BFSH model in healthy gait cycle transforms the neural excitation (u) into the muscle activation (a).

3.1.5. Generation of gait simulations

The predictive forward simulation module has three main data files: *Model.osim*, *InitialFile.par*, *Measures.scone* (see Fig. 2.2). The model files are the muscle-tendon geometry and the muscle-tendon actuated model, and the initialization files defined the initial values and thresholds of parameters. For instance, by changing the pelvis velocity along the x-axis direction, it is possible to have the model walk at different speeds. Hence, the model speed range can be changed in the *Measures.scone* file, which can be optimized based on the parameters, and the model can self-adjust the speed. The file *Model.osim* is modified in OpenSim 3.3, and all other components are called and executed in SCONE. *InitialFile.par* stored 90 free parameters, due to the CMA-ES of gait controller may take tens of hours to optimize the new model, hence, we perform pre-optimize before optimizing, and use the optimized parameters as the *InitialFile.par* for the new model, and the result show that it dramatically reduced the optimization scope and the optimization time.

The model files included gait controller file, the initialization files and the measures file, where the model files are the muscle-tendon geometry and the muscle-tendon actuated model, and the initialization files defined the initial values and thresholds of parameters (i.e., by changing the velocity of the pelvis along the x-axis direction, it is possible to realize the model walking at different speeds. Therefore, it is possible to change the speed range of the model in the *Measures.scone* file, which could be optimized according to the parameters, and the model can enable self-adjustment of the speed). The files required for each process of the predictive dynamic simulation module are shown in Figure 3.8.

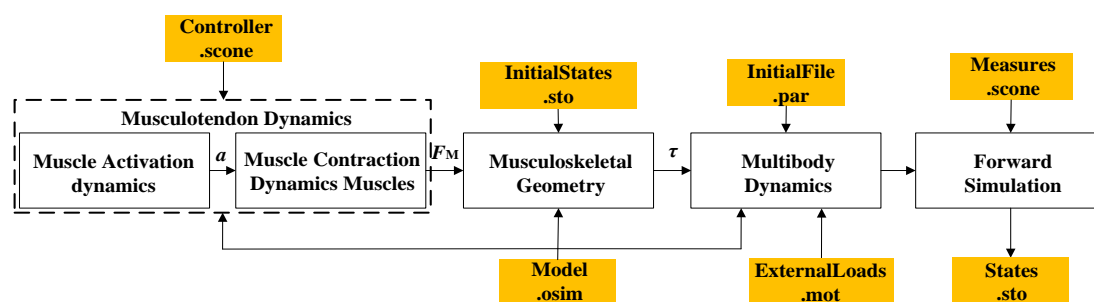


Figure 3.8 Flowchart illustrating the forward dynamics component in OpenSim and SCONE.

3.2 Experiment design

To explore the influence of the lower limb muscles on the knee joint during the gait cycle, we systematically and independently studied the relationship between the influence of each muscle group on the knee joint. Combined Figure 3.5 shows that the BFSH muscle mainly influences the knee joint flexion during the swing phase. Therefore, we first independently studied the influence of the BFSH muscle on the knee joint during the gait cycle, especially during the swing phase. Then, we systematically investigated the effects of HAMS, GAS and BFSH on the knee joint during the gait cycle and qualitatively gave the magnitude of the effects to provide a foundation for the subsequent development of modified rules for the predictive model. For subsequent modification of the model to achieve the reproduction of diseased gait according to the knee joint motion pattern in specific diseased gait.

3.2.1 Pathological knee gait caused by BFSH muscle contracture or muscle weakness

According to the forward predictive simulation module (Fig. 3.1), we proceed to analyze the BFSH muscle of the lower extremities in contracture and muscle weakness, respectively.

Following experimental observations, the sensitivity for the effect of BFSH contracture or muscle weakness on knee flexion was weaker for the former than the latter. In which, we modify the BFSH's optimal fiber length in *model.osim* (see Fig.3.8) to 85%, 70% and 55% of its original value when modeling the BFSH muscle contracture, and modify the BFSH's max-isometric force to 25%, 12.5% and 6.25% of its original value when modeling the BFSH muscle weakness, denoting mild, moderate, and severe, respectively [3].

3.2.2 The effects of muscle group synergy in gait cycle related to knee joint motion

The previous results gave us confidence in the forward predictive model. We then used the module to study how the HAMS, GAS and BFSH muscle groups act on the knee joint in gait cycles under contracture or muscle weakness. We modified the optimal fiber lengths of the HAMS, GAS, and BFSH muscles in the musculoskeletal model to 85%, 70%, and 55% of their original value, respectively, represented by mild, moderate, and severe degrees of contracture. Similarly, we modified the maximum isometric forces of these three muscle groups to 25%, 12.5%, and 6.25% of their original value, respectively, and expressed them as mild, moderate, and severe muscle weakness, respectively.

3.3 Validation

3.3.1 Validating the model's gait over a range of speeds

We validated our results within a defined range of walking speeds and self-selected speeds; this step was necessary because low gait speeds are commonly observed in patients with gait dysfunctions. We validated the ability of the predictive forward model and applied the optimization module to capture the walking trends at four different speeds: three prescribed speeds 0.6 m/s, 1 m/s and 1.4 m/s, and a self-selected speed. Individual comparisons of each speed with the experimental data of Schwartz et al [101] are (see Fig. 3.9). Their findings have been cited in close to 500 pieces of literature. And a large number of results have proved that the experimental results of Schwartz et al [101] are reliable. Therefore, this article will subsequently verify the results of our simulation module based on this experimental data. We provide all optimization results in the supplement "*Predictive optimization results.rar*". The simulated kinematic and kinetic adaptations, and joint angles matched the trends observed in the experimental data [101] [102].

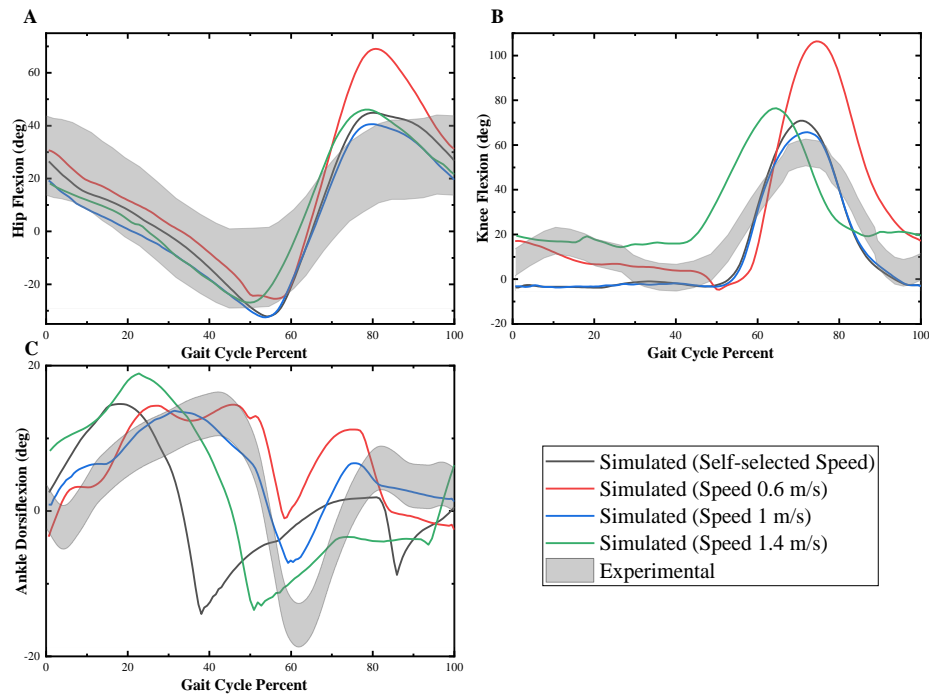


Figure 3.9 Validating the model’s gait over a range of speeds. Three prescribed speeds 0.6 m/s (red), 1 m/s (blue) and 1.4 m/s (green), and a self-selected speed (black) were analyzed. Joint angles for the hip (A), knee (B), and ankle (C) were plotted. Positive joint angles indicate flexion. Simulated kinematics and kinetics are compared with the experimental data (gray area) collected by Schwartz et al [101].

The optimized gait generated by walking at a constant speed of 0.6 m/s had significantly larger hip and knee angles in the late swing phase. At the prescribed speed of 1 m/s, the hip and knee angles were essentially the same as the self-selected speed in gait cycle, but in the pre-swing phase, the knee angles were smaller compared to the experimental data. With the prescribed speed of 1.4 m/s, the hip joint angle was out of range in the pre-swing phase and the knee joint entered flexion earlier, indicating that the optimized gait speed was increased.

Overall, the generated optimized gait for walking at a constant speed of 0.6 m/s exhibited greater angles at the hip, knee, and ankle joints than the other three speed patterns in gait cycle. The self-selected speed was the optimized gait generated by setting the initial speed in the range of (0.5-1.5 m/s). The trend for the self-selected gait was most similar to the prescribed speed of 1 m/s. In addition, the ankle joint of our model showed a significant early entry into dorsiflexion compared to the experimental data. However, this section mainly focuses on finding the impacts of HAMS, GAS and BFSH on the knee joint. Therefore, it has no influence on the subsequent study. This indicates that the magnitude of the prescribed speed is not necessarily related to the change of each joint angle in the optimized gait. The self-selected speed could find a solution to the optimization module and be insensitive to the initial guesses. So, we subsequently used self-selected speed to validate the relationship between HAMS, GAS and BFSH and the knee joint.

3.3.2 Walking with BFSH contracture or weakness in the swing phase

The results are illustrated in (Fig. 3.10), during walking, the BFSH muscle mainly inflicts the states of swing in the gait cycle. In the contracture condition (Fig. 3.10A), the knee joint angle

decreases approximately 20° to 25° during the swing phase, in which the contracture is severe, the knee joint exhibits hyperflexion throughout the gait cycle and behaves like rickets. It also leads to a significant reduction in walking speed. In muscle weakness (Fig. 3.10B), the knee joint angle decreases by approximately 10° during the swing phase. At all three severity of weakness, the knee joint shows significant muscle weakness, resulting in overstretching of the lower limb, which also leads to a significant reduction in model speed. In the case of severe contracture (Fig. 3.10C), the force on the knee joint is significantly increased except during the swing state, however, (Fig. 3.10D) demonstrates that muscle weakness has no effect on knee joint force, also indicating that the effect of BFSH on gait mainly during the swing phase.

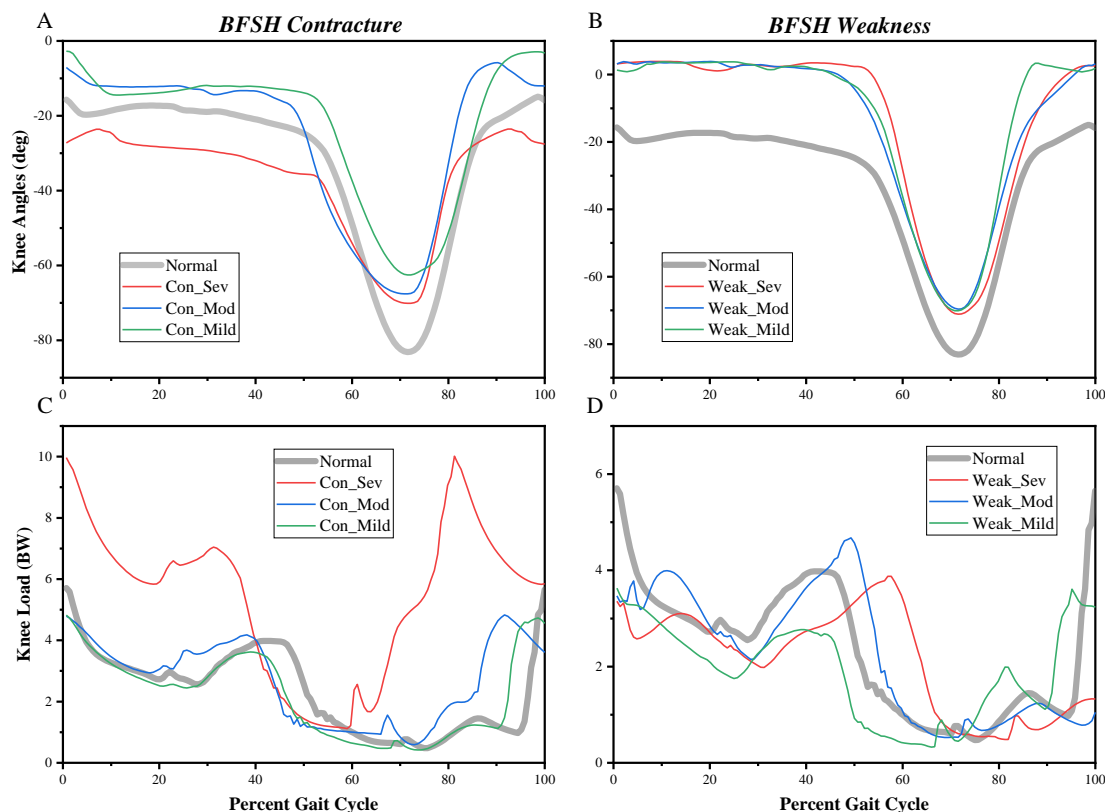


Figure 3.10 Predictive forward simulation of gait with BFSH contracture or weakness. Comparisons of knee angles in one gait cycle between the normal gait and three degrees of mild, moderate and severe of BFSH muscle contracture (A); Comparisons of knee angles with weakness (B); Comparisons of knee load with contracture (C); Comparisons of knee load with weakness (D). Joint load (BW), normalized by weight, denoted as $load = joint\ force / (model\ mass * g)$.

3.3.3 Validation for knee joint in gait cycle with muscle contracture or weakness

The previous results gave us confidence in the forward predictive model. We then used the module to study how the HAMS, GAS and BFSH muscle groups act on the knee joint in gait cycles under contracture or muscle weakness. We modified the optimal fiber lengths of the HAMS, GAS, and BFSH muscles in the musculoskeletal model to 85%, 70%, and 55% of their original value, respectively, represented by mild, moderate, and severe degrees of contracture. The left column (see Fig. 3.11) shows that when different degrees of contracture developed in HAMS (see Fig. 3.11a), GAS (see Fig. 3.11b) and BFSH (see Fig. 3.11c), the knee joint showed

hyperflexion during the contact phase with the ground, and the degree of sensitivity from strong to weak was GAS>BFSH>HAMS. Contractures of HAMS and GAS resulted in knee hyperflexion during the swing phase, but it was noted that when the HAMS contracture was severe, the knee flexion during the swing phase was instead significantly relieved. The more severe GAS contracture (see Fig. 3.11b), the more severe knee flexion. The moment simulation results indicate (see Figs. 3.11(d)-(f)) that all three muscle contractures cause the knee torque to increase, and as the contracture becomes more severe, the knee torque becomes greater.

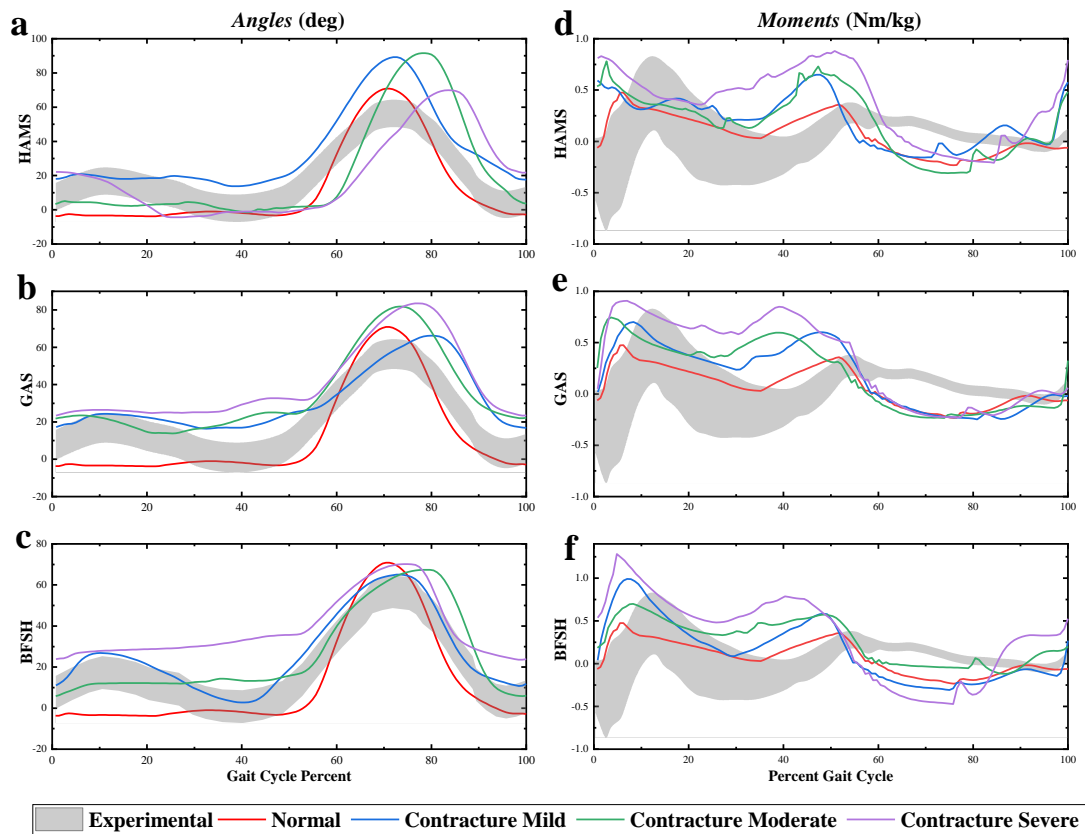


Figure 3.11 Validation for knee joint in gait cycle with muscle contracture. Knee kinematics and kinetics with normal (red), mild (blue), moderate (green) and severe (purple) contractures in HAMS, GAS and BFSH, respectively, are compared with the experimental data (gray area) collected by Schwartz et al [101]. The gait for knee angles (left column) and knee moments (right column) are plotted with different severities of muscle contractures.

Similarly, we modified the maximum isometric forces of these three muscle groups to 25%, 12.5%, and 6.25% of their original value, respectively, and expressed them as mild, moderate, and severe muscle weakness, respectively. Muscle weakness in the GAS (see Fig. 3.12b) and BFSH (see Fig. 3.12c) muscle groups had little effect on knee flexion, but mild muscle weakness in the HAMS (see Fig. 3.12a) had an accelerating effect on walking speed, while moderate and severe HAMS muscle weakness hindered walking speed instead. The effect of muscle weakness in BFSH is more sensitive to the knee moment (see Fig. 3.12f): the more severe the muscle weakness of BFSH, the weaker the knee moment in the whole gait cycle.

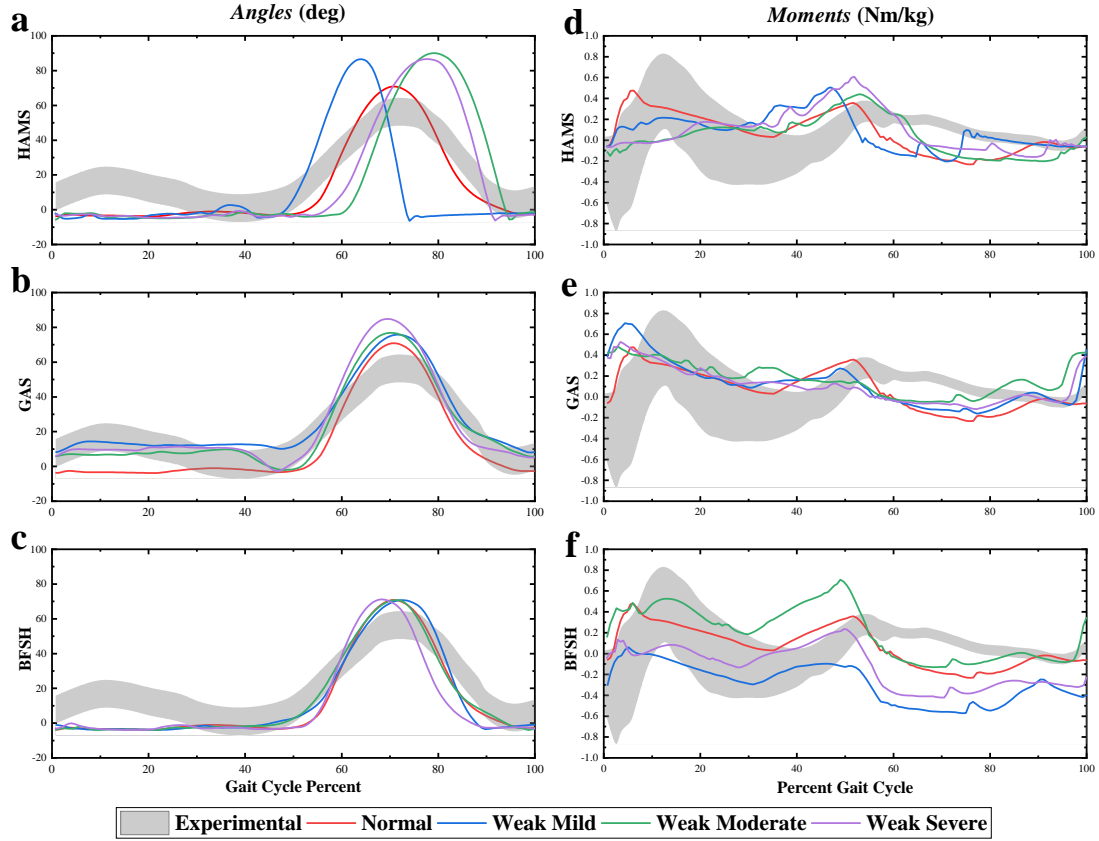


Figure 3.12 Validation for knee joint in gait cycle with muscle weakness. Knee kinematics and kinetics with normal (red), mild (blue), moderate (green) and severe (purple) weakness in HAMS, GAS and BFSH, respectively, are compared with the experimental data (gray area) collected by Schwartz et al [101]. The gait for knee angles (left side) and knee moments (right side) are plotted with different severities muscle weakness.

3.4 Experimental validation of muscle activation

We performed measurements of the lower limb BFSH muscle using DTing XS01 type electromyographic (EMG) sensor. The experimenter was 1.72 in height and 82 kg in weight, and after fixing the sensor (Fig. 5A), walking in the most comfortable state and implementing the acquisition of measurement data. EMG sensor used DTing XS01 type, a dry electrode biosensor. The sampling frequency was 1000HZ, the signal-to-noise ratio was 59.5dB, the sampling accuracy was 12Bit, the amplification was 700 times. The EMG sensor communicated with the handheld device via Bluetooth in real-time to record and generated image information. DTing XS01 is easy to measure but not easily fixed to the skin. Therefore, we fix the sensor with nylon straps and tape to avoid relative displacement to the skin. The experiment was performed in continuous walking, with 5 complete gait cycles as a group, resting for 30s after each group, and after 10 groups were performed, the EMG_DATA were collated and the group with high repeatability was taken (Fig. 5C). To obtain the EMG signal with offset, the EMG_DATA is subject to data conversion according to

$$U_{EMG} = D_{EMG} * (1.151 * 10^{-5}), \quad (3.15)$$

where U_{EMG} denote the voltage of the actual EMG signal, D_{EMG} denote the EMG ordinate data, thus, the range of EMG voltage in (Fig. 3.13C) is -5.89 mv to 5.89 mv . Based on the predictive forward simulation module of the lower limb BFSH muscle (Fig. 3.10), the black line is the simulated muscle activation, the red line is the simulated muscle excitation in gait cycle and the blue area is the measured EMG normalized data (Fig. 3.13B). Because the SEMG sensor is attached to the skin surface, it is easy to be disturbed during the experiment, which leads to some experimental data being unreliable. Therefore, we selected a set of data with the highest repeatability among the 10 sets of data, normalized them and take the average (see Fig 3.13B). The experimental results showed that subjects detected significant EMG signals during the swing phase (average range of 50%-80% of the gait cycle). It matched with the Predictive Forward Simulation for BFSH excitation-activation.

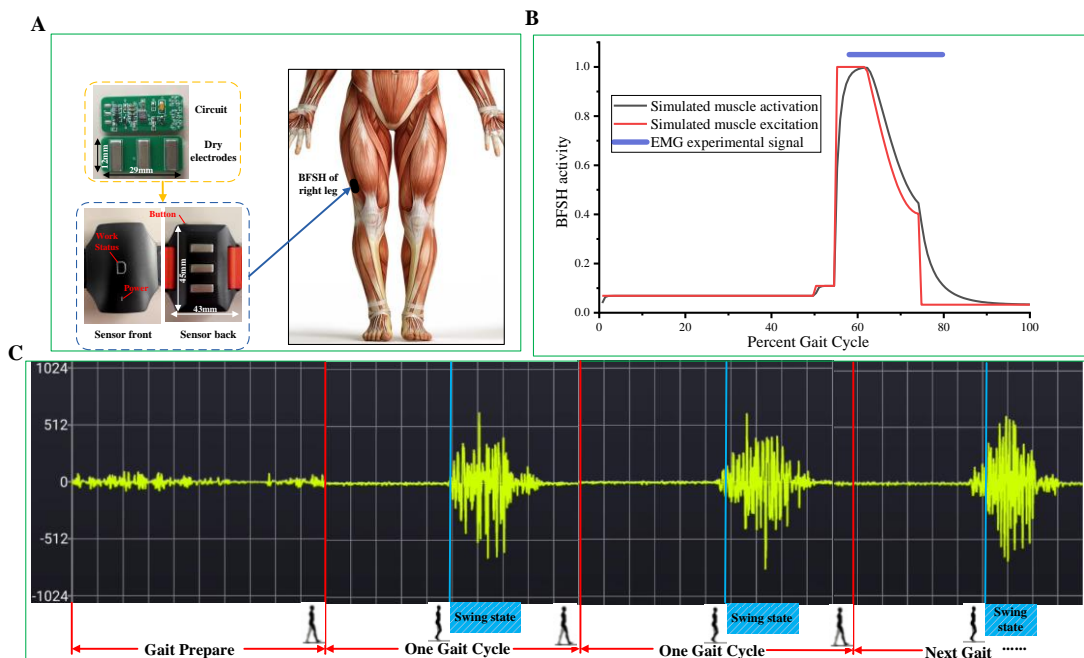


Figure 3.13 Experimental validation scheme for BFSH excitation-activation. (A) EMG sensor and its placement. (B) Predictive simulation module for excitation and activation, and normalized EMG acquisition data were averaged from the group with the highest repeatability. (C) EMG data acquisition at BFSH in continuous gait cycles. Muscle activation was recorded starting from >170 , and thresholds at signal intervals of -512 to 512 were considered as muscle activation until sustained inactivation.

In the gait cycle, muscle actuators are directly reflected by muscle activation on its surface[103]. Therefore, we collected experimental data on muscle activation in the HAMS, GAS and BFSH muscle groups of the normal human right leg in gait cycle.

Considering that the intensity of muscle activation increases with exercise time, the surface EMG signal is enhanced. To validate the predictive assessment model for excitation-activation of knee motion during gait cycle, we performed the excitation-activation experiments of HAMS, GAS and BFSH during the gait cycle according to the experimental approach in Fig. 3.13. Therefore, we intercepted the EMG signals of these three muscle groups in the latter part of the experiment for analysis, for it was found that the cycle changes of EMG signals were relatively

stable in the latter part of the experiment. We then used the muscle on-off time to indicate the muscle activation, and compared the binarized EMG signals with simulated muscle activation (normal gait, self-selected speed) (see Fig. 3.14).

The simulated muscle activity presented many of the significant features observed in the experiments. During early stance and landing preparation, it was the increase in body weight that made the HAMS very active. In mid-stance, when the knee joint needs to be driven to start flexion, the GAS behaves quite actively. While the swinging phase, the BFSH was active, allowing maximum knee flexion. There were some differences between our simulated data and experimental EMG, in which the activity of HAMS and BFSH during landing preparation was lower than the experimental data. The activation sequence of the three muscle groups also ensured a continuous flexion-extension of the knee joint in gait cycle.

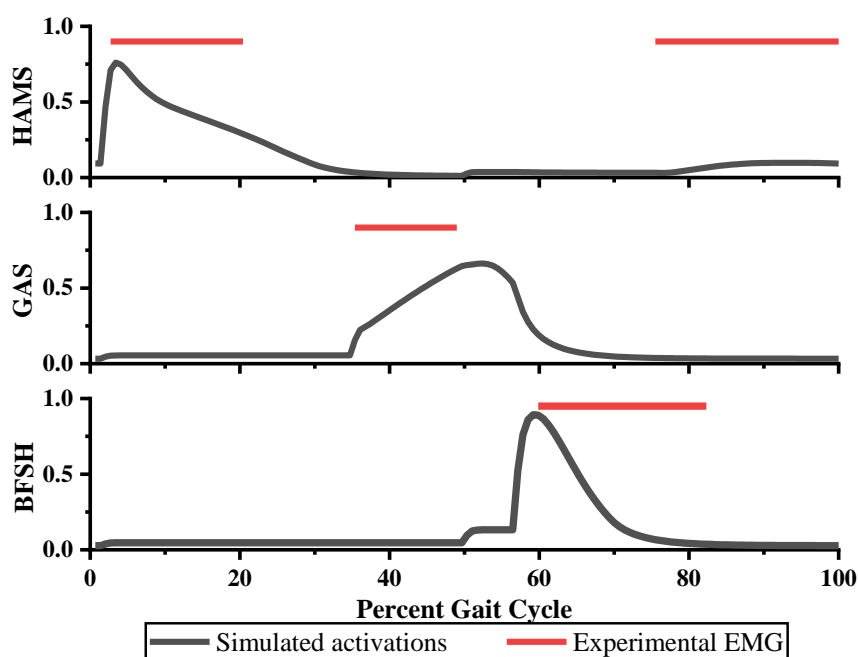


Figure 3.14 Muscle activation in normal gait at self-selected speed.

3.5 Discussion

On the basis of these results, we assessed the level of influence by HAMS, GAS and BFSH muscle groups on knee joints in gait cycle (see Table 3.3). (+) represents the enhancement effect, and (-) represents obstruction. The number indicates the intensity. The larger the number, the heavier the impact. The assessment reference value reflects the extent of impact by HAMS, GAS and BFSH muscle groups on knee joint in gait cycle.

The physical therapist is able to modify the MTU parameters in the predictive forward simulation module referencing Table 3.3. The contracture effect of the MTU actuators is obtained by modifying the optimal fiber length of the muscle model, similarly, the muscle weakness effect of the MTU actuators is obtained by modifying the maximum isometric force of the muscle model. It is experimentally demonstrated that each change in MTU parameters has a different effect on the optimization of knee gait. Our aim is to reproduce the gait simulation of the affected limb using the forward predictive simulation module in order to obtain real-time data on knee joint

angle and knee joint moment in gait cycle. The parameters modified by the physiotherapist are used as the desired values for the lower limb exoskeleton rehabilitation robot controller to realize the robot's spatial motion to track the movement of the affected limb offline. In addition, physiotherapists can adjust the damping and stiffness parameters offline through the patient's condition, so that the robot can not only quickly follow the affected limb trajectory, but also adjust the damping force and stiffness force to realize active rehabilitation training or passive rehabilitation training.

Table 3.3 The impact of contracture or weakness of muscle groups on knee joint in gait cycle.

Lower limb	Knee	Contracture						Weakness						
		ES	MS	PS	S	LP	Speed	ES	MS	PS	S	LP	Speed	
HAMS	Mild	Angle	3+	3+	3+	3+	3+	0	0	0	2+	2+	1-	2+
		Moment	2+	1+	3+	1-	0	0	1-	0	1+	2-	0	2+
	Mod	Angle	1+	1+	2-	3+	2+	1-	0	0	0	2+	2+	2-
		Moment	2+	1+	3+	2-	0	2-	2-	0	1+	1+	0	2-
	Sev	Angle	3+	0	0	3-	2+	2-	0	0	0	2+	2+	2-
		Moment	3+	1+	3+	1-	0	2-	2-	0	1+	1+	0	2-
GAS	Mild	Angle	3+	3+	3+	0	3+	2-	2+	2+	2+	1+	2+	0
		Moment	1+	2+	2+	2-	0	2-	2+	0	0	1-	0	0
	Mod	Angle	3+	2+	3+	2+	3+	0	2+	2+	0	1+	2+	0
		Moment	2+	3+	2+	2-	0	0	1+	0	0	1-	0	0
	Sev	Angle	3+	3+	3+	2+	3+	1-	2+	2+	0	2+	2+	0
		Moment	3+	3+	3+	2-	0	1-	1+	0	1-	1+	0	0
BFSH	Mild	Angle	3+	1+	1+	1-	2+	0	0	0	1+	0	1-	0
		Moment	3+	0	2+	2-	0	0	3-	3-	3-	3-	2-	0
	Mod	Angle	2+	2+	2+	0	1+	2-	0	0	1+	0	0	0
		Moment	2+	2+	2+	1-	0	2-	0	1+	2+	0	0	0
	Sev	Angle	3+	3+	3+	0	3+	1-	0	0	0	0	1-	1+
		Moment	3+	3+	3+	2-	2+	1-	2-	2-	1-	2-	2-	1+

+ represents the enhancement effect; - represents obstruction; the number indicates the intensity.

We have shown that the musculoskeletal assessment module for the lower extremities can successfully predict the simulation results of gait adaptation for the BFSH muscle without tracking experimental data. Predicted gait adaptation was verified to be basically accurate using the EMG sensors. Our work aimed to obtain simulation results of pathological gait adaptation due to different degrees of deficiencies in the BFSH muscle through the predictive assessment module. In addition, the module can calculate the relevant parameters for each joint of the optimized model. The control protocol of the LLER robot is optimized using the parameters to obtain a personalized passive training mode for the rehabilitation robot.

Relevant anatomical studies (Glenn et al.,1996 [38]) have shown that BFSH is damaged by dissecting 82 consecutive acutely injured knee samples. Based on this study, we performed the study on the effect of BFSH on knee motion. Related research on predictive simulation (Liu et al.,2008 [104]; Ong et al.,2019 [3]) investigate the effect of Soleus (SOL) and gastrocnemius (GAS) on walking with OpenSim and found the causes of "heel-walking" gait, "toe-walking" gait. We were inspired to study the role of BFSH on the knee joint in gait cycle. The results showed that when the BFSH is severely contracted, the knee joint exhibits hyperflexion (rickets) throughout the gait cycle. In addition, our result shows that BFSH muscle weakness had almost no effect on knee joint loading; BFSH affects the gait occurred mainly in the swing phase, which also verified that the predicted model was accurate.

It has been proposed in the literature [105] that heel contact on the ground and toe-off the ground are important for gait differentiation in gait planning for exoskeleton rehabilitation robots. However, the parameters of gait differentiation vary greatly from subject to subject. Our simulation model distinguishes the gait by the high-level state machine. In order to achieve the generality of the model, we do not consider heel-contact and toe-off, but only the ground reaction force generated when the heel landing is considered to determine the gait state.

Our findings on the kinematic and kinetic modeling of the lower extremity robot indicate that the trajectories tracked are comparable to previous results (Janz et al., 2017 [105]). In contrast to previous studies, the robotic system involved in this thesis requires harmonic self-service motors to drive the hip and knee joints, respectively, while there is no kinetic design for the ankle joint. However, previous studies (Ong et al., 2019 [3]; Armand et al., 2016 [6]) show that in addition to BFSH muscle, there are hams (biarticular muscle group) and gas (monoarticular muscle group), but the activities of the two muscle group on the knee joint not only accompanies almost the entire gait cycle, but also the isolation researches are complex. This is our main work in the next study.

3.6 Conclusion

This chapter complements the recent work by Carmichael [3], who achieved the prediction of gait adaptation by ankle-plantar flexor weakness and contracture. We proposed how to explore the effects of different muscle groups of the lower limb on the knee joint in gait cycles by means of predictive simulation. The final realization of clinical gait analysis using predictive forward dynamics is achieved. Parameters are provided for the implementation of customized training patterns in LLER devices.

Chapter 4. Motion Intent Detection Module Based on Multimodal Integration

In the process of rehabilitation training for stroke patients, the rehabilitation effect is positively affected by how much physical activity the patients take part in. Most of the signals used to measure the patients' participation are EMG signals or oxygen consumption, which increase the cost and the complexity of the robotic device[62]. To achieve an exoskeleton that provides intelligent, effective, and comfortable assistance to the wearer, it is essential to acquire different types of motion data from the human-exoskeleton system during movement. The measured motion data can be used to identify the wearer's movement intentions, analyze movement states and gait patterns, and evaluate motor performance.

Biomechanical data typically associated with human movement is divided into three types: kinematic data, such as body posture and joint angles; kinetic data such as human joint moments, ground reaction forces, and wearer-exoskeleton interaction forces; and bioelectrical data, such as electromyography (EMG) signals and electroencephalography (EEG) signals. Different types of sensors are usually equipped in the exoskeleton system to measure these motion data. For example, encoders, potentiometers and inertial measurement units (IMUs) are typically used to measure kinematic data, while torque transducers are used for kinematic data acquisition. With multiple sensor systems in hardware and sensor fusion algorithms in the software, exoskeleton controllers can acquire and process motion data for motion control purposes.

Frequently the feedback varies proportionally to the classified brain activity. Most of the BCI-task designed for movement restoration purposes are based on MI and movement execution (ME) [50]. These mental/behavioral activities produce specific spatiotemporal patterns of cortical oscillations denoted as event-related desynchronization (ERD), and event-related synchronization (ERS), mainly observed over sensorimotor areas, known as sensorimotor rhythm (SMR). MI produces sensorimotor rhythm (SMR) activation of brain regions and spectral performance. It means that simple MI of the movement to be performed by the user after a few days or weeks of training can induce SMR modulation in cortical areas that are directly connected to normal neuromuscular pathways[105]. To this end, MI is considered the best strategy for natural control of neuro-prostheses and BCI-based rehabilitation approaches. MI has been used in the ERD/ERS modality to control some of the most successful BCI systems, including the approaches of Wadsworth[106], Berlin[107], and Graz[108].

4.1 Overview of detection architecture

The multi-modal integrated intent detection module is mainly composed of the EEG system and the EMG system (see Fig. 4.1). Subjects were recorded by a 13-channel electrode system EEG system in the International 10-20 system after MI training for specific movements (such as knee flexion). Meanwhile, the three lower limb muscles (HAMS, GAS and BFSH) of the right leg were recorded using the EMG system within the same acquisition device.

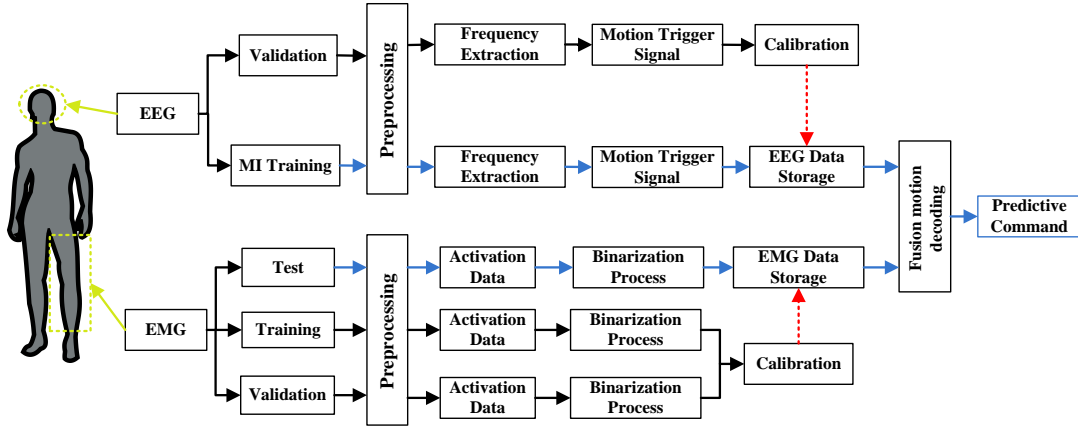


Figure 4. 1 Schematic representation of the motion intent detection system with multi-modal.

The EEG dataset is divided into two different datasets, namely the MI training set and the validation set. The data from the validation set is used to calibrate the parameters of the MI training classification. After pre-processing the EEG raw data, the required frequency signal is extracted and the trigger moment of the action signal is determined.

Muscle activation in three regions of the right leg is acquired with the DTing XS01 dry electrode EMG sensor. There are three types of datasets collected by EMG: test set, training set and validation set. The training data set is collected during the subject's repeated training (only wearing the EMG) for a particular movement. The same movement, trained several times, during this period the collected dataset is the validation dataset. The test data set is the EMG data set collected after the subject wears both EEG and EMG sensors. The EMG raw data are pre-processed to obtain muscle activation data for each muscle group. After binarizing these data, the control signal of the LLER robot from EMG is obtained.

The LLER robot control signals from the EEG and EMG are decoded by fusion motion and then used as predictive control commands to guide the LLER robot to achieve the active training stage in rehabilitation.

Passive training drives the lower limbs to perform movements, and after a period of focused training combined with the stimulation of HMI rehabilitation movement videos, patients are able to develop effective MI training. When the physiotherapist switched the rehabilitation mode of the LLER robot to active training mode, the patient is able to perform EEG control of the LLER robot as much as possible due to the long-term limb-to-cortex neural interaction activity experienced during passive training. In addition, the patient wears an EMG sensor system at the same time to correct the EEG to avoid false movements. We would like to emphasize that the active training mode focuses on arousing the patient's motor nervous system. Therefore, even if the multimodal integrated fusion module recognizes a low success rate of control intent, the physical therapist should provide psychological interventions to encourage the patient to complete active rehabilitation training.

For the assisted rehabilitation robot [109], the different actions of the HMI and the translation between them are shown in Fig. 4.2. We proposed the LLER robot during the active training mode, which is mainly implemented to complete the start and stop commands of the LLER robot using a

multimodal integrated intent detection module, such as a stand and sit commands. In addition, the patient is given the HMI rehabilitation training video corresponding to the training mode during the rehabilitation.

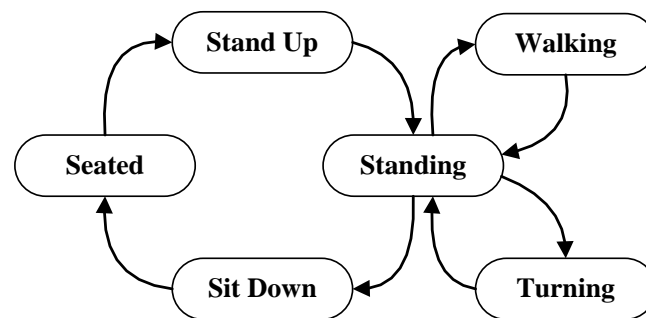


Figure 4. 2 HMI actions of the assisted LLER robot and their transformation.

Active training mode: On acquiring motion data, an exoskeleton's motion assistance can be initiated according to the wearer's intention. As the multi-modal integrated motion intent detection module is applied to the active rehabilitation training model, it has the following characteristics:

- a) Patients wear the EEG device during passive training, and the relationship between patients' psychological state and rehabilitation effect is studied quantitatively through EEG to provide guidance for patients' psychological training.
- b) Since patients with lower limb movement disorders caused by stroke and other diseases have the possibility of motor nerve reconstruction, monitoring the patients' EEG information during passive training to evaluate the rehabilitation effect of passive training.
- c) After patients pass a long period of passive rehabilitation training, combining with HMI's rehabilitation video movement stimulation helps patients to form effective MI training. When switching to active training mode, patients can form effective motor commands to control the LLER robot through the EEG and EMG multimodal fusion system.

4.2 Application advantages and characteristics of EEG sensors

Currently, the main research directions of BCI include brain neural mechanism revealing, experimental paradigm design, algorithm iteration and interactive application research. EEG-BCI systems are used as a direct connection system or electronic device between the human brain and computer, there are three main types of EEG features measured, which are based on Event-related Potentials (ERP) brain-machine interface, Steady-State Visual Evoked Potentials (SSVEP) brain-machine interface, and Motor-Imagine (MI) brain-machine interface[110].

ERP is used as a specific evoked potential that responds to a specific stimulus and generates a positive or negative deflection of voltage in the brain. One of the most-used components of such BCIs is the P300 potential[111].

SSVEP relies on a certain frequency of stimulation to produce a multiplicative response in the EEG signal, where the stimulus is mainly a fixed frequency flicker; while P300 is an EEG signal evoked due to a small probability event, where the small probability also emphasizes unpredictability and chance, and a positive peak in the EEG will appear 300ms after the stimulus,

so it is called P300 (P3) [112]. For example, the stimulus form that induces P300 looks like AAAAABAA, induced by that B. The stimulus form that evokes SSVEP is AAAAAAAA, evoked by that string of A. In addition, P300 is the response in the time domain and SSVEP is the characteristic in the frequency domain.

Due to the fact that human MI has similar brain activity to real action, MI can be considered as an imaginary mental activity without any obvious motor action. Since Jasper and Penfield [113] discovered the characteristic EEG for MI activation, more and more scholars have focused on MI-BCI-based control systems. Compared to SSVEP-BCI and ERP-BCI, which are evoked based on exogenous visual stimuli, MI-BCI depends on subjects' imaginary actions such as limb movements, whole-body activities, performing specific cognitive tasks, and relaxation, and does not require external stimuli (like visual stimuli).

The spontaneous EEG signals of imagined movements can be classified as output control signals, namely Event-Related Desynchronization (ERD)/ Event-Related Synchronization (ERS), which directly reflect the mental state associated with the subject's subjective movement and without any external triggering factors. Based on this relationship, the subject's brain actively controls the amplitude of the left and right μ and β rhythms to generate multiple control commands for interaction with external devices. Graz [114] conducted a study of the BCI system first based on the task of distinguishing 3 simple limb motor images (left hand, right hand and right foot). Compared to SSVEP-BCI and ERP-BCI systems, MI-BCI showed shorter response times and higher correctness rates in behavioral subjects, but individual differences among subjects were significant.

When subjects performed MI-BCI experiments, they might perform finger and arm pointing movements out of instinctive reactions. MI could cater to the subconscious reactions of subjects, which was simple and convenient to provide subjects with a high degree of freedom for control. Especially for people with motor disorders and motor rehabilitation, the MI-BCI system had incalculable research value[115].

According to whether there is feedback instruction, interface interaction can be divided into synchronous interaction and asynchronous interaction. Synchronous interaction specifically refers to the completion of an action and the need to get feedback before moving on to the next action. Asynchronous interaction refers to completing an action without getting feedback to proceed to the next action. Similarly, the BCI is divided into synchronous BCI and asynchronous BCI according to the temporal order of experimental operations[116].

The surface EEG is affected by mental activity and external stimuli and shows different frequency characteristics and spatial distribution. Based on the frequency, it can be divided into different frequency bands, as shown in Table 4.1. The five EEG frequency classifications are:

- δ waves are the largest and slowest waves in terms of amplitude. Delta waves may also be associated with pathological features such as subcortical lesions, diffuse lesions, deep midline lesions, and hydrocephalus in metabolic encephalopathy.
- θ waves appear during meditation or sleepiness [117] and are more frequent in young children. Theta wave abnormalities may indicate focal subcortical lesion disturbances.
- α waves are seen in the posterior region on both sides of the head, so they are also called

"posterior dominant rhythms", and their amplitude is more pronounced on the dominant side. Alpha waves appear when the eyes are closed and relaxed, and disappear or diminish when the eyes are opened or when the mind is focused.

- β waves represent positivity and anxiety and are often associated with locomotion. beta waves are small in amplitude, symmetrically distributed on both sides of the cortex and most obvious on the frontal side[60].
- γ waves tend to imply the joint activity of different neurons to accomplish some higher functions such as cognition or locomotion[118].

Table 4.1 EEG frequency classification.

Rhythm	Frequency (Hz)	Amplitude (μV)	Dominant period
α	8-13	10-100	Awake and relaxed
β	14-30	5-20	Thinking Activities
θ	4-7	20-100	Frequency of dominance during childhood. Also increases in adults during sleepiness.
δ	0.5-3	20-200	Deep sleep and Infant dominance frequency
γ	25-140	/	Body perception and cognition, such as working memory, and attention [119].

4.3 Signal extraction and processing

4.3.1 EEG signal detection and data processing

Before preprocessing the raw EEG signal for analysis, MATLAB, as well as the eeglab plugin, need to be installed. The aim of EEG data preprocessing is to improve the signal-to-noise ratio and consists of the following steps.

- Step 1: EEG raw signal acquisition. The EEG device used for our experiments is a 32-channel device with a sampling frequency of 1KHz. In this experiment, we adopted the data from the 13 EEG channels (see Fig.4.3B). The object is a normal male doing repetitive squat-stand-up movements (see Fig. 4.3A).
- Step 2: Import the EEG raw data into eeglab.
- Step 3: Verify the location of the channel. The position of the electrodes on the headshell can be changed by modifying the coordinate values of each electrode.
- Step 4: Reject useless electrodes. In this step, we only selected the electrode data for the 13 channels in Fig. 4.3B.
- Step 5: Re-reference. In this step, we select two electrodes T7 and T8 near the earlobe as reference electrodes.
- Step 6: Band-pass filtering. We choose the bandpass frequency interval (0.5-45Hz).
- Step 7: Run Independent Component Analysis (ICA).
- Step 8: Common average reference. For example, if the data acquisition for the CZ channel electrode fails during the experiment, the data from the CZ electrode can be replaced by averaging the data from multiple electrodes around the CZ in this step.
- Step 9: Detrend and data saving.

The flow chart of the preprocessing and decoding algorithm (see Fig. 4.4) is a multimodal integrated intent detection and processing module based on the above description, combined with the active training of the LLER robot. To measure brain waves in the parietal lobe, we use the Brain vision EEG device developed by Physio-Tech. The device consists of BrainCap with movable electrodes, the DC amplifier, and communication cables. Among them, the electrode cap is 32 channels, and we selected 13 of these channels. Figure 4.3 shows the EEG electrode montage corresponding to the international 10-20 system with 13 electrode positions used for decoding analysis.

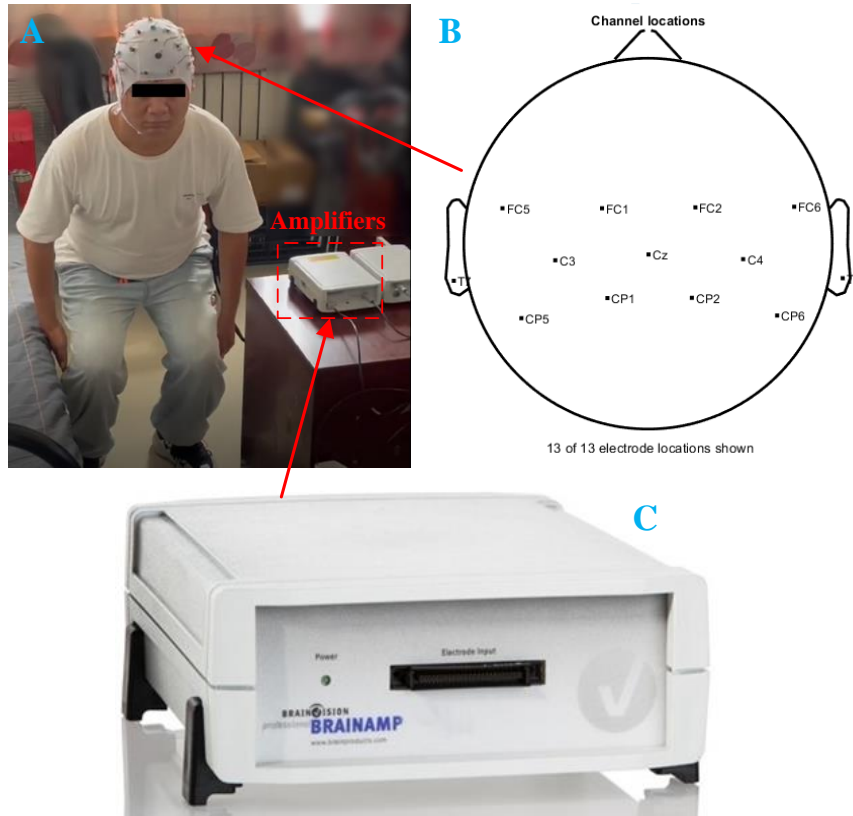


Figure 4. 3 EEG acquisition equipment and experimental environment. (A) is the subject wearing EEG to do squat-up movement, (B) is the 13-channel electrode distribution for the international 10-20 system, and (C) is the EEG host.

As preparation for neural decoding, recorded EEG signals were band-pass filtered in the delta band (0.5–4 Hz). The filtered non-rectified signals, which are called slow cortical potentials, were confirmed to be particularly informative for decoding motor-related parameters [120]. In the experimental data preprocessing, we band-pass filtered the raw data and retained the data from 0.5 to 45 Hz, so that the signals characterizing the motion have been preserved. To make it easier to implement active training of the LLER robot for intention recognition, we did a qualitative analysis of the EEG data collected from 13 channels, and the experimental results showed that the intention signals of squatting and getting up could be clearly distinguished.

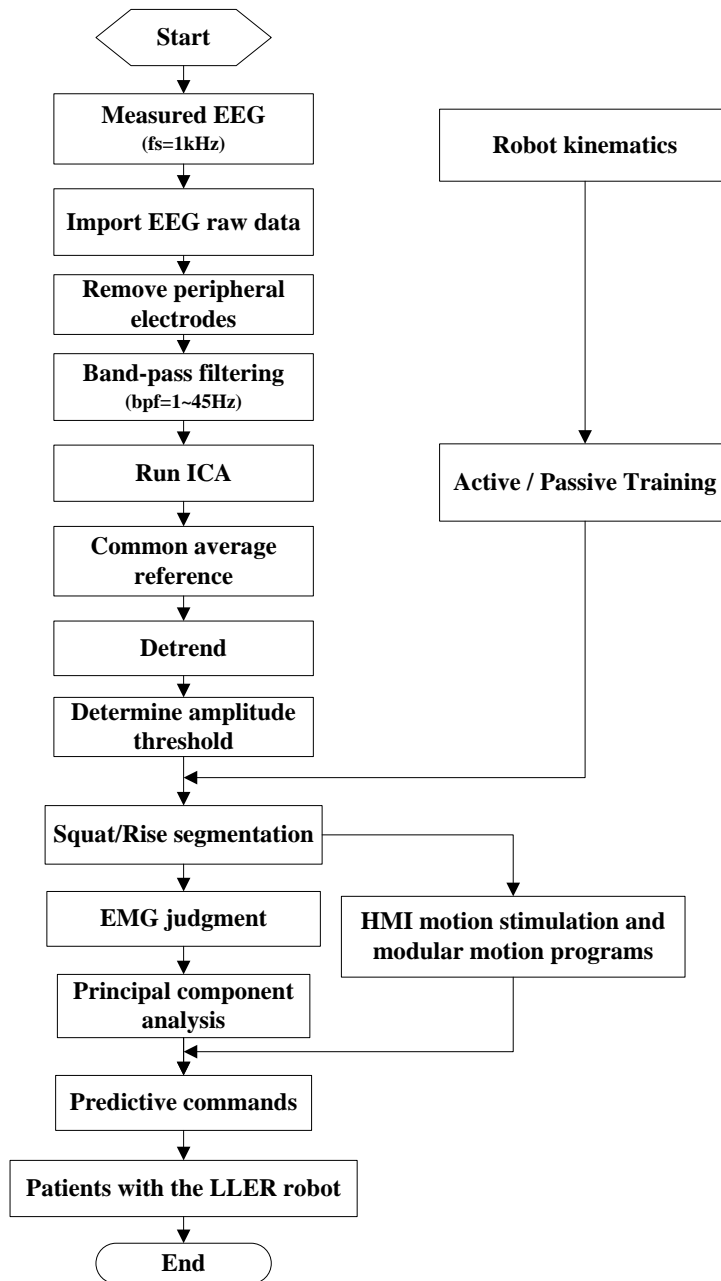


Figure 4. 4 Flowchart of the preprocessing and decoding algorithm.

4.3.2 EMG signal detection and data processing

The multi-modal integrated intent recognition module aims at patients with lower limb dyskinesia due to diseases such as stroke. The module encourages patients to give start-up commands to the LLER robot through MI. With each start-up, the LLER robot executes once a pre-defined motor command. By continuously stimulating the patient's motor nervous system, it achieves an improved rehabilitation effect. However, the signal acquired by EEG is weak and easily disturbed by the environment such as detection equipment, interference from electromyographic signals (such as eye EMG signals) and the patient's emotions. Therefore, in addition to preprocessing the EEG signal, the raw signal also needs additional means to ensure that the active training mode is established to give accurate motor commands. This module proposes the use of EMG sensors immobilized on the surface of muscles with residual muscle

force. The LLER robot can only start when both EEG start command and EMG muscle activation command are satisfied at the same time. In this way, not only the accuracy of active training is improved, but also the safety of rehabilitation training is ensured.

Assuming the BFSH muscle group of the affected limb has residual muscle strength, we measured BFSH's activation using a DTing XS01 EMG sensor. We implemented measurements of the lower limb BFSH muscle groups using DTing XS01 type EMG sensor. The subject was 1.72m in height and 82 kg in weight, and after fixing the sensor, walked in the most comfortable state and implemented the acquisition of measurement data. EMG sensor used DTing XS01 type, which was a dry electrode biosensor. The sampling frequency was 1000HZ, the signal-to-noise ratio was 59.5dB, the sampling accuracy was 12Bit, and the amplification was 700 times. DTing XS01 was easy to measure but not easily fixed to the skin. Therefore, we fixed the sensor with nylon straps and tape to avoid relative displacement to the skin (see Fig. 4.5B). The EMG sensor communicated with the handheld device via Bluetooth in real-time to record and generate image information. Subjects performed continuous up-squat movements, EMG data were collected after commissioning the device, and the first two up-squat cycles were recorded (see Fig. 4.5C). The EMG of the subject from the start of the squat to after fully rising is shown in Fig. 4.5A.

To obtain the EMG signal with offset, the EMG_DATA in (Fig. 4.5) is subject to data conversion according to equation 3.15. Preventing the EMG signal from being more strongly expressed because of the continuous excitation of the measured muscles due to the continuous exercise, the experiment tended to select the assay data at the beginning of the experiment.

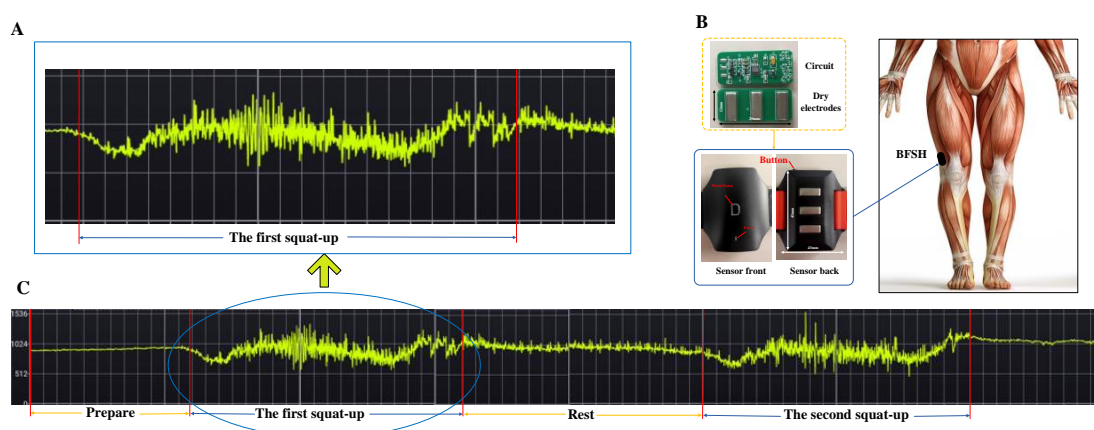


Figure 4. 5 Activation of BFSH in the right leg during rise-squat movement measured with EMG. (A) EMG in the first cycle, (B) EMG acquisition devices and measurement locations, and (C) EMG in the first two consecutive cycles.

4.4 Experiment and validation

4.4.1 Experimental design

It can be easily expected that the use of the sole EMG signal is enough to achieve accurate decoding of gait phases in conditions where the nervous and/or musculoskeletal systems are not impaired [121], with respect to what could be achieved by an EEG-based classifier, thanks to its higher correlation with the movement. However, in order to evaluate the control commands of the LLER robot using the available dataset (containing EEG and EMG of healthy subjects only), we

performed EEG experiments of squat-rise movements on normal subjects.

The subject wore an EEG device and did squat-up movements in cycles. Five sets of five squat-up cycles were performed, with about two minutes of rest between each set. We found that subjects began each set of experiments with more severe EEG signal interference, which we analyzed might be due to the psychological tension of the subjects at the beginning of the experiments. Therefore, after a systematic evaluation, we took the middle and latter part of the fourth set of experiments (18 s-40 s) and the sum of the EEG signals (0.5-45 Hz) of the 13 channels in the time domain is shown in Table 4.2.

Table 4.2 Action trigger time of the object in the experiment.

Action (s) Cycle	Prepare for squat	Full squat	Prepare to stand	Full stand up
1	2.2	5.7	6.5	9.1
2	10.5	14.2	14.7	18.2
3	20.2	23.4	24.1	27.2
4	30.1	33.5	34.2	36.2
5	42.2	44.7	45.6	48.2

The power spectral density of the 13 channels (see Fig. 4.7) indicates that the 5.9 Hz EEG signal is concentrated in the central and parietal regions of the cephalic shell. To be precise, this region contains EEG signals below 10 Hz. The result also verifies the finding of Hikaru et al.[56] that the activation of motor muscle synergy is decoded from slow cortical waves. The power spectral densities (see Fig. 4.7) also show that the signals of the 13 channels we selected are basically consistent with the squat-rise action. Therefore, we took the peak time of each channel to set the start command of LLER in active training mode.

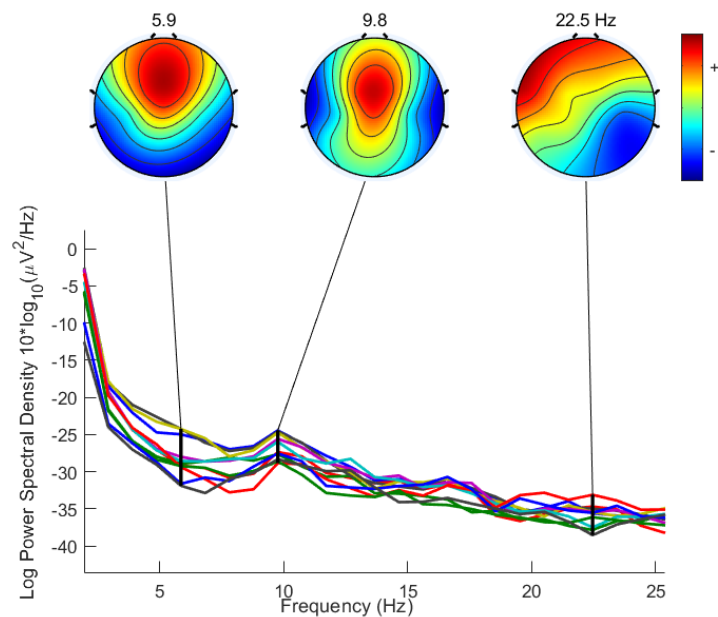


Figure 4. 6 Channel spectra and maps.

After pre-processing the raw EEG signal in Fig. 4.4, the data set of 13 channels (see Fig. 4.3B) was selected and the DC offset and normalize channels were performed again separately, and the results are shown in Fig. 4.8. Then the temperature clouds of the signal component distribution were plotted at the wave peaks for each of the 13 channels.

The ICA weights were applied to the EEG signals coming from Step I, projecting the data into the independent component domain. Components that belong to stereotypical artifacts (e.g., neck muscles, eye movement) were rejected by back projecting the EEG signals to the original domain using only the components related to brain activity.

The experimental data set of the fourth group (18s-38s) was processed using EEGLAB and the EEG clouds at the moments of 20.3s, 26.3s, 31.7s and 35.5s were plotted (see the bottom of Fig. 4.8). The results show that the data composition and distribution of each frequency band collected by the 13 electrodes at the EEG wave peak are basically consistent. In addition, we also collected EEG data at three random moments in the non-wave region, and its cloud distribution (see the top of Fig. 4.8) is quite different. These findings provide us the possibility to use patient intent to fulfill the active training of the LLER robot.

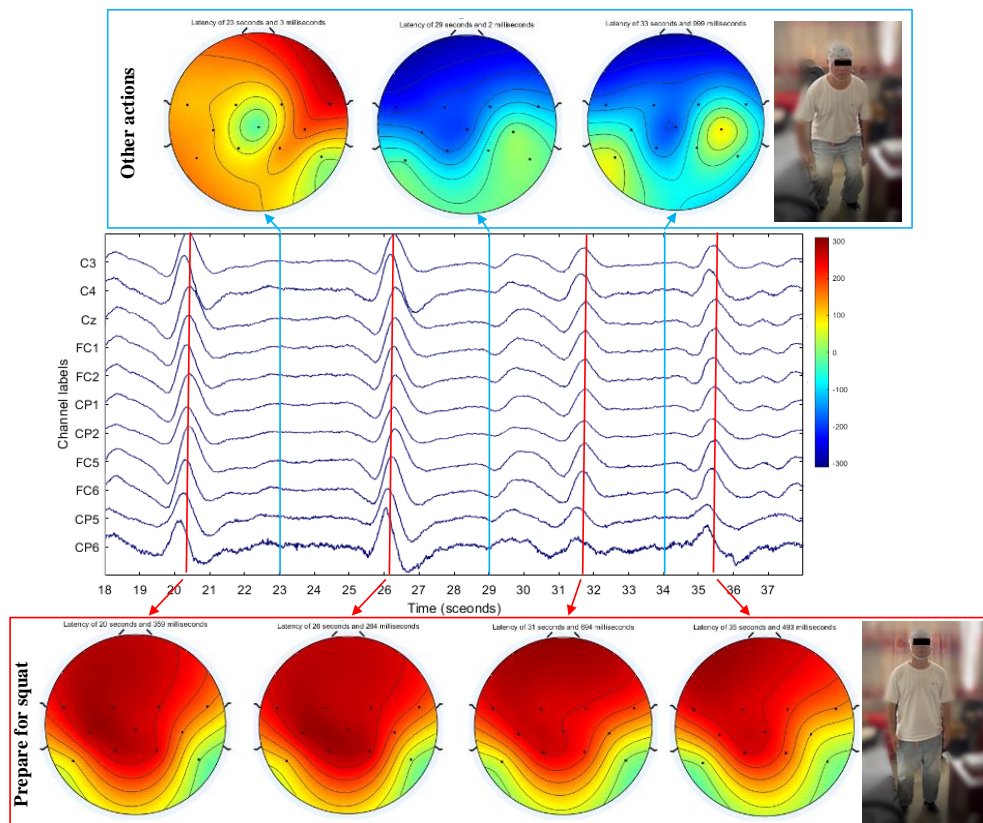


Figure 4. 7 13-channel EEG acquisition of time-domain data for squat-rise movements.

4.4.2 Experimental conclusions

After evaluating the experimental results, we took the fourth group of experimental results in which the subjects' emotions were relatively stable for analysis. The moments of pre-squat, full squat, pre-stand and full stand up were recorded separately for each movement cycle (see Table 4.2). Meanwhile, 13 channels of EEG data sets (18 s -38 s) were acquired. After processing by

EEGLAB, the wave peaks/several non-wave peaks of each channel were taken separately (see Fig. 4.6) and collated as shown in Table 4.3.

The fourth set of squat-rise movements performed by the subject (see Table 4.2) showed that one squat-rise cycle was approximately 7 s. The time interval between fully squatting and preparing to stand up is about 1 s. In the experiment, all actions of the subject were done completely autonomously according to the experimental requirements, so the time interval of each action state was different, which met the experimental design requirements of MI.

Combining Table 4.2 and Table 4.3, the bolded data in Table 4.2 basically correspond to the time of the prepared squat in Table 4.3, with a maximum error of 0.9 s. This result also illustrated that the subjects showed a significant enhancement of EEG signals in the central area of the cerebral cortex in preparing for squatting and fully standing, respectively, during the squat-rise movement. These findings provide us the possibility to implement the LLER robot in active training mode when the patient's intention can control the robot to perform rehabilitation operations. As shown in Table 4.3, the average amplitude value of the 13 channels is 2526.339 μV at the moment of the EEG wave peaks. The amplitude difference in the non-peak period is large, around the baseline (25 μV), which is much smaller than the amplitude of wave peaks. Therefore, in the subsequent LLER robot development, we will determine the threshold value for triggering based on the sensitivity of the MI.

Table 4.3 Waveform amplitude at each trigger moment during EEG measurement.

Time (ms) Channel labels	20359	26264	31694	35493	Average
C3	300.3401	282.5299	139.47	169.0924	297.1442
C4	172.8691	191.1732	88.75695	81.29569	178.0316
CZ	284.9825	278.8902	140.5478	187.032	297.1508
FC1	301.2987	276.0055	145.8306	189.9183	304.351
FC2	270.3384	260.1422	138.9694	159.1393	276.1964
CP1	295.5192	283.308	144.134	181.6365	301.5326
CP2	264.0945	265.0034	120.4776	136.9113	262.1623
FC5	272.0109	257.6534	139.639	183.9981	284.4338
FC6	171.1646	193.0882	111.1609	113.1349	196.1828
CP5	116.3512	117.4331	38.65043	28.4652	100.3
CP6	25.23418	36.90581	11.7547	12.66566	28.85345
Sum	2474.203	2442.133	1219.391	1443.289	2526.339

4.5 Conclusion

This chapter proposes a human intention detection module based on multi-modal integration of MI. The module is used in the active training mode in the middle and late stages of rehabilitation training. The EEG module based on MI acquires the patient's EEG signal, which is corrected by EMG to drive the LLER robot to perform a complete walking cycle. In addition, the accuracy of the MI is enhanced by combining the continuous stimulation of the patient's brain with the HMI rehabilitation visual instrumentation.

Chapter 5. LLER Robot Modeling and Controller Design

The human-robot system consists of an exoskeleton that works in concert with the human muscular and nervous systems[122]. The interaction between the exoskeleton and the human body determines whether the exoskeleton can perform the desired function. Researchers have tried to model HRI through musculoskeletal models. One attempt is to model the interaction between human and rehabilitation devices through musculoskeletal simulation, where parametric design based on musculoskeletal performance settings has been performed[123]. Exoskeleton design with biomechanical analysis has also been investigated on single-degree-of-freedom exoskeletons[124]. Human-robotic models have been developed for 2-degree-of-freedom assisted exoskeletons to study the effect of power assistance on muscle activity[125]. Therefore, the core problem in the modeling effort is to simulate: the response of the human body when subjected to external loads and forces/torques exerted by the exoskeleton. Our human-robot system consists of the predictive simulation module in Chapter 3 and the lower limb exoskeleton rehabilitation robot in this chapter.

5.1 Control strategies for gait rehabilitation

The control strategies of exoskeletons in gait rehabilitation can be generally divided into two main categories: (1) trajectory tracking and (2) assist as needed (AAN) [16]. In trajectory tracking control, the predefined trajectories of the lower limb joints, usually collected from normal gait, are used as the control objectives. The passive training in the pre-rehabilitation stage is mainly achieved with trajectory tracking. The active training in the middle and late stages is achieved through the AAN for this stage of rehabilitation training. A gravity-compensated PD controller is developed to achieve the requirements of LLER robot trajectory tracking. Robust adaptive controllers are developed to satisfy the LLER robot's resistance to external perturbations.

Based on the above research, considering the different damping and elasticity requirements of the LLER robot for different affected limbs and the same affected limb at different stages of rehabilitation training, we developed the impedance controller based on variable parameters to meet the different rehabilitation requirements with the help of physical therapists.

5.2 Mathematical Model Formulation of LLER Kinematic Analysis

In order to construct the human-exoskeleton model, two submodules, a musculoskeletal model and an exoskeletal model, need to be developed. The musculoskeletal model performs biomechanical analysis, and the exoskeletal model performs kinematic and kinetic simulations. The former is presented in Chapter 3.1.3. Therefore, this section focuses on simulating the kinematics and kinetics of the exoskeletal model.

Literature has suggested that physical guiding lower limb movement may decrease motor learning, and the patient's effort and participation in the training, and thus may not achieve effective training [126]. So far, trajectory tracking control has been used mainly for the early rehabilitation of patients with lower limb movement disorders when muscle strength is very weak [127]. Based on the wearer's intention, the exoskeleton can adjust the amount of support to be assisted. Therefore, the wearer will feel more comfortable when walking with the exoskeleton. With this controller, the exoskeleton can provide interactive robotic gait training, according to the wearer's disability level and voluntary participation. The lower limb exoskeleton rehabilitation

robot system is a complex nonlinear highly coupled dynamic system [128]. The model of the robot has three parts: robot kinematics model, dynamics model and variable parameter impedance controller.

Indeed, according to movement exerted on the lower limb is of small variation of acceleration during the rehabilitation sessions, some hypotheses were fixed, and which will be valid for all structures [27]:

- 1) The links of the exoskeleton robot are considered to be rigid bodies. This assumption enables the application of the mechanical rigid body approach. As the body segments are rigid, their center of mass and their moments of inertia does not change during movement.
- 2) The joints are assumed to be perfect mechanical connections.
- 3) The actions that generate movement are localized in the joint centers.
- 4) The body mass is assumed concentrated on the center of mass.
- 5) To ignore artifacts soft tissue, the movement marrow masses (skin and fat) is negligible and does not affect the inertial properties during the execution of the movement.
- 6) The joints are defined with viscoelastic behavior in anatomical axes of the joint. In addition, these axes are fixed, thus the translations of a bone on the other (knee) are also negligible.
- 7) The muscular action is due to a single muscle group. Therefore, there are no antagonist muscles that oppose the movement created by the agonists.

The LLER robot system is a complex nonlinear highly coupled dynamic system [128]. The model of the robot has three parts: robot kinematics model, kinetic model and variable parameter impedance controller.

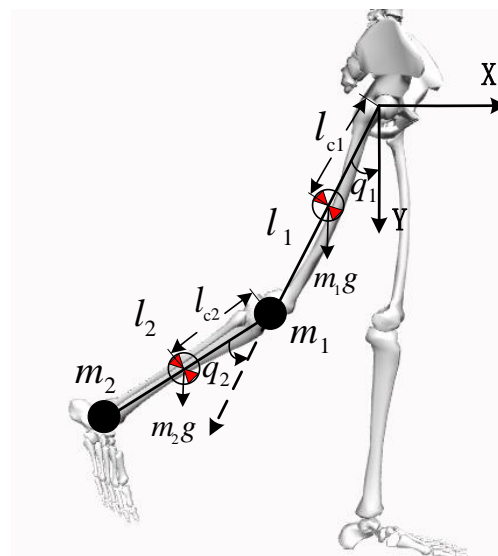


Figure 5.1 Two link model for dynamic analysis of lower limb exoskeleton robot. It includes link lengths (l_1, l_2), center of gravity for link lengths (l_{c1}, l_{c2}), the approximate mass of the lower limbs (m_1, m_2), the angles between the rotational point (q_1, q_2), counterclockwise negative.

Planar mechanical structure with two rotating joints (see Fig. 5.1). The notation is solved by: for $a = 1, 2$, q_i denotes the joint turning angle, which is also used as a generalized coordinate, m_i denotes the mass of link i , l_i denotes the length of link i , l_{c_i} denotes the distance between the previous joint and the center of mass of link i , and I_i denotes the rotational inertia of link i about the axis that passes through its center of mass and points out of the thesis. We use the Denavit-Hartenberg joint variables as generalized coordinates and thus are able to efficiently derive the Jacobi matrix expressions to calculate the kinetic energy as

$$\begin{cases} v_{c1} = J_{v_{c1}} \dot{q} \\ v_{c2} = J_{v_{c2}} \dot{q} \end{cases} \quad (5.1)$$

with

$$J_{v_{c1}} = \begin{bmatrix} -l_{c1} \sin q_1 & 0 \\ l_{c1} \cos q_1 & 0 \\ 0 & 0 \end{bmatrix}, \quad (5.2)$$

$$J_{v_{c2}} = \begin{bmatrix} -l_1 \sin q_1 - l_{c2} \sin(q_1 + q_2) & -l_{c2} \sin(q_1 + q_2) \\ l_1 \cos q_1 + l_{c2} \cos(q_1 + q_2) & l_{c2} \cos(q_1 + q_2) \\ 0 & 0 \end{bmatrix}. \quad (5.3)$$

Therefore, the kinetic energy corresponding to the translational part is

$$\frac{1}{2} m_1 v_{c1}^T v_{c1} + \frac{1}{2} m_2 v_{c2}^T v_{c2} = \frac{1}{2} \dot{q} (m_1 J_{v_{c1}}^T J_{v_{c1}} + m_2 J_{v_{c2}}^T J_{v_{c2}}) \dot{q}, \quad (5.4)$$

The angle velocity term, ω_i , are considered below. When expressed in the base inertial coordinate system, we have

$$\omega_1 = \dot{q}_1, \omega_2 = (\dot{q}_1 + \dot{q}_2) \quad (5.5)$$

Since ω_i is aligned with the z-axis of each joint coordinate system, the kinetic energy of the rotational motion can be expressed as

$$E = \frac{1}{2} I_i \omega_i^2 = \frac{1}{2} \dot{q}^T \left\{ I_1 \begin{bmatrix} 1 & 0 \\ 0 & 0 \end{bmatrix} + I_2 \begin{bmatrix} 1 & 1 \\ 1 & 1 \end{bmatrix} \right\} \dot{q}, \quad (5.6)$$

where I_i is the rotational inertia with its axis passing through the center of mass of the connecting rod i and parallel to the z_i axis. Construct the inertia matrix $D(q)$. To do this, we need to add two matrices to Eq. (5) and Eq. (8), respectively. Thus, the inertia matrix is

$$D(q) = m_1 J_{v_{c1}}^T J_{v_{c1}} + m_2 J_{v_{c2}}^T J_{v_{c2}} + \begin{bmatrix} I_1 + I_2 & I_2 \\ I_2 & I_2 \end{bmatrix}, \quad (5.7)$$

$$\begin{cases} \cos \alpha \cos \beta + \sin \alpha \sin \beta = \cos(\alpha - \beta) \\ \cos^2 \theta + \sin^2 \theta = 1 \end{cases}, \quad (5.8)$$

Equation 8 combined with the trigonometric constant Equation 9 is obtained as

$$D(q) = \begin{bmatrix} m_1 l_{c1}^2 + m_2 (l_1^2 + l_{c2}^2 + 2l_1 l_2 \cos q_2) + I_1 + I_2 & \\ m_2 (l_{c2}^2 + l_1 l_{c2} \cos q_2) + I_2 & \\ m_2 (l_{c2}^2 + l_1 l_{c2} \cos q_2) + I_2 & \\ m_2 l_{c2}^2 + I_2 & \end{bmatrix}, \quad (5.9)$$

Calculating the Christoffel signs, we get

$$C(q, \dot{q}) = \begin{bmatrix} -0.4\dot{q}_2 \sin q_2 & -0.4 \sin q_2 (\dot{q}_1 + \dot{q}_2) \\ 0.4\dot{q}_1 \sin q_2 & 0 \end{bmatrix}. \quad (5.10)$$

The gravity moment vector $g(q)$ is given by

$$g(q) = \begin{bmatrix} (m_1 + m_2)l_1 \cos q_2 + m_2 l_2 \cos (q_1 + q_2) \\ m_2 l_2 \cos (q_1 + q_2) \end{bmatrix}. \quad (5.11)$$

The dynamic equation of the LLER robot with 2-DOF is

$$\tau = D(q)\ddot{q} + C(q, \dot{q})\dot{q} + g(q) + F(\dot{q}) + \tau_d, \quad (5.12)$$

where $q \in \mathbb{R}^2$ is the angular displacement of the joint, $D(q) \in \mathbb{R}^{2 \times 2}$ is the inertia matrix of the robot, $C(q, \dot{q}) \in \mathbb{R}^2$ denotes the centrifugal and Coriolis forces, $g(q) \in \mathbb{R}^2$ is the gravity term, $F(\dot{q}) \in \mathbb{R}^2$ denotes the friction moment, $\tau \in \mathbb{R}^2$ is the control torque and $\tau_d \in \mathbb{R}^2$ is the applied external disturbance. Simulation parameters for the robot (see Table 5.1).

Table 5.1 Parameters for simulation.

	Notation	Thigh($i = 1$)	Shank($i = 2$)
Length(m)	l_i	0.4	0.5
Center of gravity length(m)	l_{ci}	0.2	0.25
Mass(kg)	m_i	8	4
Inertia(kg · m ²)	I_i	0.32	0.2

5.3 Reference trajectory acquisition based on predictive assessment

For the early rehabilitation of lower limb movement disorder patients with very weak muscle strength, trajectory tracking control is mainly used. In order to obtain the reference trajectory, Emken et al [129] proposed the teach-and-replay technique to generate the reference trajectory. The reference trajectory was generated by replaying the recorded kinematic data. Swift et al [109] used a camera motion analysis system to generate reference trajectories for an exoskeleton lower limb gait system. However, these methods require high equipment for acquiring the reference trajectory and the relevant software systems are complex. In this section, we proposed a method to obtain the reference trajectory of an exoskeleton robot using forward dynamics (Chapter 3).

Generally, there are two ways to perform the motion equations of gait simulation: forward dynamics and inverse dynamics. Inverse dynamics has been used successfully to estimate quantities of recorded human motion that are not directly observable, such as muscle force or joint torque. Even though these inverse simulations have provided useful insights into human motion, they rely on existing data and cannot predict new behavior. Predictive forward dynamics computes motion trajectories that perform a given task optimally, according to high-level objectives such as stability, energy efficiency and pain avoidance. Predictive simulations enable musculoskeletal models to powerful new applications, such as predicting the outcome of treatment and optimizing

the efficiency and efficacy of assistive devices[82].

The system adopts the positive dynamics method to realize the simulation of different rehabilitation training, and involves patients in controlling their own rehabilitation. The remainder of this thesis offers the followings:

a. We applied SCONE to build the forward dynamic model of walking gait. After several iterations, we obtained the parameters of low limb joint at stabilization. More fundamentally, use existing models in SCONE forum, such as jumping and running models, to obtain the reference trajectories for the corresponding movements.

b. We propose an impedance controller with variable parameters for LLER robot. By means of MATLAB simulation, comparing the trajectory tracking accuracy and real-time performance of lower limb exoskeleton robot, the fuzzy controller algorithm is better than the conventional PID control algorithm.

The model considered here is a three-DOF for one foot (see Fig. 5.1), wearable LLER similar to Lokomat[64], 1-DOF for the hip joints (Flexion/extension), 1-DOF for the knee joints (Flexion/extension), and 1-DOF for the ankle joints (Dorsiflexion/ toe flexion). Each joint is independently driven by a servomotor/ball-screw assembly complete with an encoder and a force sensor for measuring its angular displacement and driving torque respectively [11].

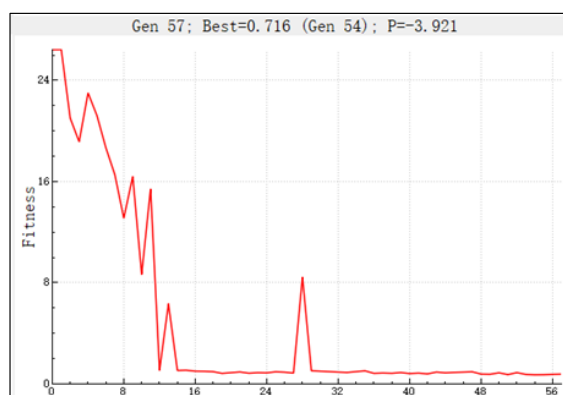


Figure 5.2 Gait fitness of predicted forward dynamics.

SCONE is open-source software for predictive simulation of biological motion. According to high-level objectives such as stability, energy efficiency and pain avoidance, it computes motion trajectories so that performs a given task optimally. In this section, the SCONE optimizer is based on the CMA-ES (Covariance Matrix Adaptation Evolution Strategy) algorithm by Hansen which is used to establish a forward dynamic model of gait walking [82]. The parameters of *CmaOptimizer* are shown in Table 5.2.

Table 5.2 Parameter CMA optimizer.

Parameter	Type	Value	Description
Mu	int	7	Mu parameter of CMA-ES.
Lambda	int	14	Lambda parameter of CMA-ES.
Sigma	double	0.100509	Initial Sigma parameter of CMA-ES.
Window_size	size_t	500	Window size used for fitness prediction.
Max_generations	size_t	1000	The maximum number of iterations without file output.

It can be seen from Fig. 5.2 that gait walking model tends to be stable after about 30 optimization operations, and the curve is smoother after 54 iterations. Therefore, we abort the optimization calculation when the optimization iteration reaches 57 times. Hence, we choose the optimize scenario when Gen = 54, Best = 0.716 as the research object.

Through the simulation with ADMAS, the moment on the knee to flexion and extension is about 50Nm and the angle scope of the freedoms on the knee is about 80° in the normal walking [130], as shown in Table 5.3.

Table 5.3 The lower limb of the exoskeleton's DOF design.

	Joints	DOF	the scope of freedoms	Driving Force Needed
The DOFs of LLER robot	hip	Flexion/extension	-120° ~ 65°	80N/m ~100N/m
	knee	Flexion/extension	(-120° ~ -160°) ~ 0°	45N/m ~70N/m
	ankle	Dorsiflexion/toe flexion	-20° ~ (40° ~50°)	Spring or other impedance

General biomechanical studies of walking frequently identify seven or more distinct phases of the human walking gait cycle[25]. To simplify the control, we divide the LLER robot into three discontinuous stages (see Fig. 5.3), which are represented by three different dynamic models:

Single support: one leg is in the stance configuration while another leg is in swing.

Double support: both legs are in stance configuration and situated flat on the ground.

Double support with one redundancy: both legs are in stance configuration, but one leg is situated flat on the ground while the other one is not.

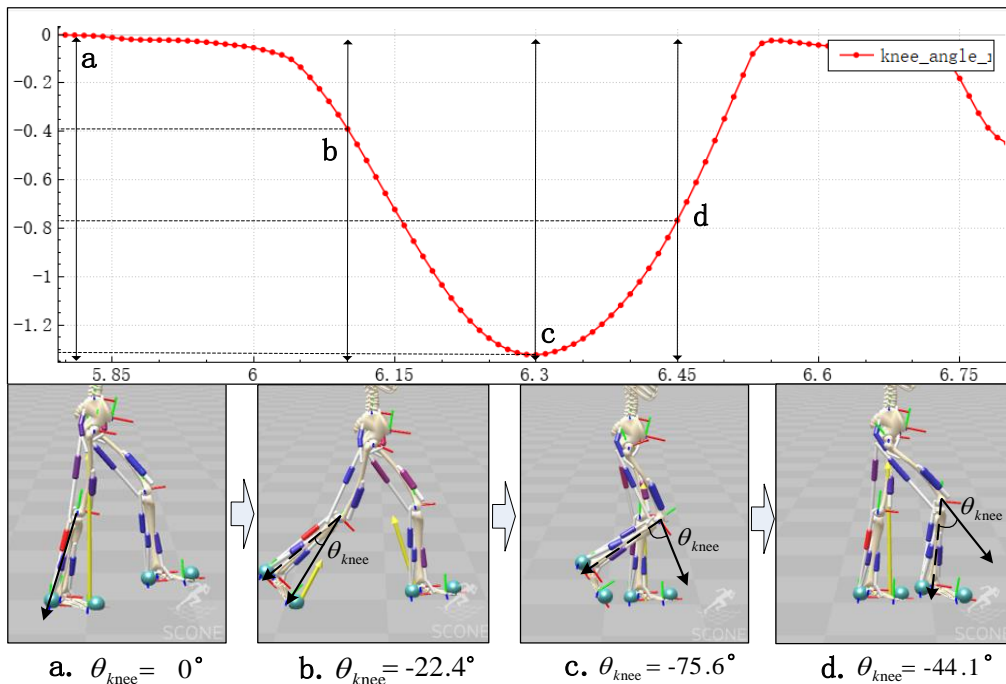


Figure 5.3 Knee changes in a gait cycle.

Using OpenSIM and SCONE, 4 characteristic moments of forward motion analysis in a walking cycle are predicted. The configuration diagram is shown in Figure 5.4. The knee joint angles of point **a**, point **b**, point **c** and point **d** are 0° , -22.4° , -75.6° , -44.1° respectively. In Fig. 5.4, the abscissa is time per second, the ordinate is the angle of the right knee joint, and the counterclockwise direction is the positive direction.

For the simulations we used the anthropometric data of a male of 65kg with 1.7m height shown in Table 5.4, which is calculated according to [31]. In order to simplify the model, the center of gravity of the two limbs are placed at the end of each segment. According to the equation (6) ~ (8) and the given parameters' values, we obtain the lower-limb dynamic equation inertia matrix $D(q)$, centrifugal force and Coriolis force vector matrix $C(q, \dot{q})$ and gravity vector matrix $G(q)$.

Table 5.4 Parameters for simulation.

	Notation	Thigh($t = 1$)	Shank($t = 2$)
Length(m)	l_i	0.4	0.5
Mass(kg)	m_i	8	4
Inertia($kg \cdot m^2$)	I_i	0.12	0.04

When Gen = 54 in Fig. 5.2, the predicted value of right knee angle during walking gait (see Fig.5.4) is taken as the input of the LLER robot controller.

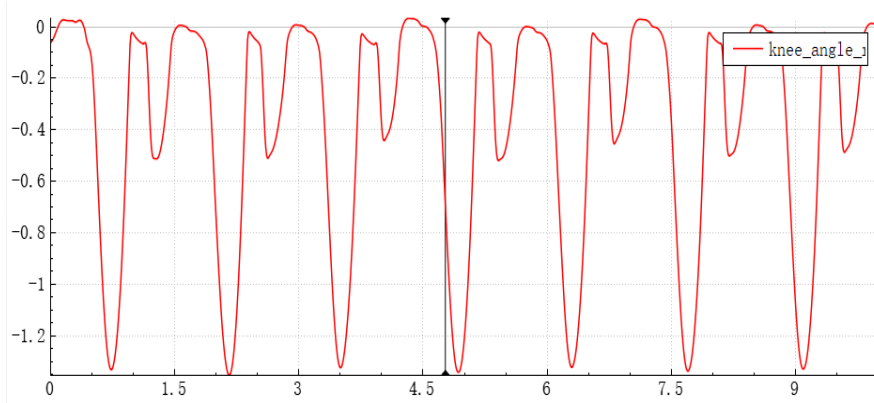


Figure 5.4 Predicted value of right knee joint angle in 0-10 seconds.

5.4 Controller for trajectory tracking model of LLER robot

5.4.1 Development of PD controller for hip-knee robot

When gravity and applied disturbances are neglected, independent PD control is used to satisfy the trajectory tracking control requirements of the robot. n-joint robot equation is

$$\tau = D(q)\ddot{q} + C(q, \dot{q})\dot{q} + g(q), \quad (5.13)$$

where $D(q) \in \mathbb{R}^{n \times n}$ is the definite inertia matrix and $C(q, \dot{q}) \in \mathbb{R}^n$ denotes the centrifugal and Coriolis force, $g(q) \in \mathbb{R}^n$ is the gravity term (see equation 5.11), τ is the joint driving torque. The independent PD control law is

$$\tau = K_d \dot{e} + K_p e, \quad (5.14)$$

take the tracking error as $e = q_d - q$, and when fixed-point control is used, q_d is a constant value, then $\dot{q}_d = \ddot{q}_d \equiv 0$. This scenario applies to the LLER robot working at low speed. Here, the robot dynamics equation is

$$D(q)\ddot{q} + C(q, \dot{q})\dot{q} + g(q) + K_p e = -K_d \dot{e}. \quad (5.15)$$

Take the Lyapunov function as

$$V = \frac{1}{2} \dot{e}^T D(q) \dot{e} + \frac{1}{2} e^T K_p e, \quad (5.16)$$

From the positive definite nature of $D(q)$ and K_p , it is known that V is globally positive definite, then

$$\dot{V} = \dot{e}^T D(q) \ddot{e} + \frac{1}{2} \dot{e}^T \dot{D}(q) \dot{e} + \dot{e}^T K_p e, \quad (5.17)$$

Using the skew-symmetry of $\dot{D} - 2C$, it is known that

$$\dot{e}^T \dot{D} \dot{e} = 2 \dot{e}^T C \dot{e}, \quad (5.18)$$

Then

$$\dot{V} = \dot{e}^T D \ddot{e} + \dot{e}^T C \dot{e} + \dot{e}^T K_p e = \dot{e}^T (D \ddot{e} + C \dot{e} + K_p e) = -\dot{e}^T K_d \dot{e} \leq 0, \quad (5.19)$$

Since \dot{V} is semi-negative definite and K_d is positive definite, then when $\dot{V} \equiv 0$, $\dot{e} \equiv 0$, and thus $\ddot{e} \equiv 0$. Taking into equation (5.15), we have $K_p e = 0$, and then by the reversibility of K_p , we know that $e = 0$. By LaSalle's theorem, $(e, \dot{e}) = 0$ is the equilibrium point of global asymptotic stability of the controlled robot, that is, from any initial condition (q_0, \dot{q}_0) , we have $q \rightarrow q_d$, $\dot{q} \rightarrow 0$.

Therefore, we developed the LLER robot with equation (5.13) as the kinetic model, choosing the 2-joint robot system (without considering friction and disturbances). Where $D(q)$ is equation (5.9), $C(q, \dot{q})$ is equation (5.10), and the initial angle and angular velocity of the LLER robot is $q_d(0) = [0.565 \quad 0.274]^T$ (rad). The controller of the hip-knee LLER robot is implemented by the PD control algorithm (see Fig. 5.5). The input angle parameters, $[\tilde{q}_{hip}, \tilde{q}_{knee}]$, are the results of the self-selected velocity simulation in Fig. 3.9 of Chapter 3.

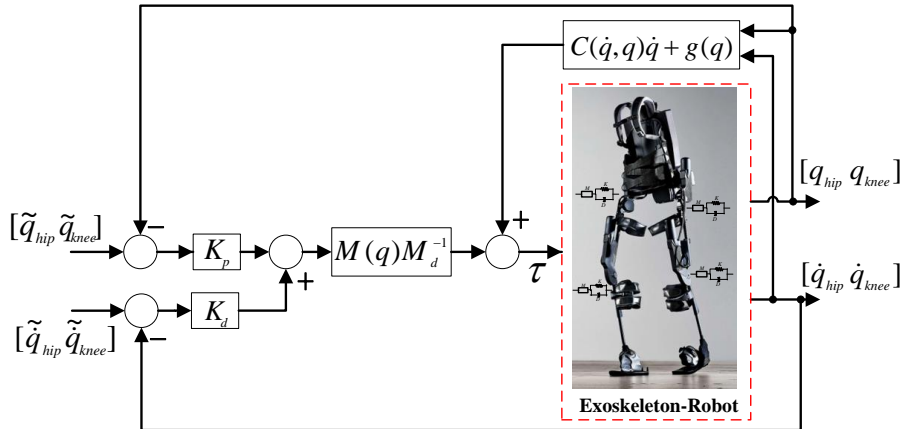


Figure 5.5 Block diagram of the PD controller for the hip-knee LLER robot.

In the controller (equation 5.15), take $K_p = \begin{bmatrix} 9000 & 0 \\ 0 & 9000 \end{bmatrix}$, $K_d = \begin{bmatrix} 1000 & 0 \\ 0 & 1000 \end{bmatrix}$, the simulation results (see Fig. 5.0 and Fig. 5.1). The LLER robot's hip joint (see Fig. 5.6A) achieves the expected tracking effect after 35% of the gait cycle (see Fig 5.6B); the knee joint (see Fig. 5.6C) achieves the expected tracking effect after 25% of the gait cycle (see Fig 5.6D). Therefore, without considering external interference, the PD-controlled LLER robot can achieve angle tracking, and this approach is suitable for the passive training session of rehabilitation training.

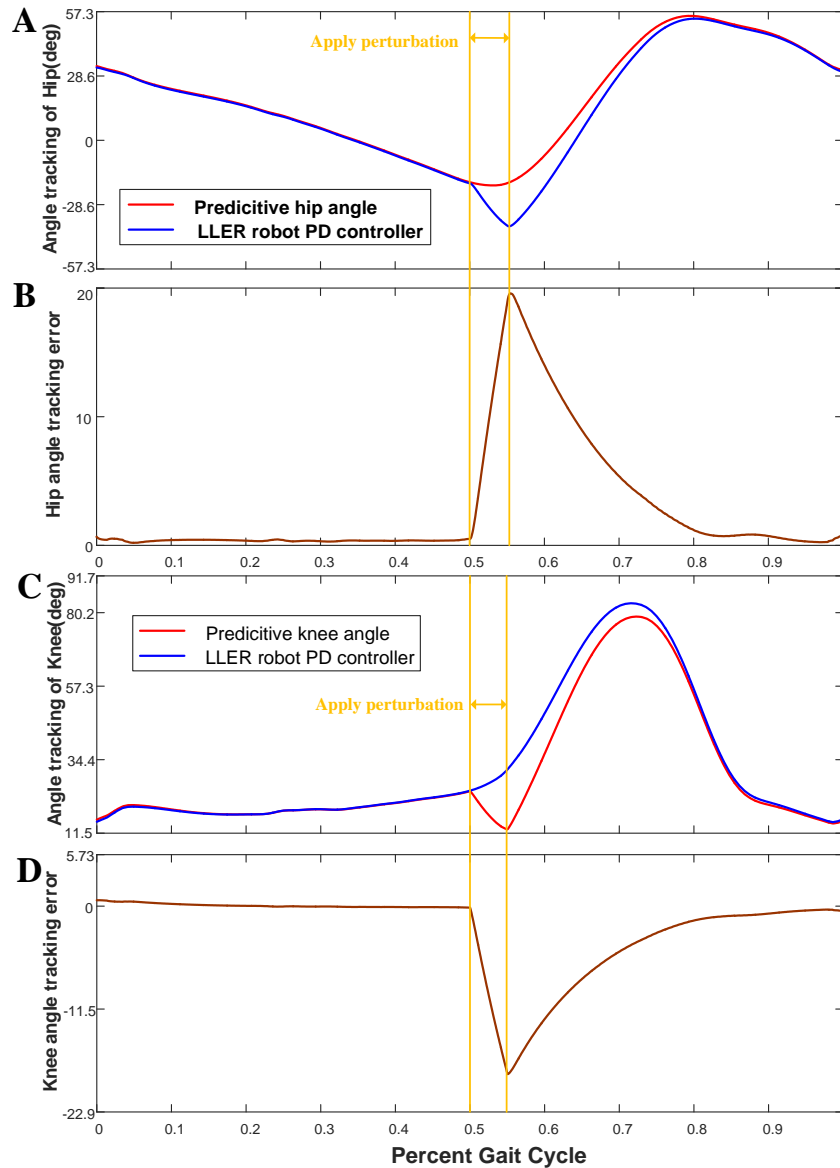


Figure 5.6 Angle tracking of the hip and knee for the robot in normal simulated gait cycle. (A) is the trajectory tracking of the LLER robot hip joint. (B) is the trajectory tracking error of the LLER robot hip joint. (C) is the trajectory tracking of the LLER robot knee joint. (D) is the trajectory tracking error of the LLER robot knee joint.

The LLER robot requires a larger torque at the hip joint (see Fig. 5.7A) near 55% and 80% of the gait cycle, respectively. The torque required for the knee joint (see Fig. 5.7B) is greatest near 70% of the gait cycle. This result indicates that the torque required at the hip and knee joint

increases with its flexion angle.

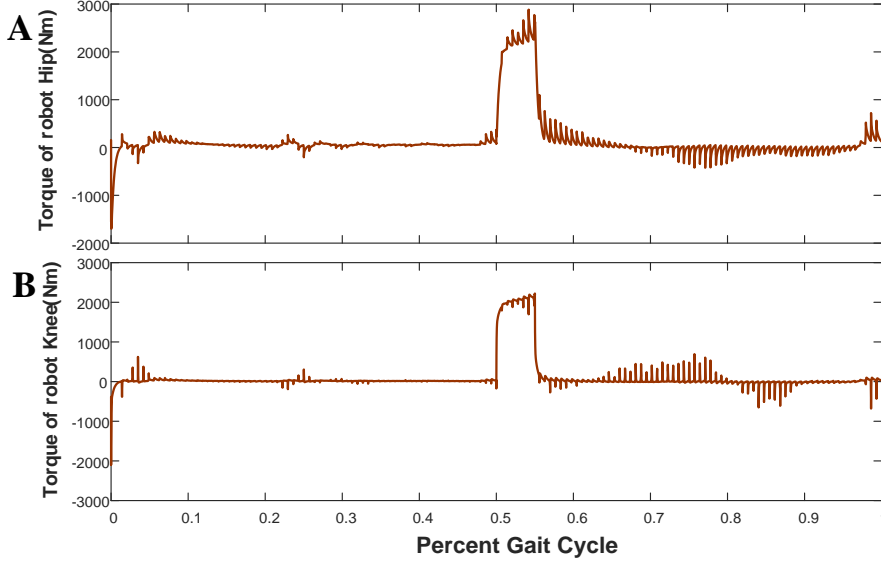


Figure 5.7 Torque generated by LLER robot's hip and knee in normal simulated gait cycle. (A) is the torque generated by the robot's hip. (B) is the torque generated by the robot's knee.

5.4.2 Development of Robust Adaptive PD Controller for LLER Robot

From the conclusions in Section 5.4.1, it is clear that linear PD control is the most effective control method for robotic systems with strong coupling and nonlinearity. However, engineering practice shows that linear PD control often requires a large initial output from the actuator (see Figure 51), and it is often impossible for the actual actuator (usually a motor) to provide excess initial torque. In view of this, many nonlinear PD control methods have been proposed, but conventional nonlinear PD controllers have only PD terms, which require still larger coefficients for the proportional and differential terms, and have the problem of large output torque. Jiao X et al.[131] proposed an adaptive robust PD control strategy to avoid the drawback of too large initial output torque. The controller consists of two parts: nonlinear PD feedback and compensated control. The robot uncertain dynamics part is compensated by an adaptive controller composed of a regression matrix, and a perturbation compensation term is designed according to the upper exact bound of the robot perturbation. The advantages of this control strategy: when the initial error is large, the PD feedback plays the main role to avoid excessive initial torque output through nonlinear PD control; when the error is small, the adaptive controller plays the main role, thus ensuring a good dynamic performance of the system.

After adding the perturbation and gravity terms to the hip-knee LLER robot described by equation (5.9), it is

$$D(q)\ddot{q} + C(q, \dot{q})\dot{q} + g(q) + \omega = \tau, \quad (5.20)$$

where $q \in \mathbb{R}^n$, is the joint angle, $D(q) \in \mathbb{R}^{n \times n}$ is the positive definite inertia matrix of the LLER robot, $C(q, \dot{q}) \in \mathbb{R}^n$ denotes the Centrifugal and Coriolis forces, $g(q) \in \mathbb{R}^n$ is the gravity term, $\tau \in \mathbb{R}^n$ is the control moment, and $\omega \in \mathbb{R}^n$ is the external disturbance.

According to the dynamics of the robot system: there exists a parameter vector that depends

on the robot parameters and makes $D(q)$, $C(q, \dot{q})$, and $g(q)$ satisfy the linear relationship:

$$D(q)\vartheta + C(q, \dot{q})\rho + g(q) = \Phi(q, \dot{q}, \rho, \vartheta)P, \quad (5.21)$$

where $\Phi(q, \dot{q}, \rho, \vartheta) \in R^{n \times m}$, is the regression matrix of known joint variable functions, which is the matrix of known functions of the generalized coordinates of the robot and its derivatives of all orders; $P \in R^n$ is the vector of unknown constant parameters describing the mass characteristics of the robot. Then, the parametrization of the external perturbation term ω satisfies.

$$\|\omega\| \leq d_1 + d_2\|e\| + d_3\|\dot{e}\|, \quad (5.22)$$

where d_1 , d_2 and d_3 are the positive constants, $e = q - q_d$, $\dot{e} = \dot{q} - \dot{q}_d$ are the tracking error and tracking error derivative, respectively. Introducing the variables y and q_r , let

$$y = \dot{e} + \gamma e, \quad (5.23)$$

$$\dot{q}_r = \dot{q}_d + \gamma e, \quad (5.24)$$

where $\gamma \geq 0$, is a constant, gives

$$y = \dot{q} - \dot{q}_r, \quad (5.25)$$

For equation (5.21), taking $\vartheta = \ddot{q}_r$, $\rho = \dot{q}_r$, gives

$$D(q)\ddot{q}_r + C(q, \dot{q})\dot{q}_r + g(q) = \Phi(q, \dot{q}, \dot{q}_r, \ddot{q}_r)P, \quad (5.26)$$

Taking equation (5.25) into equation (5.26) we get

$$D(q)(\ddot{q} - \ddot{y}) + C(q, \dot{q})(\dot{q} - y) + g(q) = \Phi(q, \dot{q}, \dot{q}_r, \ddot{q}_r)P, \quad (5.27)$$

Combining equation (5.20) and simplifying it, we get

$$D(q)\ddot{y} + C(q, \dot{q})\dot{y} = \tau - \Phi(q, \dot{q}, \dot{q}_r, \ddot{q}_r)P - \omega, \quad (5.28)$$

For the LLER robot system, when the disturbance signal is known with upper exact bound, we use the following controller and adaptive law [131] to ensure the global asymptotic stability of the system.

$$\tau = -K_p e - K_v \dot{e} + \Phi(q, \dot{q}, \dot{q}_r, \ddot{q}_r)\hat{P} + u, \quad (5.29)$$

$$u = [u_1 \cdots u_n]^T, \quad u_i = -(d_1 + d_2\|e\| + d_3\|\dot{e}\|)\text{sgn}(y_i), \quad (5.30)$$

where the parameter estimation law of \hat{P} is taken as:

$$\dot{\hat{P}} = -\Gamma \Phi^T(q, \dot{q}, \dot{q}_r, \ddot{q}_r)y, \quad (5.31)$$

in which

$$\begin{aligned} K_p &= K_{p_1} + K_{p_2} B_p(e), \quad K_v = K_{v_1} + K_{v_2} B_v(\dot{e}), \\ K_{p_1} &= \text{diag}(k_{p_{11}}, k_{p_{12}}, \dots, k_{p_{1n}}), \quad K_{p_2} = \text{diag}(k_{p_{21}}, k_{p_{22}}, \dots, k_{p_{2n}}), \\ K_{v_1} &= \text{diag}(k_{v_{11}}, k_{v_{12}}, \dots, k_{v_{1n}}), \quad K_{v_2} = \text{diag}(k_{v_{21}}, k_{v_{22}}, \dots, k_{v_{2n}}), \\ B_p(e) &= \text{diag}\left(\frac{1}{\alpha_1 + |e_1|}, \frac{1}{\alpha_2 + |e_2|}, \dots, \frac{1}{\alpha_n + |e_n|}\right), \\ B_v(\dot{e}) &= \text{diag}\left(\frac{1}{\beta_1 + |\dot{e}_1|}, \frac{1}{\beta_2 + |\dot{e}_2|}, \dots, \frac{1}{\beta_n + |\dot{e}_n|}\right), \end{aligned} \quad (5.32)$$

where $k_{p_{1i}}$, $k_{v_{1i}}$, α_i , β_i , ($i = 1, 2, \dots, n$) are positive, and Γ is a positive definite symmetric matrix.

The stability proof of this controller is provided in [131]. Further we need to determine the Φ and \mathbf{y} in equation (5.31).

For the lightweight exoskeleton robot, we assume that the center of gravity of the thigh and the thigh exoskeleton in Fig. 5.1 is located at the joint, that is, $l_1 = l_{c1}$, $l_2 = l_{c2}$. Then, the terms $D(q)$, $C(q, \dot{q})$ and $g(q)$ in equation (5.20) can be simplified as

$$\begin{bmatrix} D_{11}(q_2) & D_{21}(q_2) \\ D_{12}(q_2) & D_{22}(q_2) \end{bmatrix} \begin{bmatrix} \ddot{q}_1 \\ \ddot{q}_2 \end{bmatrix} + \begin{bmatrix} -C_{12}(q_2)\dot{q}_2 & -C_{12}(q_2)(\dot{q}_1 + \dot{q}_2) \\ C_{12}(q_2)\dot{q}_1 & 0 \end{bmatrix} \begin{bmatrix} \dot{q}_1 \\ \dot{q}_2 \end{bmatrix} + \begin{bmatrix} g_1(q_1, q_2) \\ g_2(q_1, q_2) \end{bmatrix} = \begin{bmatrix} \tau_1 \\ \tau_2 \end{bmatrix}, \quad (5.33)$$

In which

$$\begin{aligned} D_{11}(q_2) &= (m_1 + m_2)l_1^2 + m_2l_2^2 + 2m_2l_1l_2\cos q_2 \\ D_{12}(q_2) &= D_{21}(q_2) = m_2l_2^2 + m_2l_1l_2\cos q_2 \\ D_{22}(q_2) &= m_2l_2^2 \\ C_{12}(q_2) &= m_2l_1l_2\sin q_2 \\ g_1(q_1, q_2) &= (m_1 + m_2)l_1\cos q_2 + m_2l_2\cos(q_1 + q_2) \\ g_2(q_1, q_2) &= m_2l_2\cos(q_1 + q_2), \end{aligned} \quad (5.34)$$

For the dynamic equation

$$D(q)\ddot{q}_r + C(q, \dot{q})\dot{q}_r + g(q) = \Phi(q, \dot{q}, \ddot{q}_r)P, \quad (5.35)$$

In order to implement the control law equation (5.29), equation (5.30) and equation (5.31), the expressions for Φ and P in equation (5.35) must be given.

Combining equation (5.33) and equation (5.35), we get

$$\begin{aligned} [D(1,1) \quad D(1,2)]\ddot{q}_r + [C(1,1) \quad D(1,2)]\dot{q}_r + g(1) \\ = [\phi_{11} \quad \phi_{12} \quad \phi_{13}] \begin{bmatrix} p_1 \\ p_2 \\ p_3 \end{bmatrix}, \end{aligned} \quad (5.36)$$

$$\begin{aligned} [D(2,1) \quad D(2,2)]\ddot{q}_r + [C(2,1) \quad D(2,2)]\dot{q}_r + g(2) \\ = [\phi_{21} \quad \phi_{22} \quad \phi_{23}] \begin{bmatrix} p_1 \\ p_2 \\ p_3 \end{bmatrix}, \end{aligned} \quad (5.37)$$

where

$$\begin{aligned} p_1 &= (m_1 + m_2)l_1^2 \\ p_2 &= m_2l_2^2 \\ p_3 &= m_2l_1l_2 \\ \phi_{11} &= \ddot{q}_{1r} + g/l_1\cos q_2 \\ \phi_{12} &= \ddot{q}_{1r} + \ddot{q}_{2r} \\ \phi_{13} &= 2\ddot{q}_{1r}\cos q_2 + \ddot{q}_{2r}\cos q_2 - \dot{q}_2\dot{q}_{1r}\sin q_2 - (\dot{q}_1 + \dot{q}_2)\dot{q}_{2r}\sin q_2 + g/l_1\cos(q_1 + q_2) \\ \phi_{21} &= 0 \\ \phi_{22} &= \phi_{12} \\ \phi_{23} &= \dot{q}_1\dot{q}_{1r}\sin q_2 + \ddot{q}_{1r}\cos q_2 + g/l_1\cos(q_1 + q_2), \end{aligned} \quad (5.38)$$

where $g = 9.8$, $\Phi(q, \dot{q}, \ddot{q}_r) = \begin{bmatrix} \phi_{11} & \phi_{12} & \phi_{13} \\ \phi_{21} & \phi_{22} & \phi_{23} \end{bmatrix}$, $P = [p_1 \ p_2 \ p_3]^T$.

Based on the above description, we built the robust adaptive PD control system, as shown in Fig. 5.8.

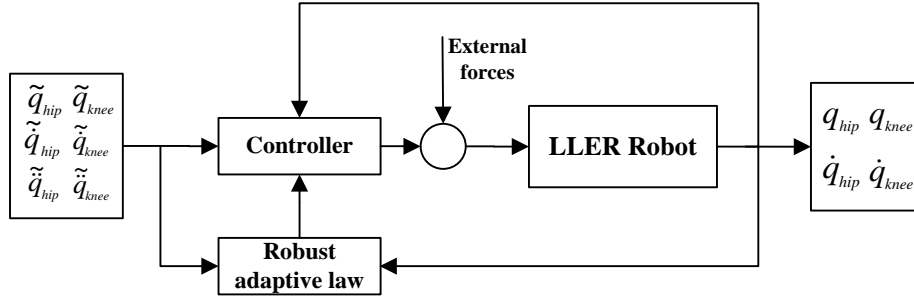


Figure 5.8 Block diagram of the robust adaptive PD controller for the hip-knee LLER robot.

The inputs to the robust adaptive PD controller (see Fig.5.8) are the hip and knee angle, angular velocity and angular acceleration data from the predicted assessment results (see *Self-selected Speed* in Fig. 3.9). Controller (see Fig. 5.8) is the description of equations 5.36 and 5.37 using the S function of MATLAB. Robust adaptive law in Fig.5.8 is the description of equation 5.31 using the S function, and LLER robot is the description of equation 5.20 using the S function. After simulation of this controller model, the results are shown in Fig. 5.9.

We set the initial position of the LLER robot to be the same as the initial position of the gait for the prediction assessment (see Fig. 5.9). Figs. 5.9A and 5.9B show that overall the robust adaptive PD controller is able to achieve tracking to the expected motion trajectory of the LLER robot. After applying external perturbations during 50%-55% of the gait cycle, Fig. 5.9B shows that the trajectory tracking error of the knee increases immediately, followed by a gradual decrease of the error. However, the error of the hip trajectory tracking becomes smaller rapidly after 50% of the gait cycle instead, reflecting the good robustness of this controller. As shown in Fig. 5.9E and Fig. 5.9F, the velocity tracking of both the hip and knee exhibits a sharp change in velocity at the beginning of the gait. This is caused by the fact that the velocity of the LLER robot is changing from 0 although the initial angle is set to the same value as the predicted assessment. Figs. 5.9G and 5.9H show that the angular velocity tracking errors of the hip and knee show significant oscillation during the application of external perturbations. This phenomenon is caused by the application of external perturbations.

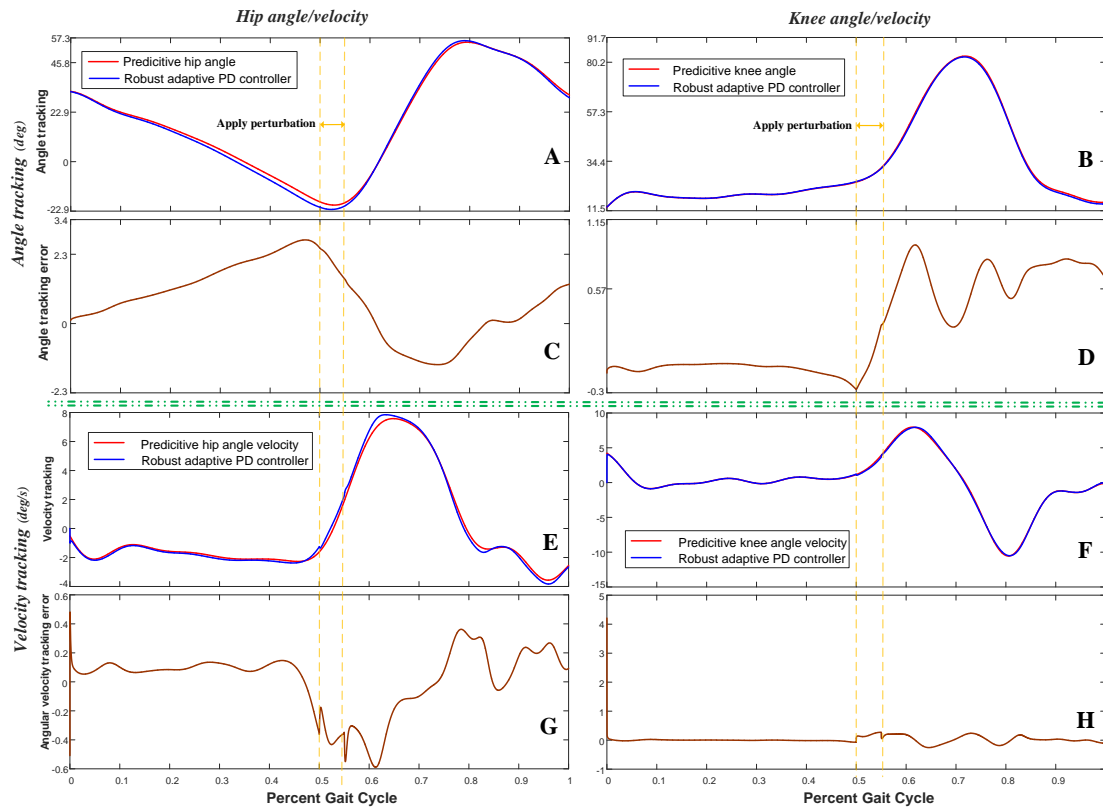


Figure 5.9 Simulation results of the robust adaptive PD controller for the LLER robot. (A) and (B) show the angle trajectory tracking of the hip and knee, respectively. (C) and (D) presents the angle tracking errors of the hip and knee, respectively. (E) and (F) are the angle velocity tracking of ankle and knee, respectively. (G) and (H) show the angle velocity tracking errors of hip and knee, respectively.

5.5 Variable parameter impedance controller with gravity compensation

In social applications such as elderly care, health care and human-robot collaboration, environments are typically unknown to robots and there exist uncertainties due to many factors. Therefore, control of the interaction between robots and environments is essential and there has been much effort made on this topic. In the literature on interaction control, two approaches are widely studied, i.e., hybrid position /force control [132] and impedance control [133][134]. Compared to hybrid position/force control, impedance control is more feasible in the sense that it does not require the decomposition of two directions. Besides, impedance control is preferred for its better robustness [135]. However, in many situations, imposing a passive impedance model on the robot is too conservative, and the environmental dynamics can be taken into consideration to obtain desired impedance model. Besides, a fixed prescribed impedance model does not suffice in many applications[136]. In human-robot collaboration, variable impedance control is necessary.

The classical approach to robot control is negative feedback control with high proportional-derivative (PD) gains. This type of control is straightforward to implement robust towards modeling uncertainties, and computationally cheap. Unfortunately, high-gain control is not ideal for many tasks involving interaction with the environment, e. g force control tasks or locomotion. In contrast, impedance control (Hogan 1985) seeks to realize a specific impedance of the robot,

either in the end-effector or joint space. The issue of specifying the target impedance, however, has not yet been completely addressed[137].

5.5.1 Variable parameter impedance controller for LLER robotics

With impedance control, the robot is controlled to be compatible with the interaction forces exerted by the environment, thus ensuring the safety of the robot and the environment. Specifically, if the environment is also passive, imposing a passive impedance model on the robot will ensure interaction stability[136]. LLER human-robot collaboration is characterized by the physical contact between the human, the robot and its surroundings during the collaboration process, which in turn forms a coupled dynamic system. Therefore, our LLER robotics system has 3 metrics, namely: safety, collaboration and intelligence. In this thesis, we focus on safety and collaboration, and the intelligence of the LLER robot will be one of our main tasks in the future.

In order to make both the hip and knee joints of the LLER robot have the dynamic properties of the second-order system composed of spring-damping-mass. The impedance control relationship is:

$$M_d\ddot{E} + B_d\dot{E} + KE = -F_e, \quad (5.39)$$

where, F_e represents the contact force with the environment, $\tau_d = -F_e$. M , B , and K denote the inertia matrix of the impedance model, damping matrix and stiffness matrix of the robot, respectively. E denotes the error between the actual position and the desire position ($E = q_d - q$), \ddot{q}_d , \dot{q}_d , q_d are the expected input angle acceleration, angular velocity and angle value, respectively.

The dynamic equation of the LLER robot is

$$\tau = D(q)\ddot{q} + C(q, \dot{q})\dot{q} + g(q) + \tau_d, \quad (5.40)$$

Where $\tau_d = -F_e$, Combining (1) and (2), we get

$$\tau = D(q)\ddot{q}_d + C(q, \dot{q})\dot{q} + g(q) + D(q)M^{-1}(B\dot{E} + KE) + (I - D(q)M^{-1})\tau_d, \quad (5.41)$$

The equation (5.41) can be obtained by taking equation (5.41) into equation (5.39) and multiplying both sides of the equation by $D^{-1}(q)$ and M respectively after eliminating the same term.

The impedance control model described in equation (5.41) can achieve: a dynamic control relationship between the locomotion of the LLER robot and the contact forces between the robot and the external environment. The ideal impedance controller block diagram is shown in Fig. 5.10.

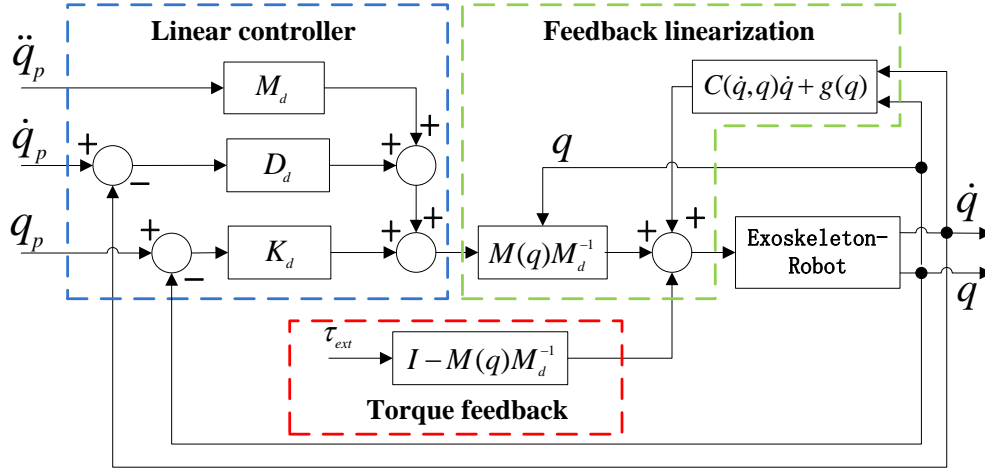


Figure 5.10 Schematics illustrating of ideal impedance control system for LLER robot. The input to the control system is the predicted joint angles and joint loads after the optimization [138]. In the exoskeleton robot model, we assume that the simulation parameters for the robot are Table 5.1.

Fig. 5.10 represents the single-leg hip and knee joints both reflecting the dynamic characteristics of a second-order system consisting of a spring-damped-mass. $C(q, \dot{q})\dot{q} + g(q)$ is the robot gravity compensation. However, the model for the conversion of external force to joint angular acceleration, $(I - D(q)M_d^{-1})F_{ext}$ (see red dashed area in Fig. 5.10), requires real-time feedback sensors for joint moments to be installed in each joint of the rehabilitation robot to achieve its goals, which also makes the design of the rehabilitation robot more difficult.

In addition, the system needs to provide accurate stiffness matrix for robot dynamics and stiffness matrix for impedance controller. However, for different affected limbs, this problem is difficult to solve and can cause instability for the system due to the strong coupling of the second-order terms. Therefore, based on this system, we designed the PD-based impedance control system.

Considering that the LLER robot we developed is mainly used in the passive training stage of the affected limb initial training. Owing to the gentler training in this period and the relatively small joint angular acceleration, the inertia term in the impedance model is considered to be equivalent to the inertia term in the kinematic model, which eliminates the torque feedback term. With this processing, our impedance model is simplified to a first-order PD-based impedance control system (see Fig. 5.11). Although the PD impedance control system theoretically causes an increase in the error between the actual and desired values, the error can be eliminated by adjusting the offset values, considering that each joint parameters obtained from the forward simulation module require the physiotherapist to adjust the offset values according to the affected limb rehab course.

The red dashed area (see Fig.5.10) in the impedance control block diagram indicates the torque feedback. Because the application scenario of our framework is a low-speed and gentle rehabilitation movement. It is difficult to obtain real-time feedback of the LLER robot joint torque, special torque sensors or predictive calculations of the joint motor current are required. Therefore, the inertia matrix of the impedance control is taken as the inertia matrix of the robot, $D(q) = M$, then equation (5.41) is simplified as

$$D(q)\ddot{E} + B\dot{E} + KE = \tau_d, \quad (5.42)$$

To simplify, let $\ddot{q}_d = 0$, $\dot{q} = 0$ and equation (5.42) obtains

$$\tau = C(\dot{q}, q)\dot{q} + g(q) - B_d\dot{q} + K_d\dot{E}, \quad (5.43)$$

After the above simplification, the impedance control model of LLER still has impedance characteristics to the external environment. However, when the acceleration of the joint is large, the result will have a large error with the set value.

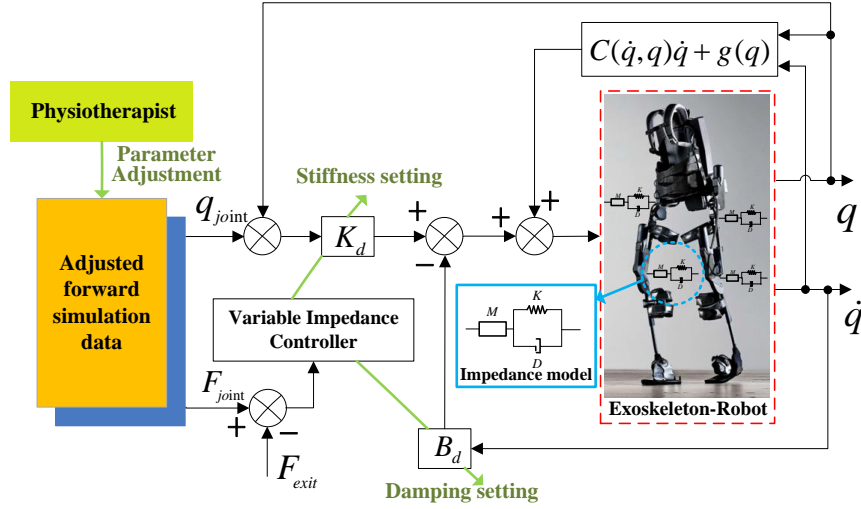


Figure 5.11 Architectural framework of variable impedance PD controller based on predictive assessment. The inputs to the control system are optimized predicted joint angles and joint loads with offset values set by the physiotherapist [138]. In the exoskeleton robot model, we assume that the masses, lengths and momentum of Inertia for shank and thigh are $8kg$, $0.5m$ and $0.4kgm^2$, respectively.

The red dotted box (see Fig. 5.11) shows the exoskeleton robot hip and knee joints both applying the impedance control of equation (5.43). The variable impedance controller in the black dotted box (see Fig. 5.11) allows the physiotherapist to adjust the impedance parameters K_d and B_d according to the rehabilitation training needs. For example, the physiotherapist can increase the damping coefficient when active training of the affected limb is required, and similarly, the elasticity coefficient can be increased when the robot is required to drive the affected limb for passive training. The rules for determining the impedance parameters will be investigated in our next work.

5.5.2 Simulation of LLER robot knee joint tracking with impedance controller based on variable parameters

We developed a dynamics model for the LLER robot (see equation 5.12) and a PD-based impedance control system (see equation 5.43) using MATLAB's S-function (MathWorks, Natick, Massachusetts, USA). Meanwhile, a sinusoidal external disturbance force with a gain of $300N$ was applied to the model in SIMULINK during 25% to 30% of the gait cycle to validate the model's robustness. We selected the predicted optimized simulation data for the two scenarios where the variance in knee angle changes in gait cycle is the sharpest: severe contracture and severe muscle

weakness, to validate the knee angle trajectory and torque tracking effect of the rehabilitation robot system. We need to emphasize that the purpose of the predictive assessment module is to form a new clinical gait analysis approach by reproducing the pathological gait through forward predictive simulation, where the acquired joint parameters are evaluated by the physiotherapist and set appropriate offsets as desired parameters for the rehabilitation robot to guide its operation. In addition, the PD-based impedance model allowed to tune the damping or stiffness values according to the rehabilitation training requirements to achieve the elasticity effect or the tracking effect of the robot.

The initial state of the robot knee joint is stationary, the top row (Fig. 5.12) knee angle trajectory tracking in the early stage of gait, the robot can follow to the desired value within 5% of the gait cycle. It is also observed that the larger stiffness value makes the angular trajectory tracking of the system significant, and only in the swing phase the robot has some lags. In the bottom row (Fig. 5.12) knee load tracking, in the initial stage, the robot needs a large torque to start the robot knee joint, which is also in line with the practical experience. In addition, the load tracking effect deteriorates in both validation scenarios when external force perturbations are applied, and our next work will consider implementing torque detection devices to solve the problem.

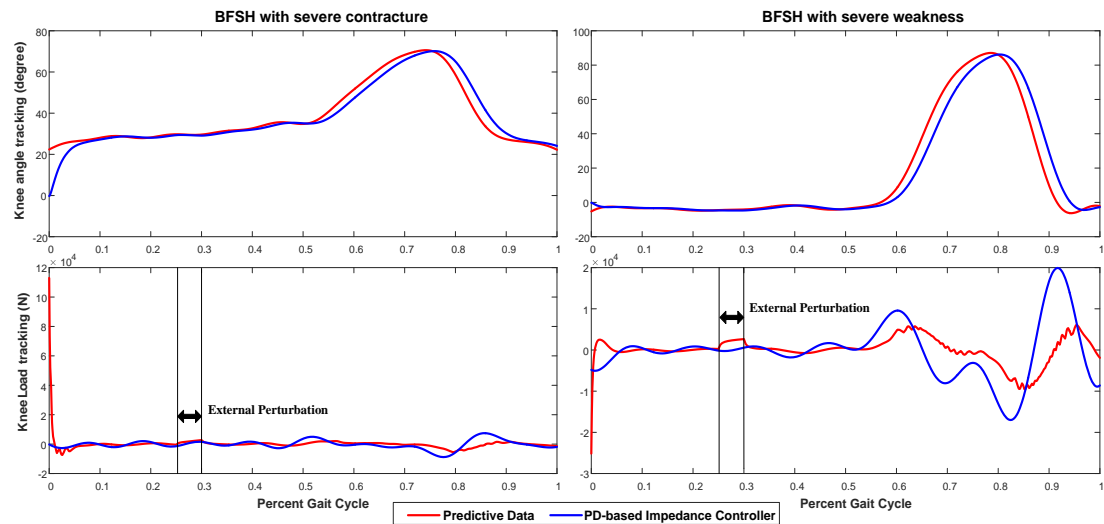


Figure 5.12 Knee joint angle trajectory and load tracking. The left and right columns are robot tracking for the forward predictive assessment of BFSH contracture severity and muscle weakness severity, respectively. The top row presents the robot knee trajectory tracking and the bottom row presents the robot knee load tracking.

The approximate clinical gait knee flexion angle and torque parameters obtained using the predictive forward simulation module are used as inputs to the lower limb exoskeleton rehabilitation robot controller with variable impedance parameters. The input values and impedance parameters allowed for adjustment by the physiotherapist depending on the rehabilitation situation.

We performed simulations for the variable parameter impedance controller with gravity compensation in MATLAB. Three sets of impedance parameters ($B_d = 10Ns/m$, $K_d =$

5000N/m, $B_d = 50Ns/m$, $K_d = 500N/m$ and $B_d = 50Ns/m$, $K_d = 5000N/m$) were set and external sinusoidal perturbations disturbance was applied during 35%-40% of the gait cycle. The robot knee joint angle trajectory tracking and torque tracking in gait cycle were obtained separately (see Fig. 5.13).

The simulation results show that the knee joint angle trajectory tracking and torque tracking of our established robot controller model are effective. When external perturbations are applied, both robot knee joint angle tracking and torque tracking vary greatly with different impedance parameters. Specifically, the large stiffness of the impedance controller makes the robot knee joint angle tracking excellent in real-time, and the large damping of the impedance controller renders the robot knee joint show more obvious elasticity when it receives external resistance.

The knee moment for the optimized gait is consistent with the overall trend of the experimental data, however, between 35% and 45% of the gait cycle (from the right foot leaving the ground to the start of swing). It might be caused by the error between the model center of gravity and the normal human model center of gravity position during the motion. During 80% to 100% of the gait cycle (from right heel touching the ground to left toe off the ground), the simulation deviated from the experiment, and the model trunk tilted forward prematurely. The knee joint angle in the optimized gait of a normal human is smaller than the experimental data in the stance phase. The optimized model exhibited leg stiffness in the stance phase, probably owing to the inadequate design of the model muscle actuators, which could not mimic completely the effect of human lower limb muscle groups on the knee joint.

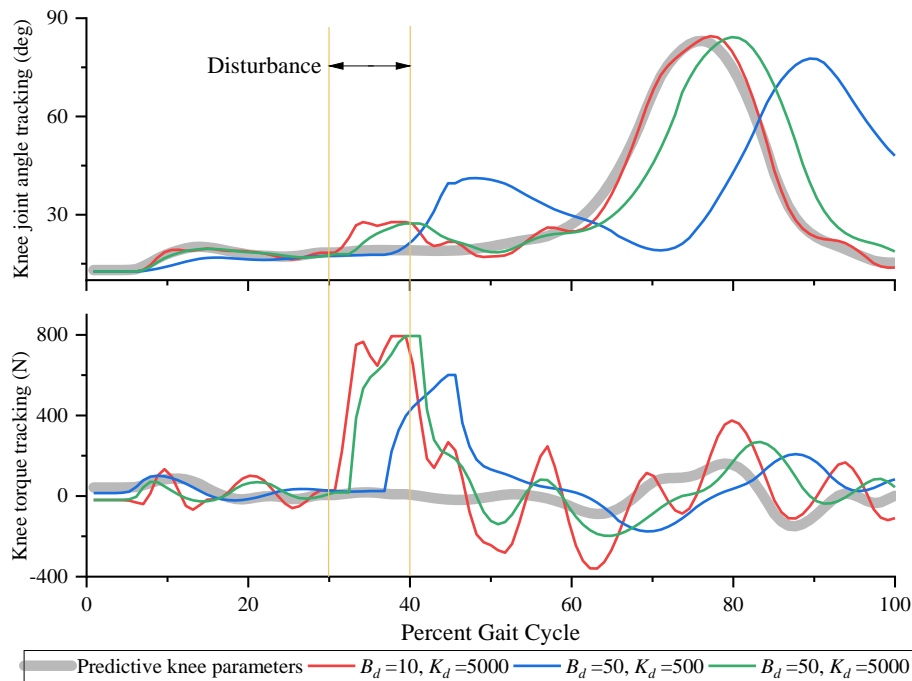


Figure 5.13 Knee joint angle trajectory tracking and torque tracking. The parameters obtained from the uninjured walking simulation (gray area) are compared to the angular tracking (top) and moment tracking (bottom) of the robot knee joint with three different impedance parameters, Damping B_d (Ns/m) and Stiffness K_d (N/m).

5.5.3 Development of impedance tuning approach based on a novel PSO algorithm

The tuning of the stiffness and damping parameters of the impedance controller involved in the previous section usually relies on experience, which results in low efficiency and poor accuracy. In the dynamic process, we are trying to develop a hybrid controller for PD impedance parameter optimization based on the PSO algorithm (see Fig. 5.14). Based on the mechanical impedance parameters of the affected limb obtained from online identification, the PSO algorithm is applied to dynamically tune the target impedance control parameters. The aim is to realize that the LLER robot can effectively adapt to the changes in the condition of the affected limb, so that the impedance controller can achieve better smoothness and stability. The blue area (see Fig. 5.14) presents setting the optimization-seeking bounds for the damping B_d and stiffness K_d in PSO algorithm to reduce the computation time and improve the optimization quality.

PSO is a random search algorithm based on group collaboration developed by simulating birds foraging for food [139]. The algorithm uses the velocity-position model, and the particle swarm velocity-position update formula is as follows

$$v_{id} = w * v_{id} + c_1 r_1 (p_{id} - x_{id}) + c_2 r_2 (p_{gd} - x_{id}), \quad (5.44)$$

$$x_{id} = x_{id} + v_{id}, \quad (5.45)$$

Where r_1 and r_2 are two separately generated uniformly distributed random numbers in the range $[0,1]$, c_1 and c_2 are learning factors[140]. The algorithm repeats the velocity and position of the new particles according to equations (5.45) and (5.46) until the maximum number of cycles is reached, or a predetermined minimum fitness threshold is satisfied, at which point the result is the optimal solution. According to equation (5.44), the particle velocity update is mainly determined by three components. The first part of equation (5.44) is the inertia, which reflects the motion habit of the particle and represents the tendency of the particle to maintain its previous velocity. The second part is cognitive, which reflects the memory of the particle's historical experience and represents the tendency of the particle to approach the best position in its history [141]. The third part is social cognition, which responds to the group-historical experience of collaborative cooperation and knowledge sharing among particles and represents the tendency of particles to approach the best position in the group or threshold history. Therefore, the learning factors c_1 and c_2 in PSO reflect the information exchange between particle populations [142].

Although the PSO algorithm converges quickly and has low computational complexity, it is prone to diversity loss and falls into local optimum [143]. With the traditional PSO algorithm, the learning factor is set to $c_1=c_2=2$. For the purpose of enriching particle diversity and improving the case of overripening and falling into local extremes, we tried to design the equal random learning factor improvement approach to obtain better convergence [144]. Therefore, the relatively better search results are selected as the random interval for the learning factor. The novel PSO is implemented in equation (5.44), the values of c_1 and c_2 are randomly taken from 0.5 to 2.0, respectively. The equations are as follows

$$c'_1 = c'_2 = 1.3 + (2.0 - 1.3)rand(), \quad (5.46)$$

Take equation (5.46) into equation (5.44) and get

$$v_{id} = w * v_{id} + c'_1 r_1 (p_{id} - x_{id}) + c'_2 r_2 (p_{gd} - x_{id}), \quad (5.47)$$

where equation (5.47) and equation (5.45) together form the equal random learning factor PSO algorithm in this thesis. We performed this novel PSO based on the designed PD impedance parameter optimization hybrid controller to explore whether it contributes to the optimization of impedance parameters. To obtain optimal control results, the novel algorithm optimizes the impedance parameters when the ITAE standard is reached.

$$J = \int_0^{\infty} t|e(t)dt| , \quad (5.48)$$

where J is the ITAE criterion; $e(t)$ denotes the deviation value from the target impedance. The flow chart of the developed hybrid controller for impedance parameter optimization based on PSO algorithm is shown in Fig. 5.14.

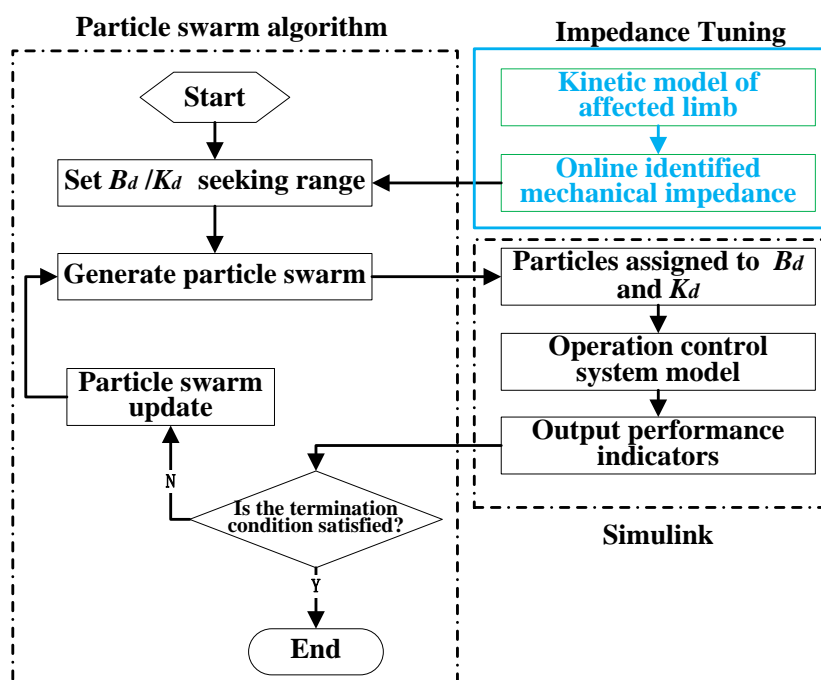


Figure 5.14 Flowchart for the hybrid controller based on PSO algorithm.

This novel PSO algorithm proved to be effective in solving the pure hysteresis problem met in process control[139]. Theoretically, the method can be used to improve the optimization of the target impedance, but it requires online identification of the impedance parameters of the obtained affected limb. We will solve this problem in future work.

5.6 Conclusion

This chapter established the kinematics and kinetics model of the hip-knee robot. A PD controller with gravity compensation was developed, and the simulation results verified that the controller can basically realize the trajectory tracking of hip and knee joints. Then, a robust adaptive PD controller was designed. This controller not only eliminates the excessive initial torque output of the system but also significantly improves the anti-interference capability. Finally, a variable parameter impedance controller was designed to address the need for different damping effects and elasticity effects during the rehabilitation process. This controller allows the physical

therapist to adjust the damping and stiffness values according to the rehabilitation needs to achieve the desired damping effect and stiffness effect, thus improving the rehabilitation efficiency of the affected limb.

Chapter 6. Conclusions

6.1 Contributions

This article dealt with a framework for clinical gait analysis of an exoskeleton rehabilitation robot based on predictive assessment. Firstly, the musculoskeletal model of the affected limb is modified using OpenSim based on medical advice, and the modified model is simulated by SCONE for predictive optimization, aiming to reappear the pathological gait. In this thesis, taking the BFSH muscle groups as an example, the effects of BFSH muscle contracture and weakness on the knee joint motion are studied separately for three severity: mild, moderate and severe. The simulation shows that at different severity of BFSH contracture and BFSH muscle weakness, there are varying impacts on both walking speed and maximum knee flexion angle. And then, based on the musculoskeletal model, the lower limb exoskeleton rehabilitation robot control system model based on impedance control is designed, and the optimized parameters of each joint are applied as the desired values of the exoskeleton robot, and the PID control parameters are tuned offline basing on the desired values to realize the trajectory tracking and load torque tracking of the rehabilitation robot. The simulation result shows that the knee joint angle tracking and load tracking of the lower limb exoskeleton rehabilitation robot based on impedance control can be adjusted in real-time in healthy gait and severe contracture gait, respectively, which realizes the customized setting of each parameter of the rehabilitation robot according to different pathological gait during the passive training in the initial rehabilitation stage, so that the robot can gradually correct the pathological gait trajectory of the affected limb on the basis of the pathological gait trajectory of the affected limb and avoid the injury during this period. Finally, the activation of BFSH in continuous gait is detected by using EMG sensors, and the experimental result shows that BFSH mainly affected the swing phase of the lower limb in one gait cycle, which verified that the predictive simulation assessment model is correct and feasible.

In this thesis, we model pathological gait by predicting forward dynamics, using minimizing the total cost of transport within a self-selected speed while ensuring head stability as a high-level goal. The gait controller utilizes a combination of state machines and low-level control laws to determine the excitation, and calculate the optimal motion trajectory to perform a given task. We attempted to explore the characteristics for reproducing the patient's gait just by modifying the parameters of the model muscles. Therefore, mild, moderate and severe muscle weakness or contractures were applied to the HAMS, GAS and BFSH muscle groups, respectively, and the models were trained to walk at self-selected speeds. Finally, we developed an impedance control model for the lower limb exoskeleton rehabilitation robot: we adopted the knee joint angle and torque parameters optimized by using predictive forward dynamics simulation as the expected values for the robot in order to achieve customized tuning for the robot motion trajectory. The framework not only realizes progressive rehabilitation training but also reduces the wearer's resistance.

A novel approach of clinical gait analysis based on predictive assessment for the exoskeleton rehabilitation robot is proposed, which mainly consists of a clinical gait assessment module based on predictive simulation and a variable parameter impedance robot controller module with gravity compensation. The thesis established a musculoskeletal model for predictive forward simulation

and opted for self-selected speed to investigate the impact relationships of the model's HAMS, GAS and BFSH muscle groups on the knee joint in gait cycle, respectively. On this basis, it was proposed that the parameters of the predictive simulation muscle model were appropriately modified according to the affected limb diagnosis combined with the impact relationships of the model muscle groups on the knee joint to obtain the simulation model and the optimized parameters of each joint to obtain the maximum matching of the clinical gait. Real-time parameters of knee joint angle and torque in gait cycle were applied as the expected values of impedance controller for exoskeleton rehabilitation robot in this thesis, and different angle trajectory tracking and torque tracking effects of the robot were obtained by adjusting damping matrix and stiffness matrix parameters of impedance controller.

6.2 Future work and prospect

Our future work will be devoted to the study of the effects of different muscles of the lower limb on gait, aiming to reach the goal that the pathological gait predictive model can be quickly obtained based on the medical advice of the affected limb. In addition, we will also work on the study of the master-slave control strategy of the lower limb exoskeleton robot, not only to optimize the tracking accuracy of the robot, but also to improve the comfort of wearing by the patient.

We developed an impedance controller with variable parameters for the lower limb exoskeleton rehabilitation robot. Although gravity compensation is taken into account, we equate the inertia matrix of the impedance model and the inertia matrix of the robot model, however, in the later stage of rehabilitation training, the acceleration of the rehabilitation robot will increase with the strength enhancement of the affected limb, and the performance of our impedance controller will decline. To achieve the ideal impedance control, it is necessary to meet the requirements of obtaining real-time feedback of the robot joint angle and joint angular velocity, real-time feedback of the robot joint torque, and torque control of the robot. Therefore, our impedance controller is only suitable for the early stage of rehabilitation when the rehabilitation movement is slow. To achieve ideal impedance control, we need to satisfy the requirements of obtaining real-time feedback of the robot's joint angle and joint angular velocity, real-time feedback of the robot's joint torque, and the robot's torque control. These are also the main contents of our next work.

Because the EEG signal is very weak and easily disturbed, we scaled up the raw EEG data set of the 13 channels acquired for the motor imagery EEG experiment. From the analysis of the data, it is obvious that the subjects showed a significant peak at the moments of prepared squatting and full standing up. However, if we want to improve the accuracy of MI, we need not only accurate EEG hardware equipment, but also an appropriate BCI experimental paradigm for effective external stimulation. The stimulus interface and stimulus presentation style for MI is mainly implemented using HMI. Studying the MI-BCI paradigm and the development of HMI will be the main part of our work in the next step.

The PD controller for the LLER robot in Chapter 5 can achieve better trajectory tracking. Among them, the proportion and differential coefficients of the PD controller are used to obtain better trajectory tracking by trial and error method. In order to obtain better parameters, we try to find the optimal value for a given range of parameters, using the PSO algorithm.

Finally, we have the following personal views on the current status and development of the exoskeleton industry. There are several major applications for exoskeletons: military, medical rehabilitation, industrial applications (assisted handling and lifting), and consumer products (assisted walking and motion assistance).

1. Military Applications. Many countries are currently developing, but there are no mature products yet, in the stage of equipment experimentation and verification. There is a great demand for this, but the current technical performance and reliability of exoskeleton products can not meet the requirements. The future of exoskeletons for military use will only be a breakthrough, and exoskeletons will become equipment similar to soldiers' helmets. Exoskeletons for military use will be a big development in the future, and there will be no possibility of stagnation or decline.

2. Medical Rehabilitation. Although the United States and Japan have commercial applications of the product, the actual market and medical applications are very limited. Mainly the risk of using the equipment is too high, hospitals and doctors do not dare to use it and do not want to use it. A patient fall or other accidents can occur to make healthcare staff suffer the risk of losing their careers or hospitals face huge compensation. Especially in foreign countries, such as the United States, for example, one medical malpractice lawsuit can make a practicing doctor bankrupt or in debt. Therefore, the safety of medical rehabilitation equipment is definitely put in the first place. At present, lower limb rehabilitation is mainly based on fixed, sitting horizontal and passive rehabilitation equipment. The equipment is simple, reliable, safe and controllable. There is no need for special personnel to accompany and protect. The operation, disinfection, cleaning and maintenance are simple. The hospital and medical staff basically dare to use it with confidence.

3. Industrial Applications. Due to the wide use of exoskeleton for industrial use, there is a huge demand in the international market. This type of exoskeleton has the trend of becoming an auxiliary tool or labor protection appliance in production or the workplace. Most of the current industrial exoskeletons are still passive or pneumatic active, which are mechanical or electromechanical products and cannot be considered robots. Passive exoskeletons take the route of lower threshold and specific use, which is difficult to industrialize or form a new industry. Active exoskeleton robots (no power supply cable, battery-driven) will be the future development direction with great potential.

4. Consumer Products. This field should be the largest market in the future, Japan HONDA, Korea SAMSUNG, China CONCHIN (Shenzhen Kenchin Technology) and Switzerland and some other companies have launched assisted walking exoskeleton. For example: people who need to walk and stand for a long time or occupation (for example, tour guide, police, outdoor activities and other market segments and uses), the elderly (aging and rehabilitation market), people with mobility problems and other markets. In addition, some sports-assisted exoskeletons and photography-assisted exoskeletons are also gradually developed, forming a confirmed market demand. We believe that the civilian consumer application of exoskeletons will be the largest potential market in the future, but the market has yet to be further validated.

Appendix

A: Predictive assessment of the high-level control state of the simulation

Our control laws for the actuators are based on the muscle-reflex controller introduced by Geyer and Herr [80]. The modifications we made are described in section 3.2. Two different sets of control laws apply for each muscle, depending on whether the leg is in stance or swing phase (i.e., the foot is on the ground or not). We further defined a start swing state within the stance phase, and a stance preparation state within the swing phase, where control laws for a subset of MTUs are modified (see Fig. 0.1 below). The high-level control state of each leg is determined by the comparison of d , F_{GRF} and stance load threshold, swing load threshold, landing threshold and late stance threshold. The threshold parameters are obtained from the new model (the parameters of the model are modified) after being optimized by the CMA-ES algorithm. Table 0.1 shows the result of thresholds for Con-Sev.

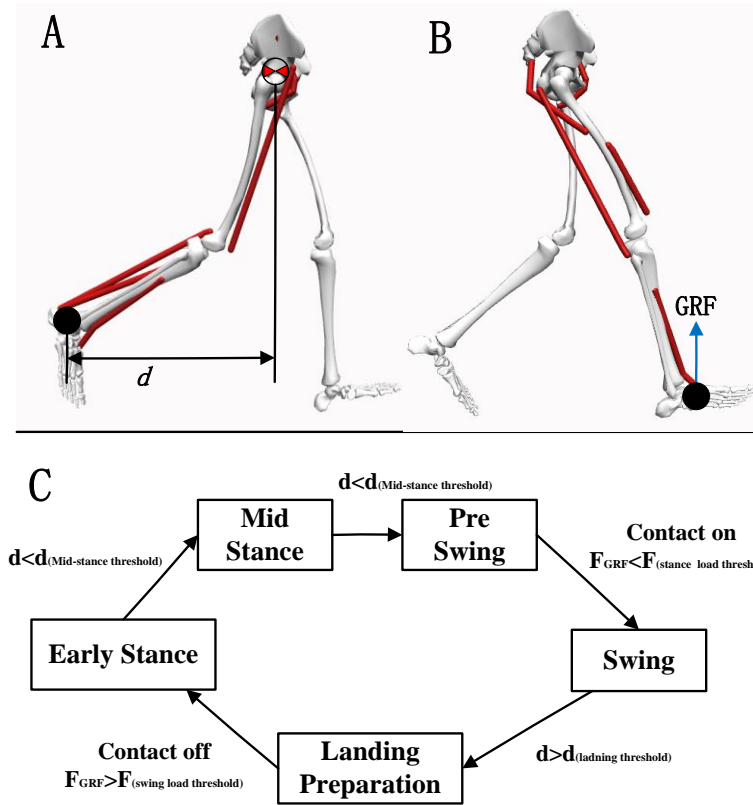


Figure 0.1 High-level control states for each leg [145]. (A) denotes the signed horizontal distance (d) between the center of gravity and the ankle of the model. (B) denotes the stance and swing phases triggered by the ground reaction force (F_{GRF}). (C) is the state transition for high-level control of each leg. $F_{(stance\ load\ threshold)}$, $F_{(swing\ load\ threshold)}$, $d_{(landing\ threshold)}$ and $d_{(late\ stance\ threshold)}$ are the threshold parameters, respectively. Corresponds to the 4 range thresholds and load thresholds mentioned in section 3.1.

Table 0. 1 Con-Sev optimized gait conversion parameters

Parameter name	Population best (CMA-ES)	Population mean (CMA-ES)	Population standard deviation (CMA-ES)
Stance load threshold	0.16124508	0.160903	0.01
Swing load threshold	0.23435794	0.23449639	0.01
Landing threshold	0.06623917	0.06597286	0.01
Late stance threshold	-0.01225637	-0.01302969	0.01

The predicted forward simulation mentioned in chapter 3 is realized as follows: the control law of the model simulation gait consists of 70 free parameters (low-level control law), 16 model kinematic parameters and 4 range parameters and load parameters (high-level control state), for a total of 90 free parameters. Section 3.1.5 is specifically: the modified model, after the optimization search with the CMA-ES algorithm in SCONE, obtains these 90 optimal parameters according to the objective function (see Equation 3.14). Therefore, the simulation results present a complete gait cycle, which, of course, can be set in SCONE with continuous gait.

The predictive dynamics simulation is achieved by optimizing the parameters. However, in the simulation experiments, we found that the sensitivity to gait was generally low by modifying the muscle parameters of the model, which may be due to the fact that the MTU of the model is not rich enough to fully simulate the actual lower limb motion. Therefore, our proposed predictive assessment module can only restore the approximate pathological gait, and of course, the lower limb exoskeleton rehabilitation robot needs to reasonably adopt the data generated by the predictive assessment module after the intervention of a physical therapist. Improving the efficiency of the predictive assessment data is one of our priorities.

Our predictive assessment module is mainly implemented using 2 software: Opensim, which builds the muscle-tendon-skeleton model, and SCONE, which uses a Covariance Matrix Adaptation Evolutionary Strategy (CMA-ES) optimization method to achieve optimized results for different models. Prof. Hartmut Geyer is one of the developers of SCONE, and this thesis involves the research of SCONE, which is based on the previous research of scone developers. In addition, we are very grateful to Thomas Geijtenbeek, one of the SCONE developers, for his help with our work.

B: Measurements for predictive assessment simulation

For the kinematic model in the prediction assessment module, we used the model from Ong, Carmichael F. et al[3] after measurements on normal subjects using Opensim. It serves as the kinematic target path threshold range for the model after being modified with MTU parameters. This threshold information corresponds to the 16 model kinematic parameters described previously. The initial model is the collection of the kinematic and force feedback data of the subject and the modeling is achieved by the following steps: 1. Experimental kinematics is used to scale the musculoskeletal model to match the dimensions of the object; 2. Solving the inverse kinematics (IK) problem to find the model joint angles that best reproduce the experimental

kinematics. 3. A residual reduction algorithm (RRA) is used to refine the model kinematics to be more dynamically consistent with the experimental reaction forces and moments. 4. A computational muscle control (CMC) algorithm is used to find a set of muscle excitations that will generate forward dynamic simulations that closely track the object's motion. From this, slow-twitch ratios were determined for 12 muscle models of the lower limbs, as shown in Table 3.1.

C: Initial Covariance Matrix Adaptation Evolutionary Strategy (CMA-ES) standard deviation for each free parameter.

Table 0.2.

Table 0. 2 Initial CMA-ES standard deviation for each free parameter.

Parameter	Description *	Initial CMA-ES standard deviation
K_C	Constant excitation ($u_C = K_C$)	0.01
$K_{F\pm}$	Force feedback gain (Eq 3.10)	0.1
K_{L+}	Length feedback gain (Eq 3.11)	0.1
l_0	Length feedback offset (Eq 3.11)	0.05
K_{V+}	Velocity feedback gain (Eq 3.12)	0.05
K_p	Pelvis tilt orientation feedback gain (Eq 3.13)	0.05
θ_0	Pelvis tilt orientation offset (Eq 3.13)	0.01
K_v	Pelvis tilt velocity feedback gain (Eq 3.13)	0.05
ES to MS	Horizontal distance between foot and pelvis	0.01
PS to S	GRF on foot	0.01
S to LP	Horizontal distance between foot and pelvis	0.01
LP to ES	GRF on foot	0.01
Initial positions	Initial pelvis tilt, hip, knee, and ankle angles	0.01
Initial velocities	Initial pelvis tilt, hip, knee, and ankle angular velocities.	0.01
Initial pelvis horizontal velocity (specified speed)	Initial pelvis horizontal velocity during a simulation with a specified speed.	0.01
Initial pelvis horizontal velocity (self-selected speed)	Initial pelvis horizontal velocity during a self-selected speed simulation.	0.1

* Equation numbers in this column refer to those in chapter 3.1.4.

References

- [1] “United Nations Population Fund (UNFPA). UNFPA report: setting the scene. Chapter 1. Available at: <http://www.unfpa.org/webdav/site/global/shared/documents/publications/2012/UNFPA-Report-Chapter1.pdf>. [accessed 04.10.15].”
- [2] J. H. B. Nijendijk, M. W. M. Post, and F. W. A. Van Asbeck, “Epidemiology of traumatic spinal cord injuries in the Netherlands in 2010,” *Spinal Cord*, vol. 52, no. 4, pp. 258–263, 2014.
- [3] C. F. Ong, T. Geijtenbeek, J. L. Hicks, and S. L. Delp, “Predicting gait adaptations due to ankle plantarflexor muscle weakness and contracture using physics-based musculoskeletal simulations,” *PLoS Comput. Biol.*, vol. 15, no. 10, pp. 1–27, 2019.
- [4] S. J. Olney and C. L. Richards, “Hemiparetic gait following stroke . Part I : Characteristics,” *Gait Posture*, vol. 4, no. 2, pp. 136–148, 1996.
- [5] S. Song and H. Geyer, “Predictive neuromechanical simulations indicate why walking performance declines with aging,” *J. Physiol.*, vol. 596, no. 7, pp. 1199–1210, 2018.
- [6] S. Armand, G. Decoulon, and A. Bonnefoy-Mazure, “Gait analysis in children with cerebral palsy,” *EFORT Open Rev.*, vol. 1, no. 12, pp. 448–460, 2016.
- [7] T. M. Campbell and G. Trudel, “Knee Flexion Contracture Associated With a Contracture and Worse Function of the Contralateral Knee: Data From the Osteoarthritis Initiative,” *Arch. Phys. Med. Rehabil.*, vol. 101, no. 4, pp. 624–632, 2020.
- [8] G. E. Rose, K. A. Lightbody, R. G. Ferguson, J. C. Walsh, and J. E. Robb, “Natural history of flexed knee gait in diplegic cerebral palsy evaluated by gait analysis in children who have not had surgery,” *Gait Posture*, vol. 31, no. 3, pp. 351–354, 2010.
- [9] J. E. Earl, S. J. Piazza, and J. Hertel, “The Protonics Knee Brace Unloads the Quadriceps Muscles in Healthy Subjects,” *J. Athl. Train.*, vol. 39, no. 1, pp. 44–49, 2004.
- [10] B. Chen, B. Zi, Z. Wang, L. Qin, and W. H. Liao, “Knee exoskeletons for gait rehabilitation and human performance augmentation: A state-of-the-art,” *Mech. Mach. Theory*, vol. 134, pp. 499–511, 2019.
- [11] Y. Wang and Z. Liu, “An impedance control method of lower limb exoskeleton rehabilitation robot based on predicted forward dynamics,” *2020 IEEE 19th Int. Conf. Trust. Secur. Priv. Comput. Commun.*, pp. 1515–1518, doi: 10.1109/TrustCom50675.2020.00206., 2020.
- [12] A. Seth, M. Sherman, J. A. Reinbolt, and S. L. Delp, “OpenSim: A musculoskeletal modeling and simulation framework for in silico investigations and exchange,” *Procedia IUTAM*, vol. 2, pp. 212–232, 2011.
- [13] J. R. Dettori, B. D. Pearson, C. J. Basmania, and W. M. Lednar, “Early ankle mobilization, part I: The immediate effect on acute, lateral ankle sprains (a randomized clinical trial),” *Mil. Med.*, vol. 159, no. 1, pp. 15–20, 1994.
- [14] Q. Wu, X. Wang, B. Chen, and H. Wu, “Development of an RBFN-based neural-fuzzy adaptive control strategy for an upper limb rehabilitation exoskeleton,” *Mechatronics*, vol. 53,

- no. January, pp. 85–94, 2018.
- [15] Q. C. Wu, X. S. Wang, and F. P. Du, “Analytical Inverse Kinematic Resolution of a Redundant Exoskeleton for Upper-Limb Rehabilitation,” *Int. J. Humanoid Robot.*, vol. 13, no. 3, pp. 1–23, 2016.
- [16] B. Chen *et al.*, “Recent developments and challenges of lower extremity exoskeletons,” *J. Orthop. Transl.*, vol. 5, pp. 26–37, 2016.
- [17] A. Rastegarpanah and M. Saadat, “Lower Limb Rehabilitation Using Patient Data,” *Appl. Bionics Biomech.*, vol. 2016, 2016.
- [18] G. Yu, J. Wang, W. Chen, and J. Zhang, “EEG-based brain-controlled lower extremity exoskeleton rehabilitation robot,” *2017 IEEE Int. Conf. Cybern. Intell. Syst. CIS 2017 IEEE Conf. Robot. Autom. Mechatronics, RAM 2017 - Proc.*, vol. 2018-Janua, pp. 763–767, 2018.
- [19] P. Milia *et al.*, “Neurorehabilitation in paraplegic patients with an active powered exoskeleton (Ekso),” *Digit. Med.*, vol. 2, no. 4, p. 163, 2016.
- [20] J. Nitschke, D. Kuhn, K. Fischer, and K. Röhl, “Reha-Technology Comparison of the Usability of the ReWalk, Ekso and HAL Exoskeletons in a Clinical Setting,” *Orthopadie Tech.*, pp. 22–26, 2014.
- [21] C. Jung, S. Jung, M. H. Chun, J. M. Lee, S. Park, and S. J. Kim, “Development of gait rehabilitation system capable of assisting pelvic movement of normal walking,” *Acta Med. Okayama*, vol. 72, no. 4, pp. 407–417, 2018.
- [22] D. Lim *et al.*, “Development of a lower extremity Exoskeleton Robot with a quasi-anthropomorphic design approach for load carriage,” *IEEE Int. Conf. Intell. Robot. Syst.*, vol. 2015-Decem, pp. 5345–5350, 2015.
- [23] H. Tannous *et al.*, “A new multi-sensor fusion scheme to improve the accuracy of knee flexion kinematics for functional rehabilitation movements,” *Sensors (Switzerland)*, vol. 16, no. 11, pp. 1–17, 2016.
- [24] B. Song, D. Lee, S. Y. Park, and Y. S. Baek, “A novel method for designing motion profiles based on a fuzzy logic algorithm using the hip joint angles of a lower-limb exoskeleton robot,” *Appl. Sci.*, vol. 10, no. 19, 2020.
- [25] X. Wang, H. Wang, and Y. Tian, “Gait planning and hybrid model based tracking control of lower extremity exoskeleton,” *Chinese Control Conf. CCC*, vol. 2016-Augus, pp. 6019–6024, 2016.
- [26] L. F. Li, F. F. Cao, X. Zhang, R. H. Liang, and G. H. Xu, “Research and development of an EEG-driven lower limb rehabilitation training system for active and passive co-stimulation,” *J. Xi’an Jiaotong Univ. (Medical Sci.)*, vol. 40, no. 1, pp. 4582–4585, 2019.
- [27] H. Faqih, M. Saad, K. Benjelloun, M. Benbrahim, and M. N. Kabbaj, *Optimization algorithm for an exoskeleton robotic inverse kinematic application*, vol. 495. Springer International Publishing, 2020.
- [28] J. M. Wang, S. R. Hamner, S. L. Delp, and V. Koltun, “Optimizing locomotion controllers

- using biologically-based actuators and objectives,” *ACM Trans. Graph.*, vol. 31, no. 4, 2012.
- [29] B. Chen *et al.*, “A wearable exoskeleton suit for motion assistance to paralysed patients,” *J. Orthop. Transl.*, vol. 11, pp. 7–18, 2017.
- [30] Y. Zheng, P. Zhong, K. Liu, K. Yang, and Q. Yue, “Human Motion Capture System Based 3D Reconstruction on Rehabilitation Assistance Stability of Lower Limb Exoskeleton Robot Climbing Upstairs Posture,” *IEEE Sens. J.*, vol. 20, no. 20, pp. 11778–11786, 2020.
- [31] L. Shi, L. Fu, and Z. Liu, “Model-based active impedance controller development of the exoskeleton rehabilitation robot (ERRobot) for lower-extremity,” *Proc. - 2018 IEEE Smart World, Ubiquitous Intell. Comput.*, pp. 150–155, 2018.
- [32] X. L. Xie *et al.*, “Model based control of a rehabilitation robot for lower extremities,” *2010 Annu. Int. Conf. IEEE Eng. Med. Biol. Soc. EMBC’10*, pp. 2263–2266, 2010.
- [33] M. Gilbert, X. Zhang, and G. Yin, “Modeling and design on control system of lower limb rehabilitation exoskeleton robot,” *2016 13th Int. Conf. Ubiquitous Robot. Ambient Intell. URAI 2016*, pp. 348–352, 2016.
- [34] C. Amici, F. Ragni, M. Ghidoni, D. Fausti, L. Bissolotti, and M. Tiboni, “Multi-sensor validation approach of an end-effector-based robot for the rehabilitation of the upper and lower limb,” *Electron.*, vol. 9, no. 11, pp. 1–16, 2020.
- [35] S. L. Delp *et al.*, “OpenSim: Open-source software to create and analyze dynamic simulations of movement,” *IEEE Trans. Biomed. Eng.*, vol. 54, no. 11, pp. 1940–1950, 2007.
- [36] K. Veerkamp, T. Geijtenbeek, J. Harlaar, and M. M. van der Krogt, “The use of predictive simulation to evaluate the effect of gastrocnemius hyperflexion on gait kinematics,” *XVII Int. Symp. Comput. Simul. Biomech. July 28th – 30th 2019, Alberta, Canada*, pp. 2–3, 2019.
- [37] S. Nakagawa, H. Mutsuzaki, Y. Mataka, R. Takeuchi, and H. Kamada, “A new tendon-lengthening technique using a tendon stripper for knee flexion contracture in a cerebral palsy patient,” *J. Orthop.*, vol. 18, pp. 110–112, 2020.
- [38] G. C. Terry and R. F. LaPrade, “The biceps femoris muscle complex at the knee: Its anatomy and injury patterns associated with acute anterolateral-antromedial rotatory instability,” *Am. J. Sports Med.*, vol. 24, no. 1, pp. 2–8, 1996.
- [39] M. M. Van Der Krogt, L. Bar-On, T. Kindt, K. Desloovere, and J. Harlaar, “Neuro-musculoskeletal simulation of instrumented contracture and spasticity assessment in children with cerebral palsy,” *J. Neuroeng. Rehabil.*, vol. 13, no. 1, pp. 1–11, 2016.
- [40] R. W. Jackson, C. L. Dembia, S. L. Delp, and S. H. Collins, “Muscle-tendon mechanics explain unexpected effects of exoskeleton assistance on metabolic rate during walking,” *J. Exp. Biol.*, vol. 220, no. 11, pp. 2082–2095, 2017.
- [41] R. G. Timmins and M. N. Bourne, “Short biceps femoris fascicles and eccentric knee flexor weakness increase the risk of hamstring injury in elite football (soccer): A prospective cohort study,” *Br. J. Sports Med.*, vol. 50, no. 24, pp. 1524–1535, 2016.
- [42] D. T. Felson, A. Naimark, J. Anderson, L. Kazis, W. Castelli, and R. F. Meenan, “The

- prevalence of knee osteoarthritis in the elderly. the framingham osteoarthritis study,” *Arthritis Rheum.*, vol. 30, no. 8, pp. 914–918, 1987.
- [43] S. R. Hamner and S. L. Delp, “Muscle contributions to fore-aft and vertical body mass center accelerations over a range of running speeds,” *J. Biomech.*, vol. 46, no. 4, pp. 780–787, 2013.
- [44] E. M. Arnold, S. R. Ward, R. L. Lieber, and S. L. Delp, “A model of the lower limb for analysis of human movement,” *Ann. Biomed. Eng.*, vol. 38, no. 2, pp. 269–279, 2010.
- [45] T. A. L. Wren, G. E. Gorton, S. Öunpuu, and C. A. Tucker, “Efficacy of clinical gait analysis: A systematic review,” *Gait Posture*, vol. 34, no. 2, pp. 149–153, 2011.
- [46] T. A. L. Wren, C. A. Tucker, S. A. Rethlefsen, G. E. Gorton, and S. Öunpuu, “Clinical efficacy of instrumented gait analysis: Systematic review 2020 update,” *Gait Posture*, vol. 80, pp. 274–279, 2020.
- [47] C. T. Pan *et al.*, “Development a multi-loop modulation method on the servo drives for lower limb rehabilitation exoskeleton,” *Mechatronics*, vol. 68, no. February, 2020.
- [48] C. Frigo and P. Crenna, “Multichannel SEMG in clinical gait analysis: A review and state-of-the-art,” *Clin. Biomech.*, vol. 24, no. 3, pp. 236–245, 2009.
- [49] P. K. Winchester, J. J. Carollo, and J. M. Wrobbel, “Reliability of gait temporal distance measures in normal subjects with and without EMG electrodes,” *Gait Posture*, vol. 4, no. 1, pp. 21–25, 1996.
- [50] S. Silvoni *et al.*, “Brain-computer interface in stroke: A review of progress,” *Clin. EEG Neurosci.*, vol. 42, no. 4, pp. 245–252, 2011.
- [51] K. K. Ang *et al.*, “A Randomized Controlled Trial of EEG-Based Motor Imagery Brain-Computer Interface Robotic Rehabilitation for Stroke,” *Clin. EEG Neurosci.*, vol. 46, no. 4, pp. 310–320, 2015.
- [52] F. Pichiorri, G. Morone, M. Petti, J. Toppi, and I. Pisotta, “Brain-computer interface boosts motor imagery practice during stroke recovery Running Head: BCI and motor imagery after stroke,” *Neuroelectrical Imaging BCI Lab.*, no. 246, p. 41, 2015.
- [53] J. Gross, P. A. Tass, S. Salenius, R. Hari, H. J. Freund, and A. Schnitzler, “Cortico-muscular synchronization during isometric muscle contraction in humans as revealed by magnetoencephalography,” *J. Physiol.*, vol. 527, no. 3, pp. 623–631, 2000.
- [54] M. Varlet, S. Nozaradan, L. Trainor, and P. E. Keller, “Dynamic Modulation of Beta Band Cortico-Muscular Coupling Induced by Audio-Visual Rhythms,” *Cereb. Cortex Commun.*, vol. 1, no. 1, pp. 1–13, 2020.
- [55] S. Nakagome, T. P. Luu, Y. He, A. S. Ravindran, and J. L. Contreras-Vidal, “An empirical comparison of neural networks and machine learning algorithms for EEG gait decoding,” *Sci. Rep.*, vol. 10, no. 1, pp. 1–17, 2020.
- [56] H. Yokoyama, N. Kaneko, T. Ogawa, N. Kawashima, K. Watanabe, and K. Nakazawa, “Cortical Correlates of Locomotor Muscle Synergy Activation in Humans: An Electroencephalographic Decoding Study,” *iScience*, vol. 15, pp. 623–639, 2019.

- [57] S. M. Shafiul Hasan, M. R. Siddiquee, R. Atri, R. Ramon, J. S. Marquez, and O. Bai, "Prediction of gait intention from pre-movement EEG signals: A feasibility study," *J. Neuroeng. Rehabil.*, vol. 17, no. 1, pp. 1–16, 2020.
- [58] S. M. S. Hasan, M. R. Siddiquee, and O. Bai, "Supervised Classification of EEG Signals with Score Threshold Regulation for Pseudo-online Asynchronous Detection of Gait Intention," pp. 2019–2022, 2019.
- [59] I. Luppi, "Commentary on the presentation of Dr. Elza Berquó. Methodological and theoretical reflections on the survey questionnaire: An integrated approach," *Rev. Bras. Epidemiol.*, vol. 11, no. SUPPL. 1, pp. 90–97, 2008.
- [60] E. Poortinga, "Event-related EEG/MEG synchronization and desynchronization: basic principles," *Studiemeesters*, vol. 110, pp. 1842–1857, 2012.
- [61] A. M. Dollar and H. Herr, "Lower extremity exoskeletons and active orthoses: Challenges and state-of-the-art," *IEEE Trans. Robot.*, vol. 24, no. 1, pp. 144–158, 2008.
- [62] H. Yan, H. Wang, L. Vladareanu, M. Lin, V. Vladareanu, and Y. Li, "Detection of participation and training task difficulty applied to the multi-sensor systems of rehabilitation robots," *Sensors (Switzerland)*, vol. 19, no. 21, 2019.
- [63] M. Vasanthakumar, B. Vinod, J. K. Mohanta, and S. Mohan, "Design and Robust Motion Control of a Planar 1P-2P RP Hybrid Manipulator for Lower Limb Rehabilitation Applications," *J. Intell. Robot. Syst. Theory Appl.*, vol. 96, no. 1, pp. 17–30, 2019.
- [64] S. Jezernik, G. Colombo, T. Keller, H. Frueh, and M. Morari, "Robotic Orthosis Lokomat: A Rehabilitation and Research Tool," *Neuromodulation*, vol. 6, no. 2, pp. 108–115, 2003.
- [65] J. Pransky, "The Pransky interview: Russ Angold, Co-Founder and President of Ekso™ Labs," *Ind. Rob.*, vol. 41, no. 4, pp. 329–334, 2014.
- [66] A. Tsukahara, R. Kawanishi, Y. Hasegawa, and Y. Sankai, "Sit-to-stand and stand-to-sit transfer support for complete paraplegic patients with robot suit HAL," *Adv. Robot.*, vol. 24, no. 11, pp. 1615–1638, 2010.
- [67] A. B. Zoss, H. Kazerooni, and A. Chu, "Biomechanical design of the Berkeley Lower Extremity Exoskeleton (BLEEX)," *IEEE/ASME Trans. Mechatronics*, vol. 11, no. 2, pp. 128–138, 2006.
- [68] J. B. Webster *et al.*, "Design of the Berkeley lower extremity exoskeleton (BLEEX)," *Int. J. Cybern. Informatics*, vol. 38, no. 2, pp. 531–1424413206, 2016.
- [69] R. L. Attwells, S. A. Birrell, R. H. Hooper, and N. J. Mansfield, "Influence of carrying heavy loads on soldiers' posture, movements and gait," *Ergonomics*, vol. 49, no. 14, pp. 1527–1537, 2006.
- [70] M. A. Boswell *et al.*, "A neural network to predict the knee adduction moment in patients with osteoarthritis using anatomical landmarks obtainable from 2D video analysis," *Osteoarthr. Cartil.*, no. xxxx, 2021.
- [71] U. Muico, Y. Lee, J. Popovi, and Z. Popovi, "Contact-aware nonlinear control of dynamic

- characters,” *ACM Trans. Graph.*, vol. 28, no. 3, 2009.
- [72] T. Kwon and J. Hodgins, “Control systems for human running using an inverted pendulum model and a reference motion capture sequence,” *Comput. Animat. 2010 - ACM SIGGRAPH / Eurographics Symp. Proceedings, SCA 2010*, pp. 129–138, 2010.
- [73] M. Da Silva, Y. Abe, and J. Popović, “Interactive simulation of stylized human locomotion,” *ACM Trans. Graph.*, vol. 27, no. 3, 2008.
- [74] Pandy M G, Andriacchi T P. Muscle and joint function in human locomotion[J]. Annual review of biomedical engineering, 2010, 12: 401-433.
- [75] Chen B, Ma H, Qin L Y, et al. Recent developments and challenges of lower extremity exoskeletons[J]. Journal of Orthopaedic Translation, 2016, 5: 26-37.
- [76] M. Ackermann and A. J. van den Bogert, “Optimality principles for model-based prediction of human gait,” *J. Biomech.*, vol. 43, no. 6, pp. 1055–1060, 2010.
- [77] F. C. Anderson and M. G. Pandy, “Dynamic optimization of human walking,” *J. Biomech. Eng.*, vol. 123, no. 5, pp. 381–390, 2001.
- [78] K. M. Steele, A. Seth, J. L. Hicks, M. S. Schwartz, and S. L. Delp, “Muscle contributions to support and progression during single-limb stance in crouch gait,” *J. Biomech.*, vol. 43, no. 11, pp. 2099–2105, 2010.
- [79] K. M. Steele, M. M. van der Krogt, M. H. Schwartz, and S. L. Delp, “How much muscle strength is required to walk in a crouch gait?,” *J. Biomech.*, vol. 45, no. 15, pp. 2564–2569, Oct. 2012.
- [80] H. Geyer and H. Herr, “A Muscle-reflex model that encodes principles of legged mechanics produces human walking dynamics and muscle activities,” *IEEE Trans. Neural Syst. Rehabil. Eng.*, vol. 18, no. 3, pp. 263–273, 2010.
- [81] S. Song and H. Geyer, “A neural circuitry that emphasizes spinal feedback generates diverse behaviours of human locomotion,” *J. Physiol.*, vol. 593, no. 16, pp. 3493–3511, 2015.
- [82] T. Geijtenbeek, “SCONE: Open Source Software for Predictive Simulation of Biological Motion,” *J. Open Source Softw.*, vol. 4, no. 38, p. 1421, 2019.
- [83] S. K. Ajay Seth*, Jennifer L. Hicks, Thomas K. Uchida, Ayman Habib, Christopher L. Dembia, James J. Dunne, Carmichael F. Ong, Matthew S. DeMers, Apoorva Rajagopal, Matthew Millard, Samuel R. Hamner, Edith M. Arnold, Jennifer R. Yong and 1, “OpenSim: Simulating musculoskeletal dynamics and neuromuscular control to study human and animal movement,” *Physiol. Psychol.*, vol. 1, no. 2, pp. 152–154, 2018.
- [84] Z. F. Lerner, M. S. DeMers, S. L. Delp, and R. C. Browning, “How tibiofemoral alignment and contact locations affect predictions of medial and lateral tibiofemoral contact forces,” *J. Biomech.*, vol. 48, no. 4, pp. 644–650, 2015.
- [85] C. F. Ong, T. Geijtenbeek, J. L. Hicks, and S. L. Delp, “Predicting gait adaptations due to ankle plantarflexor muscle weakness and contracture using physics-based musculoskeletal simulations,” *bioRxiv*, vol. 15, no. 10, pp. 1–40, 2019.

- [86] T. K. Uchida, A. Seth, S. Pouya, C. L. Dembia, J. L. Hicks, and S. L. Delp, "Simulating ideal assistive devices to reduce the metabolic cost of running," *PLoS One*, vol. 11, no. 9, pp. 1–19, 2016.
- [87] S. R. Ward, C. M. Eng, L. H. Smallwood, and R. L. Lieber, "Are current measurements of lower extremity muscle architecture accurate?," *Clin. Orthop. Relat. Res.*, vol. 467, no. 4, pp. 1074–1082, 2009.
- [88] S. S. Blemker and S. L. Delp, "Rectus femoris and vastus intermedius fiber excursions predicted by three-dimensional muscle models," *J. Biomech.*, vol. 39, no. 8, pp. 1383–1391, 2006.
- [89] X. Chen, G. N. Sanchez, M. J. Schnitzer, and S. L. Delp, "Changes in sarcomere lengths of the human vastus lateralis muscle with knee flexion measured using in vivo microendoscopy," *J. Biomech.*, vol. 49, no. 13, pp. 2989–2994, 2016.
- [90] F. Romero and F. J. Alonso, "A comparison among different Hill-type contraction dynamics formulations for muscle force estimation," *Mech. Sci.*, vol. 7, no. 1, pp. 19–29, 2016.
- [91] H. Geyer, A. Seyfarth, and R. Blickhan, "Positive force feedback in bouncing gaits?," *Proc. R. Soc. B Biol. Sci.*, vol. 270, no. 1529, pp. 2173–2183, 2003.
- [92] C. F. Ong, T. Geijtenbeek, J. L. Hicks, and S. L. Delp, "Predicting gait adaptations due to ankle plantarflexor muscle weakness and contracture using physics-based musculoskeletal simulations," *PLoS Comput. Biol.*, vol. 15, no. 10, pp. 1–40, 2019.
- [93] M. S. DeMers, J. L. Hicks, and S. L. Delp, "Preparatory co-activation of the ankle muscles may prevent ankle inversion injuries," *J. Biomech.*, vol. 52, pp. 17–23, 2017.
- [94] A. Rajagopal, C. L. Dembia, M. S. DeMers, D. D. Delp, J. L. Hicks, and S. L. Delp, "Full-Body Musculoskeletal Model for Muscle-Driven Simulation of Human Gait," *IEEE Trans. Biomed. Eng.*, vol. 63, no. 10, pp. 2068–2079, Oct. 2016.
- [95] G. G. Handsfield, C. H. Meyer, J. M. Hart, M. F. Abel, and S. S. Blemker, "Relationships of 35 lower limb muscles to height and body mass quantified using MRI," *J. Biomech.*, vol. 47, no. 3, pp. 631–638, 2014.
- [96] E. M. Arnold, S. R. Hamner, A. Seth, M. Millard, and S. L. Delp, "How muscle fiber lengths and velocities affect muscle force generation as humans walk and run at different speeds," *J. Exp. Biol.*, vol. 216, no. 11, pp. 2150–2160, 2013.
- [97] S. L. Delp, J. P. Loan, M. G. Hoy, F. E. Zajac, E. L. Topp, and J. M. Rosen, "An Interactive Graphics-Based Model of the Lower Extremity to Study Orthopaedic Surgical Procedures," *IEEE Trans. Biomed. Eng.*, vol. 37, no. 8, pp. 757–767, 1990.
- [98] A. J. van Soest and M. F. Bobbert, "The contribution of muscle properties in the control of explosive movements," *Biol. Cybern.*, vol. 69, no. 3, pp. 195–204, 1993.
- [99] S. Jabeen, A. Berry, T. Geijtenbeek, J. Harlaar, and H. Vallery, "Assisting gait with free moments or joint moments on the swing leg," *IEEE Int. Conf. Rehabil. Robot.*, vol. 2019-June, pp. 1079–1084, 2019.

- [100] Q. Liu, J. Zuo, C. Zhu, and S. Q. Xie, “Design and control of soft rehabilitation robots actuated by pneumatic muscles: State of the art,” *Futur. Gener. Comput. Syst.*, vol. 113, pp. 620–634, 2020.
- [101] M. H. Schwartz, A. Rozumalski, and J. P. Trost, “The effect of walking speed on the gait of typically developing children,” *J. Biomech.*, vol. 41, no. 8, pp. 1639–1650, 2008.
- [102] F. Moissenet and S. Armand, “Qualitative and quantitative methods of assessing gait disorders,” *Orthop. Manag. Child. with Cereb. Palsy A Compr. Approach*, pp. 215–240, 2015.
- [103] T. W. Dorn, J. M. Wang, J. L. Hicks, and S. L. Delp, “Predictive simulation generates human adaptations during loaded and inclined walking,” *PLoS One*, vol. 10, no. 4, pp. 1–16, 2015.
- [104] M. Q. Liu, F. C. Anderson, M. H. Schwartz, and S. L. Delp, “Muscle contributions to support and progression over a range of walking speeds,” *J. Biomech.*, vol. 41, no. 15, pp. 3243–3252, 2008.
- [105] U. J and K. Y, *Human modeling for bio-inspired robotics: mechanical engineering in assistive technologies*. 2016.
- [106] J. R. Wolpaw, D. J. McFarland, and T. M. Vaughan, “Brain-computer interface research at the Wadsworth Center,” *IEEE Trans. Rehabil. Eng.*, vol. 8, no. 2, pp. 222–226, 2000.
- [107] B. Blankertz *et al.*, “The Berlin brain-computer interface: Progress beyond communication and control,” *Front. Neurosci.*, vol. 10, no. NOV, 2016.
- [108] N. Birbaumer and L. G. Cohen, “Brain-computer interfaces: Communication and restoration of movement in paralysis,” *J. Physiol.*, vol. 579, no. 3, pp. 621–636, 2007.
- [109] K. Wiley, “Control and Trajectory Generation of a Wearable Mobility Exoskeleton for Spinal Cord Injury Patients,” *UC Berkeley Electron. Theses Diss.*, p. 67, 2011.
- [110] M. A. Lebedev and M. A. L. Nicolelis, “Brain-machine interfaces: past, present and future,” *Trends Neurosci.*, vol. 29, no. 9, pp. 536–546, 2006.
- [111] M. Tangermann *et al.*, “Optimized stimulation events for a visual ERP BCI,” *Int. J. Bioelectromagn.*, vol. 13, no. 3, pp. 119–120, 2011.
- [112] I. Volosyak, D. Valbuena, T. Lüth, T. Malechka, and A. Gräser, “BCI demographics II: How many (and What Kinds of) people can use a high-frequency SSVEP BCI?,” *IEEE Trans. Neural Syst. Rehabil. Eng.*, vol. 19, no. 3, pp. 232–239, 2011.
- [113] H. Jasper and W. Penfield, “Electrocorticograms in man: Effect of voluntary movement upon the electrical activity of the precentral gyrus,” *Arch. Psychiatr. Nervenkr.*, vol. 183, no. 1–2, pp. 163–174, 1949.
- [114] J. Kalcher, D. Flotzinger, C. Neuper, S. Gölly, and G. Pfurtscheller, “Graz brain-computer interface II: Towards communication between humans and computers based on online classification of three different EEG patterns,” *Med. Biol. Eng. Comput.*, vol. 34, no. 5, pp. 382–388, 1996.
- [115] M. Barsotti, D. Leonardis, C. Loconsole, M. Solazzi, and E. Sotgiu, “IEEE International Conference on Rehabilitation Robotics,” *IEEE Int. Conf. Rehabil. Robot.*, vol. 2015-Sept, no.

- Mi, pp. 49–54, 2015.
- [116] M. H. Lee *et al.*, “EEG dataset and OpenBMI toolbox for three BCI paradigms: An investigation into BCI illiteracy,” *Gigascience*, vol. 8, no. 5, pp. 1–16, 2019.
- [117] B. R. Cahn and J. Polich, “Meditation states and traits: EEG, ERP, and neuroimaging studies,” *Psychol. Bull.*, vol. 132, no. 2, pp. 180–211, 2006.
- [118] J. Gamble, “Electroencephalography: Basic Principles, Clinical Applications, and Related Fields, Fifth Edition,” *Aust. Occup. Ther. J.*, vol. 39, no. 2, pp. 44–45, 1992.
- [119] X. Jia and A. Kohn, “Gamma rhythms in the brain,” *PLoS Biol.*, vol. 9, no. 4, pp. 1–5, 2011.
- [120] J. L. Contreras-Vidal *et al.*, *Neural Decoding of Robot-Assisted Gait during Rehabilitation after Stroke*, vol. 97, no. 8. 2018.
- [121] Luo R, Sun S, Zhang X, et al. A low-cost end-to-end sEMG-based gait sub-phase recognition system[J]. *IEEE Transactions on Neural Systems and Rehabilitation Engineering*, 2019, 28(1): 267-276.
- [122] Y. Nakamura, K. Yamane, Y. Fujita, and I. Suzuki, “Somatosensory computation for man-machine interface from motion-capture data and musculoskeletal human model,” *IEEE Trans. Robot.*, vol. 21, no. 1, pp. 58–66, 2005.
- [123] L. F. Lee, M. S. Narayanan, S. Kannan, F. Mendel, and V. N. Krovi, “Case studies of musculoskeletal-simulation-based rehabilitation program evaluation,” *IEEE Trans. Robot.*, vol. 25, no. 3, pp. 634–638, 2009.
- [124] Agarwal P, Narayanan M S, Lee L F, et al. Simulation-based design of exoskeletons using musculoskeletal analysis[C]//International Design Engineering Technical Conferences and Computers and Information in Engineering Conference. 2010, 44113: 1357-1364.
- [125] A. Campeau-Lecours, M. J. D. Otis, and C. Gosselin, “Modeling of physical human-robot interaction: Admittance controllers applied to intelligent assist devices with large payload,” *Int. J. Adv. Robot. Syst.*, vol. 13, no. 5, pp. 1–12, 2016.
- [126] J. F. Veneman, R. Ekkelenkamp, R. Kruidhof, F. C. T. Van Der Helm, and H. Van Der Kooij, “A series elastic- and bowden-cable-based actuation system for use as torque actuator in exoskeleton-type robots,” *Int. J. Rob. Res.*, vol. 25, no. 3, pp. 261–281, 2006.
- [127] G. Colombo, M. Joerg, R. Schreier, and V. Dietz, “Treadmill training of paraplegic patients using a robotic orthosis,” *J. Rehabil. Res. Dev.*, vol. 37, no. 6, pp. 693–700, 2000.
- [128] C. Sheng, “Mirror-type rehabilitation training with dynamic adjustment and assistance for shoulder joint,” *J. Biomed. Eng.*, vol. 38, no. 2, pp. 1–10, 2021.
- [129] J. L. Emken, S. J. Harkema, J. A. Beres-Jones, C. K. Ferreira, and D. J. Reinkensmeyer, “Feasibility of manual teach-and-replay and continuous impedance shaping for robotic locomotor training following spinal cord injury,” *IEEE Trans. Biomed. Eng.*, vol. 55, no. 1, pp. 322–334, 2008.
- [130] N. Li, L. Yan, H. Qian, H. Wu, J. Wu, and S. Men, “Review on lower extremity exoskeleton robot,” *Open Autom. Control Syst. J.*, vol. 7, no. 1, pp. 441–453, 2015.

- [131] X. Jiao, Y. Li, Y. Fang, and S. Geng, "A robust adaptive control method for robot," *Robot Tech. Appl.*, vol. 1, no. 3, pp. 40–43, 2002.
- [132] J. J. Craig and M. H. Raibert, "A systematic method of hybrid position/force control of a manipulator," *Proc. - Int. Comput. Softw. Appl. Conf.*, pp. 446–451, 1979.
- [133] N. Hogan, "Impedance Control : An Approach to Manipulation : Part I - Theory," *J. Dyn. Syst. Meas. Control. Trans. ASME*, vol. 107, no. 1, pp. 17–24, 1985.
- [134] N. Hogan, "Impedance control: An approach to manipulation: Part III-applications," *J. Dyn. Syst. Meas. Control. Trans. ASME*, vol. 107, no. 1, pp. 17–24, 1985.
- [135] A. Alessandri, "Adaptive neural network control of robotic manipulators," *Automatica*, vol. 40, no. 11, pp. 2011–2012, 2004.
- [136] S. S. Ge, Y. Li, and C. Wang, "Impedance adaptation for optimal robot-environment interaction," *Int. J. Control*, vol. 87, no. 2, pp. 249–263, 2014.
- [137] J. Buchli, F. Stulp, E. Theodorou, and S. Schaal, "Learning variable impedance control," *Int. J. Rob. Res.*, vol. 30, no. 7, pp. 820–833, 2011.
- [138] B. J. Fregly *et al.*, "Grand challenge competition to predict in vivo knee loads," *J. Orthop. Res.*, vol. 30, no. 4, pp. 503–513, 2012.
- [139] Y. Wang, "Development of Numerical Modeling and Temperature Controller Optimization for Internal Heating Vacuum Furnace," *IEEE Access*, vol. 9, pp. 1–9, 2021.
- [140] J. Zhao, T. Li, and J. Qian, "Application of particle swarm optimization algorithm on robust PID controller tuning," *Lect. Notes Comput. Sci.*, vol. 3612, no. PART III, pp. 948–957, 2005.
- [141] J. S. Chiou and M. T. Liu, "Numerical simulation for Fuzzy-PID controllers and helping EP reproduction with PSO hybrid algorithm," *Simul. Model. Pract. Theory*, vol. 17, no. 10, pp. 1555–1565, 2009.
- [142] Z. H. Ren and J. Wang, "Accelerate convergence particle swarm optimization algorithm," *Kongzhi yu Juece/Control Decis.*, vol. 26, no. 2, pp. 201–206, 2011.
- [143] C. Sankar Rao, S. Santosh, and V. Dhanya Ram, "Tuning optimal PID controllers for open loop unstable first order plus time delay systems by minimizing ITAE criterion," *IFAC-PapersOnLine*, vol. 53, no. 1, pp. 123–128, 2020.
- [144] Mehta S, Singh M, Pamula R. Analysis of min-max algorithm and PSO algorithm for data clustering[C]//Proceedings of the 2020 International Conference on Big Data in Management. 2020: 23-27.
- [145] J. M. Wang, S. R. Hamner, S. L. Delp, and V. Koltun, "Optimizing Locomotion Controllers Using Biologically-Based Actuators and Objectives Supplemental Material," *ACM Transactions on Graphics*, pp. 1–8, 2012.